

**Nano-integrated Polymeric Suspended Microfluidic Platform  
for Ultra-Sensitive Bio-Molecular Recognition**

**Hamid SadAbadi**

A Thesis  
in  
The Department  
of  
Mechanical and Industrial Engineering

Presented in Partial Fulfillment of the Requirements  
for the Degree of Doctor of Philosophy of science at  
Concordia University  
Montreal, Quebec, Canada

August, 2013

© Hamid SadAbadi, 2013

**CONCORDIA UNIVERSITY**

**School of Graduate Studies**

This is to certify that the thesis prepared

By: **Hamid SadAbadi**

Entitled: **Nano-integrated Polymeric Suspended Microfluidic Platform for Ultra-Sensitive Bio-Molecular Recognition**

and submitted in partial fulfillment of the requirements for the degree of

**Doctor of Philosophy (Mechanical and Industrial Engineering)**

complies with the regulations of the University and meets the accepted standards with respect to originality and quality.

Signed by the final Examining Committee:

Dr. XXX XXXX Chair

Dr. Krishnan Venkatakrishnan External Examiner

Wei-Ping Zhu External to Program

Dr. Ramin Sedaghati Examiner

Dr. Narayanswamy Sivakumar Examiner

Dr. Muthukumaran Packirisamy Co-Supervisor

Dr. Rolf Wüthrich Co-Supervisor

Approved by:

Dr. Martin D. Pugh Chair of Department (MIE)

Dr. Robin Drew Dean of Faculty (ENCS)

# **Nano-integrated Polymeric Suspended Microfluidic Platform for Ultra-Sensitive Bio-Molecular Recognition**

Hamid SadAbadi, PhD of mechanical Engineering  
Concordia University, February 2013

## **Abstract**

The development of biosensors for the detection of biomolecules recognition is an extremely important problem in life science and clinical diagnostics. Many researchers and bio-scientists around the world are looking to present a simple and cost-effective ultra-sensitive platform for the bio-sensing applications in order to detect protein-protein interaction, DNA hybridization, and antigen-antibody interaction.

Microcantilever (MC) transducer is a well-known sensing mechanism for biosensing application. In this method, a surface-stress will be induced through the bimolecular recognition on the cantilever surface, which results in the MC deflection. The magnitude of deflection is related to the number of (or concentration of) biomolecules of interest that were immobilized on the MC's surface during the biosensing protocols. However, one of the main drawbacks of cantilever biosensors is the high amount of analytes (proteins, DNA, polypeptides, etc.) that are required for sensing experiments as the cantilever must be submerged in the analytes. In addition, the cantilever bending read-out system (that can be optical or electrical) has to be designed sensitive enough to make it possible to measure deflection in the range of a few nanometers.

In order to move toward ultra-sensitive biomolecular detection, one way is to increase the read-out resolution which makes the system more complex and expensive. Another solution is to fabricate the MC from materials different from silicon with less stiffness.

In addition, in order to reduce analytes consumption, integration of microfluidic systems with microcantilevers would be beneficial. Through this integration, both the volume of analytes and the time of response are reduced. This thesis reports a promising method towards ultra-sensitive biosensing by integration of microfluidic system into a

polymeric microcantilever. The fabricated platform is referred as "Polymeric Suspended Microfluidics". In order to immobilize biomolecule of interest for the biosensing application inside the microfluidic system, gold nanoparticles (AuNPs) are integrated into the buried microfluidics by two different methods. The thesis also presents a novel 3D micromixer in order to implement in-situ synthesis of AuNPs. The 3D micromixer has been fabricated and tested for characterizing mixing performance.

The results of biosensing shows significant improvement in the sensitivity of the proposed platform compared with the common silicon based MC biosensor. The results show the proposed integrated sensing platform achieved a detection limit of 2ng/ml (100pM) toward the growth hormones biosensing (Ag-Ab interaction detection). The results demonstrate a proof-of-principal for successful polymeric cantilever fabrication towards the next generation of cantilever-based biosensing mechanism which has high potential to enable femtomolar (fM) biomolecular recognition detection.

## **Acknowledgments**

I would like to express my sincere gratitude to my advisors Dr. Muthukumaran Packirisamy and Dr. Rolf Wuthrich for the continuous support of my Ph.D study and research, for their patience, motivation, enthusiasm, and immense guidance. First and most, I would like to thank them from the bottom of my heart for all their contributions, guidance, remarkable/practical ideas, and encouragement. I could not have imagined having better advisors and mentors for my Ph.D study. Throughout my thesis-writing period, they provided encouragement, sound advices and lots of good ideas.

Moreover, I am also extremely indebted to Dr. Simona Badilescu for providing valuable advices, constructive criticism and extensive discussions about my experimental work. Indeed, whenever I felt lost, stressed, or lacking the confidence to continue, I could always depend on her advices to provide direction, help, and support.

I would also like to thank the members of my defense committee, Dr. Krishnan Venkatakrishnan, Dr. Wei-Ping Zhu, Dr. Ramin Sedaghati, and Dr. Narayanswamy Sivakumar, for taking their valuable time to examine my thesis.

Special thanks to the administrative staff at Concordia University: Leslie Hossein, Arlene Zimmerman, Sophie Mélineau and Maureen Thuringer. I also would like to thank technical staff of the department, Dainius Juras, Brad Luckhart, and Henry Szczawinski for their assistance. Also thanks to Mazen Samara at Concordia University, Nicole

MacDonald and Philippe Plamondon at Ecole Polytechnic de Montreal, and David Liu at McGill University for their assistance with SEM imaging.

Very special thanks to all of my friends and lab-mates in the Optical-Bio MEMS laboratory and Electrocatalytic Green Engineering Group: Arvind, Ahmad, Stefan, Pierre, Morteza, Maniya, Jana, Anis, Siamak, Andrew, and all others. Particularly, I would like to thank Masoud, Roozbeh, Amir, Mahmoud, Jayan and Mohammad, all six of whom helped me with the experimental setup as well as their helpful discussions and valuable ideas. Definitely I could not have had better friends and colleagues.

My deepest heartfelt gratitude goes out to my wife, Sepideh and my mother, Kobrah, and My father, Mr. Gholamreza SadAbadi. Words simply cannot express my gratitude for their love and support. They have been with me every single step from the beginning to the end and definitely, I could not have achieved it without them. They provided the best possible network of love and support and help and kindness without which I would not have been able to carry on my studies to the doctoral level.

*To*

*The love of my life, Sepideh,  
My mother and my father*

# Table of contents

Acknowledgments.....	v
Table of contents.....	viii
<b>List of Figures</b> .....	xii
<b>List of Tables</b> .....	xvii
<b>Nomenclature</b> .....	xvii
<b>Chapter 1: Introduction and Literature review</b> .....	1
1.1 Introduction.....	1
1.1.1 Mechanical transducers as biosensors.....	1
1.1.2 Microfluidic systems for biosensing.....	4
1.1.3 Gold Nanoparticles in biosensors.....	5
1.2 Literature review.....	8
1.2.1 Micromechanical transducers.....	8
1.2.2 Microfluidic integrated cantilevers in biosensing.....	10
1.2.3 Gold nanoparticles in biosensing.....	12
1.3 Thesis motivation.....	15
1.4 Thesis Objectives and Scopes.....	17
1.4.1 Objectives.....	17
1.4.2 Sub-objectives.....	19
1.5 Thesis contributions.....	20
1.6 Organization of the Thesis in Manuscript-based format.....	21
<b>Chapter 2: PDMS Nanocomposite Platforms with Enhanced Sensing Properties</b> ... 25	
2.1 Introduction.....	25
2.2 Experimental.....	29
2.2.1 Materials.....	29
2.2.2 Fabrication of PDMS and synthesis Au-PDMS.....	29
2.2.3 Post processing synthesis processes of the gold nanocomposite.....	31
2.2.4 Tension test.....	32
2.2.5 Porosity measurement.....	32
2.2.6 Sensitivity Tests.....	34
2.2.7 Biosensing protocol.....	34
2.3 Results and Discussion.....	35
2.3.1 In-situ synthesis and characterization of the Au-PDMS nanocomposite.....	35

2.3.2	Annealing and swelling of the as-prepared Au-PDMS nanocomposites .....	39
2.3.3	Mechanical properties of PDMS and Au-PDMS nanocomposite .....	42
2.3.4	Porosity.....	43
2.3.5	Sensitivity test .....	45
2.3.6	Biosensing experiments.....	46
2.4	Conclusion.....	48
<b>Chapter 3: Microwave-Assisted Fabrication of Gold-PDMS Nanocomposite .....</b>		<b>49</b>
3.1	Introduction .....	49
3.2	Material and methods .....	53
3.2.1	Materials.....	53
3.2.2	Fabrication of PDMS.....	53
3.2.3	In-situ synthesis of Au-PDMS nanocomposite .....	54
3.2.4	Annealing process .....	55
3.2.5	Tension test .....	55
3.2.6	Sensitivity Test.....	55
3.2.7	Biosensing protocol.....	56
3.3	Results and Discussion.....	57
3.3.1	Microwave-induced reduction of gold ions.....	57
3.3.2	Mechanical properties .....	63
3.3.3	Sensitivity of the platform and biosensing.....	64
3.4	Conclusion.....	67
<b>Chapter 4: High performance PDMS micromixer .....</b>		<b>69</b>
4.1	Introduction .....	69
4.2	Design .....	72
4.2.1	Design Principle .....	72
4.2.2	Optimization of the micromixer dimensions.....	74
4.3	Simulation model .....	76
4.3.1	Simulation performance assessment.....	77
4.3.2	Simulation results .....	78
4.4	Fabrication.....	81
4.5	Experimental mixing results.....	83
4.5.1	Flow visualization .....	83
4.5.2	Mixing testing of acid and base.....	84
4.6	Conclusion.....	87

<b>Chapter 5: Gold nanoparticles integrated PDMS microfluidic chip</b> .....	88
5.1 Introduction .....	88
5.2 Material and methods .....	91
5.2.1 Materials .....	91
5.2.2 Fabrication of PDMS microfluidic chip and in-situ synthesis of Au-PDMS .....	91
5.2.3 Sensitivity Tests .....	94
5.2.4 Biosensing protocol .....	95
5.3 Results and Discussion .....	96
5.3.1 In-situ synthesis and kinetical study of the reaction .....	96
5.3.2 Particle size distribution in micro and macro environments .....	100
5.3.3 Sensing experiments .....	103
5.4 Conclusions .....	105
<b>Chapter 6: Realization of Polymeric Suspended Microfluidics</b> .....	107
6.1 Introduction .....	107
6.2 Design and Fabrication of the SPMF cantilever .....	110
6.2.1 Fabrication of SU-8 molds .....	111
6.2.2 Fabrication of suspended PDMS microfluidics (SPMF) .....	115
6.3 Snapping problem .....	119
6.4 Optimization of cantilever thickness .....	121
6.4.1 Finite Element Modeling .....	123
6.5 Conclusion .....	127
<b>Chapter 7: Integration of gold nanoparticles (AuNPs) on SPMF</b> .....	129
7.1 Introduction .....	129
7.2 Material and methods .....	132
7.2.1 Materials .....	132
7.2.2 Fabrication of microreactor .....	132
7.2.3 Synthesis of AuNPs in a microfluidic environment .....	133
7.2.4 Integration of 3D-micromixer with microreactor .....	136
7.2.5 Biosensing protocol and experiment .....	138
7.3 Results and discussions .....	141
7.3.1 Au-PDMS nanocomposite fabrication and SEM characterization .....	141
7.3.2 Static deflection of PDMS cantilever tip .....	143
7.3.3 Antigen-antibody interaction and determination of detection limit .....	144
7.4 Conclusions .....	146

<b>Chapter 8: Towards Femtomolar (fM) Sensing of Biomolecular Recognition</b> .....	148
8.1 Introduction .....	148
8.2 Material and methods .....	153
8.2.1 Materials .....	153
8.2.2 Integration of gold nanoparticles (AuNPs) into microchannel .....	153
8.2.3 Biosensing protocol and experiment .....	154
8.3 Results and Discussion .....	157
8.3.1 Au-PDMS nanocomposite fabrication and SEM characterization .....	157
8.3.2 Kinetics of the in-situ reduction reaction .....	160
8.3.3 Static deflection of SPMF cantilever .....	161
8.3.4 Biosensing experiment and estimation of detection limit .....	162
8.4 Conclusion .....	165
<b>Chapter 9: Conclusions</b> .....	167
9.1 Summary and conclusions .....	167
9.2 Future works .....	169
Reference .....	172

## List of Figures

<i>Figure 1-1: Scanning electron micrograph of a microfabricated silicon cantilever array (1 <math>\mu\text{m}</math> thick, 500 <math>\mu\text{m}</math> long, and 100 <math>\mu\text{m}</math> wide, pitch of 250 <math>\mu\text{m}</math>, spring constant 0.02 N m<sup>-1</sup>; Micro- and Nanomechanics Group, IBM Zurich Research Laboratory, Switzerland) [4].</i>	2
<i>Figure 1-2: Labeled-free detection of Ag/Ab interaction into the surface of cantilever. The interaction generates a compressive surface stress, which causes the cantilever to bend [6].</i>	3
<i>Figure 1-3: principals of transduction mechanism for biosensors.</i>	4
<i>Figure 1-4: Schematic of a total analysis device showing the various functions on a single microfluidic chip [7].</i>	5
<i>Figure 1-5: Gold-poly (PDMS) nanocomposite and its SEM image.</i>	7
<i>Figure 1-6: Typical spectrum of Au-PDMS nanocomposite. The peak absorbance is at of 533 nm.</i>	7
<i>Figure 1-7: The limit of detection in moles and grams per millilitre versus the analysis time for the different types of biosensor for mechanical and non-mechanical sensors. (SPR: surface-plasmon resonance; SMR: suspended microchannel resonantor; NW: nanowire; LFA: lateral flow assay; MRR: microring resonator; QCM: quartz crystal microbalance; BBA: biobarcode amplification assay; IFA: immunofluorescent assay; MC: microcantilever [1].</i>	9
<i>Figure 1-8: A suspended microchannel translates mass changes into changes in resonance frequency [48].</i>	11
<i>Figure 1-9: Schematic of the main steps of the biosensing experiment and their corresponding spectra; (A) Four steps of biosensing protocol; (B) Au-LSPR band corresponding to the steps depicted in A; (C) legend of the schematics.</i>	14
<i>Figure 1-10: The main objectives of this thesis.</i>	18
<i>Figure 2-1: Prepared and incubated samples in an ethanol (left) and aqueous (right) solution of the gold salt (incubated for 48h in 0.6% in ethanol solution and 1.0 % in aqueous solution).</i>	30
<i>Figure 2-2: The influence of threshold on the porosity evaluation.</i>	33
<i>Figure 2-3: Evolution of the in-situ reduction reaction. The inset shows the setup of the measurement. (a) Evolution of the spectral pattern for gold prepared from the solution of the gold precursor in ethanol, (b) Evolution of the spectral pattern for the synthesis of gold from an aqueous solution of the precursor.</i>	36
<i>Figure 2-4: Evolution of the reduction reaction (a) Absorbance versus time of the Au LSPR band for the synthesis in ethanol solution “ethanol sample”, (b) Absorbance versus time for the synthesis in aqueous solution “water sample”.</i>	37
<i>Figure 2-5: SEM images showing the evolution with time of the size of nanoparticles prepared from the ethanol solution of the gold precursor.</i>	37
<i>Figure 2-6: Average size of gold nanoparticles versus time.</i>	38
<i>Figure 2-7: SEM images of Au-PDMS samples before annealing (a) prepared from ethanol solution, (b) prepared from an aqueous solution. The inset shows an enlarged image prepared from an aqueous solution, showing Au nanoparticles with different shapes.</i>	39
<i>Figure 2-8: SEM image of ethanol sample after annealing at 300°C.</i>	40
<i>Figure 2-9: Au LSPR band corresponding to the Au-PDMS film prepared from (a) ethanol solution (b) aqueous solution. (Black curve; as prepared, blue curve; annealed sample and red curve; annealed and swollen sample).</i>	41

Figure 2-10: SEM image of the Au-PDMS swollen in toluene (a) surface image, and (b) cross-section image .....	41
Figure 2-11: Module of elasticity of Au-PDMS nanocomposite .....	43
Figure 2-12: Porosity measurement for PDMS and gold nanocomposites.....	44
Figure 2-13: Sensitivity tests on the platforms prepared from ethanol solution. (a) as-prepared (b) annealed only (c) annealed and swollen. ....	45
Figure 2-14: Sensitivity tests on the platforms prepared from aqueous solution. (a) as-prepared (b) annealed only (c) annealed and swollen. ....	46
Figure 2-15: Biosensing experiments with the Au-PDMS platform prepared from the 0.8% ethanol solution of the gold precursor (was kept for 7h in the solution) (a) Au LSPR band corresponding to the annealed and swollen sample, (b) Au LSPR band corresponding to the Au functionalized with the linker molecule (11-mercaptoundecanoic acid solution in ethanol (5mM)) (c) Au LSPR band after adsorption of the antibody, and (d) after adsorption of the antigen.....	46
Figure 2-16: Biosensing experiments with the Au-PDMS platform prepared from the 1.5% aqueous solution of the gold precursor (was kept for 72h in the solution) (a) Au LSPR band corresponding to the annealed and swollen sample, (b) Au LSPR band corresponding to the Au functionalized with the linker molecule (11-mercaptoundecanoic acid solution in ethanol (5mM)) (c) Au LSPR band after adsorption of the antibody, and (d) after adsorption of the antigen. ....	47
Figure 3-1: Procedure for the preparation. The ethanol solution (60 $\mu$ L) of the gold salt (1%) is dropped on the PDMS surface (as shown in inset). The figure shows the solution expanded on the sample's surface, before irradiation. The samples are irradiated for different times varying from (a) 30s; (b) 60s; and (c) 90s. ....	54
Figure 3-2: (a) Spectra of samples prepared by keeping the solution on the PDMS surface for varying times. The existence of the Au LSPR band proves the formation of gold seeds on the surface; (b) the schematic of formation of gold NPs in the polymer matrix;(c) keeping the sample on room temperature after irradiation change the color of the sample: (1) immediately after MW irradiation; (2) 30min after irradiation; (3) 75min after irradiation. (d) Effect of the irradiation time (concentration of gold precursor is 1%) (left) and of the concentration of the gold salt in solution (irradiation time of 360 sec) (right) on the spectra of the samples. ....	59
Figure 3-3: SEM images of Au-PDMS nanocomposite, (a) as-prepared sample; (b) annealed sample at 300-350°C. The inset shows the distribution of particles on a large 2 $\mu$ m $\times$ 2 $\mu$ m area of the sample. (c) Effect of the annealing process on the position of the Au-LSPR band. ....	62
Figure 3-4: Sensitivity of nanocomposite sensing platforms (the nanocomposite is prepared by using a 1% gold precursor solution with an irradiation time of 90sec) for both as-prepared and annealed samples. The regression coefficient (R) is given for each graph.....	65
Figure 3-5: Schematic of the main steps of the biosensing experiment and their corresponding spectra; (A) Four steps of biosensing protocol; (B) Au-LSPR band corresponding to the steps depicted in A; (C) legend of the schematics. ....	66
Figure 4-1: Mixing mechanism; (a) T-shape mixer; (b) the proposed 3-layer micromixer. Each inlet is split into two sub-streams. The streams are finally recombined at the outlet. ....	72
Figure 4-2: The 3D view of the micromixer. (a) The variables namely, the width of the channels ( $W_1$ – $W_4$ ) have to be optimized to have equal contributions from the inlets to maximize the mixing performance, (b) four available paths ( $p_1$ to $p_4$ ) from inlets to the outlet, (c) micromixer dimensions used for optimization. ....	73
Figure 4-3: Performance assessment of mixing; (a) T-type micromixer, (b) proposed micromixer. ....	78

Figure 4-4: Simulation results at flow rate of 20 $\mu$ l/min; (a) T-type mixing with $\eta$ =20.9%, (b) the proposed micromixer ( $\eta$ =76.3%).	79
Figure 4-5: Comparison of mixing performance of the proposed mixer and a T-type micromixer at different flow rates.	79
Figure 4-6: Simulation of combination of several mixing units for achieving better mixing performance at a high flow rate of 50 $\mu$ l/min; (a) two units ( $\eta$ =82.5%) and (b) three units ( $\eta$ =91.6%).	80
Figure 4-7: Mixing performance with different combination of mixer units at different flow rates.	81
Figure 4-8: Fabrication process of the micromixer; (a) three SU-8 molds used for fabrication of the mixer (b) PDMS thin layer fabrication process to make the middle layer (80 $\mu$ m thick); (c) the fabricated device and the close-up shows how 3-layers are aligned to form the mixer.	82
Figure 4-9: Flow visualization of the proposed micromixer using green and red flows. (a) High flow rate of 400 $\mu$ l/min ( $Re$ ~55) to minimize the diffusion for better visualization; (b) The thickness of the green flow is decreasing along the flow which shows the green flow is diffusing into the red at rate of 40 $\mu$ l/min ( $Re$ ~5.5).	84
Figure 4-10: Evaluation of the micromixer performance in real conditions; (a) a layout with four branches designed to precisely measure the variation of pH in the cross-section of the mixer outlet, (b) measured pH used for estimation of efficiency. The black line shows measured values and the hatched area represents the mixed fluids, (c) The variation of efficiency along the outlet cross-section and the average efficiency for each flow rates, (d) the fabricated device.	86
Figure 5-1: Fabrication procedure of microfluidic chip and measurement of its spectral band (a) Step-by-step fabrication procedure of SU-8 mold and PDMS microfluidics. The figure shows a chip with two channels (C400-2) and the red color of the channels indicates the synthesized AuNPs; (b) the microfluidic chip was placed directly in a spectrophotometer in order to measure the gold plasmon band.	93
Figure 5-2: Study of the kinetics of the reduction reaction; (a) Absorbance-time plots of the reaction in C400-1 corresponding to 1% and 2% gold salt concentrations at room temperature, (b) The effect of PDMS cross-linking agent on the evolution of gold nanoparticles formation (c) The effect of temperature on the evolution of formation of gold nanoparticles by using a 1% gold salt solution (d) Arrhenius plot for the calculation of apparent activation energy (e) comparison of evolution of the gold into PDMS in microchannel and in macro-scale environment, (f) Illustration of microfluidic chip cross-section and the migration of reducing agent toward the channel wall.	98
Figure 5-3: SEM images and particle size distribution of annealed cells; (a) a microchannel and formation of gold NPs on the channel surfaces. At the left side, the channel edge is shown and the inset shows the shape of particles. (b and c) SEM image and the corresponding size distribution of Gold NPs prepared by 2% solution of gold precursor for 48h of incubation for two different (c: microchannel and d: macro-scale) environments; (d) Au-LSPR band of nanocomposite prepared in microchannel and macro-scale environment.	102
Figure 5-4: Sensitivity tests of the 400-2 microfluidic cell prepared from 2% aqueous solution of gold for 48h.	103
Figure 5-5: Biosensing experiments performed by using the annealed microfluidic biosensor (400-2 cells) prepared from 2% aqueous solution of the gold precursor (48h). (a) cross-section of a microchannel and AuNPs in the channel; (b) four steps of the biosensing protocol; (c) legend of the schematics; (d) Au-LSPR corresponding to the four sensing steps depicted in a; (e) LSPR band shift corresponding to different Ag concentrations.	105
Figure 6-1: (a) Design of a cantilever with buried microchannel; (b) cross-section of the cantilever.	111

Figure 6-2: Fabrication of SU-8 mold for thin cover layer of SPMF. ....	112
Figure 6-3: Fabrication of mold for the microfluidic-structure layer of SPMF. ....	114
Figure 6-4: Images of the fabricated mold for thin layers. The SU-8 mold for bottom thin layer is shown and its SEM images demonstrate two different SU-8 levels. The inset shows the top thin layer of the SU-8 mold. ....	115
Figure 6-5: thin layers fabrication procedure (a) fabrication of cover layer; (b) fabrication of $\mu$ F-structure layer; (c) PDMS-PDMS bonding of thin layers for form a closed microchannel. ....	116
Figure 6-6: Cover layer of the cantilever on a semi-salinized glass slide. ....	117
Figure 6-7: Fabricated $\mu$ F-structure layer with the microchannel features on a semi-salinized glass slide. The buried microchannel with the depth of 15 $\mu$ m is clear in the image. ....	117
Figure 6-8: Fabricated PDMS-microcantilever with buried microchannels. The thickness of cantilever is 165 $\mu$ m. ....	119
Figure 6-9: (a) Schematics of closure of the microchannel due to snapping problem of two thin layers; (b) the fabricated device while two layers are snapped. ....	120
Figure 6-10: Schematic of the SPMF cantilever and its dimension, (a) cantilever subjected to bending; (b) cross section of the cantilever. ....	122
Figure 6-11: The variation of parameter $d$ with respect to the thickness of cantilever cover layer $t_1$ . ....	123
Figure 6-12: FEM model of the microcantilever and its boundary condition. ....	124
Figure 6-13: Variation of elastic module of PDMS membrane against thickness [159]. ....	125
Figure 6-14: Simulation of a microcantilever with buried microchannel. A surface stress of $\sigma = 5$ mNm $^{-1}$ is applied on the surface of the channel walls. ....	126
Figure 6-15: optimization of the thickness of cantilever top layer for achieving the highest tip deflection. ....	127
Figure 7-1: (A) Fabrication steps of a PDMS microreactor for the synthesis of gold nanoparticles; (B) fabricated PDMS-microreactor chip of size 2 mm $\times$ 4 mm. ....	133
Figure 7-2: Schematic of synthesis of AuNPs in a microreactor. ....	134
Figure 7-3: Synthesis of gold nanoparticles in a microreactor. ....	134
Figure 7-4: Formation of gold nanoparticles in a microfluidic reactor and immediate adsorption of synthesized AuNPs onto the PDMS microchannel surface. The micrographs show that the insufficient mixing causes the nanocomposite to form only in the contact area of two analytes. ....	135
Figure 7-5: Introduction of pre-synthesized AuNPs into the SPMF; (a) Schematic of the integrated micromixer-microreactor-biosensor platform; and (b) The fabricated device (c) SEM image of the microreactor outlet channel wall. ....	137
Figure 7-6: Deflection measurement of the cantilever (a) Schematic of the experimental setup; (b) Device under test (DUT) in an experiment. ....	139
Figure 7-7: (a) A cross section of the microchannel and the position of AuNPs; (b) biosensing protocol; (c) legend of the figure; (d) schematic of the deflection of cantilever tip upon interaction of antigen-antibody [34]. ....	140
Figure 7-8: Au-LSPR spectra of the collected solution for two different concentrations and their corresponding SEM images. ....	142
Figure 7-9: Calculation of the cantilever bending by measuring the slope of the cantilever deflection. ....	143
Figure 7-10: (a) Response of the cantilever for the Ag concentration of 4nM; (b) three phases of biosensing including: Before injection of Ag, during the stress induction, and the final response. ....	145
Figure 7-11: Deflection of the cantilever tip due to different antigen concentration and calculation of detection limit. ....	146

<i>Figure 8-1: The limit of detection in moles and grams per millilitre versus the analysis time for the different types of biosensor for mechanical and non-mechanical sensors. (SPR: surface-plasmon resonance; SMR: suspended microchannel resonator; NW: nanowire; LFA: lateral flow assay; MRR: microring resonator; QCM: quartz crystal microbalance; BBA: biobarcode amplification assay; IFA: immunofluorescent assay; MC: microcantilever [1].</i>	152
<i>Figure 8-2: (a) A cross section of the buried microchannel of SPMF and the formation of AuNPs on the PDMS surface; (b) four steps of the biosensing protocol to immobilize Ab of the surface of AuNP; (c) legend of the figure; (d) schematic of the deflection of cantilever tip due to the interaction of antigen-antibody [34].</i>	155
<i>Figure 8-3: Schematic of the experimental setup for the deflection measurement of the cantilever</i>	156
<i>Figure 8-4: (a) Device under test (DUT); Image of the cantilever tip recorded by CCD camera</i>	157
<i>Figure 8-5: Illustration of the in-situ reaction at the cross-section of microcantilever and the migration of reducing agent toward the channel wall.</i>	158
<i>Figure 8-6: gold nanoparticle integrated microfluidic buried microcantilever biosensor. The SEM image shows the size distribution of AuNPs inside the channel.</i>	159
<i>Figure 8-7: calculation of the cantilever bending by measuring the bending of the cantilever.</i>	162
<i>Figure 8-8: Response of the cantilever while the gold NPs were obtained by an in-situ method in the channels of the cantilever.</i>	163
<i>Figure 8-9: Deflection of the cantilever tip due to different antigen concentration and estimation of the limit of detection.</i>	164

## List of Tables

<i>Table 2-1: Refractive index of different solvents used for sensitivity test.....</i>	<i>34</i>
<i>Table 2-2: Module of elasticity for PDMS with two different ratios (MPa).....</i>	<i>42</i>
<i>Table 2-3: Sensitivity of different types of Au-PDMS nanocomposites. ....</i>	<i>45</i>
<i>Table 3-1: Module of elasticity (E) for PDMS with two different ratios (MPa) and the effect of presence of AuNPs on the module of elasticity of PDMS.....</i>	<i>63</i>
<i>Table 5-1: The apparent rate constants of the formation of gold NPs at different temperatures.....</i>	<i>99</i>
<i>Table 8-1: The apparent rate constants of the formation of gold NPs at different temperatures.....</i>	<i>160</i>

## Nomenclature

AFM	Atomic Force Microscopy
SEM	Scanning Electron Microscopy
MEMS	Micro Electro Mechanical Systems
MC	Microcantilever
MFS	Microfluidic System
MUMPS	Multi-User MEMS Processing System
SPR	Surface Plasmon Resonance
LSPR	Localized Surface Plasmon Resonance
PDMS	Polydimethylsiloxane
AuNP	Gold Nanoparticle

# **Chapter 1: Introduction and Literature review**

## **1.1 Introduction**

### ***1.1.1 Mechanical transducers as biosensors***

Advances in microfabrication and nanofabrication technologies are enabling a wide range of new technologies. Over the past few years, progresses in the fabrication of transducers technology with a more comprehensive understanding of the governing rules of biomolecular interactions, has led to rapid advancements in biosensors developments [1].

Progresses in the microfabrication technologies made it possible to fabricate mechanical devices with typical dimensions of a few microns or even of sub-micron moving parts [1,2]. These advancements have led to move from fundamental problems in biological physics toward fabrication of practical sensors that can be batch fabricated.

Micromechanical biosensors take advantage of properties that appear in small scales when the size decreases [3]. The unique properties of mechanical biosensors or mechanical transducers are as follows. First of all, mechanical biosensors provide exquisite mass resolution. The minimum resolution (or the minimum detectable added mass) they can achieve is proportional to their mass. Nanomechanical systems (or in the more specific case of mechanical biosensors with nanometer size moving parts) can achieve less than picogram resolution while working in the vacuum [3]. The resolution

may decrease working in air and in fluidic environments. The minimum detectable mass can be stated in the form of sensitivity of the sensor [1].

Second, the compliance of the mechanical sensors-their ability to deform-related to their stiffness can be decreased in the order of three by scaling down the device dimensions. It allows us to measure forces as small as 10pN which make them sensitive enough to even detect single antigen/antibody interactions [1]. This thesis will focus on the utilization of the transduction mechanism through a popular class of biosensors: cantilever-based biosensors. These types of mechanical transducers have been commonly used in scanning probe microscopes, have become increasingly popular as transducers in chemical and biological sensors. Figure 1-1 shows an SEM of a typical silicon microcantilever used widely for different biosensing applications such as protein detection, antigen-antibody interaction, and DNA hybridization [4].

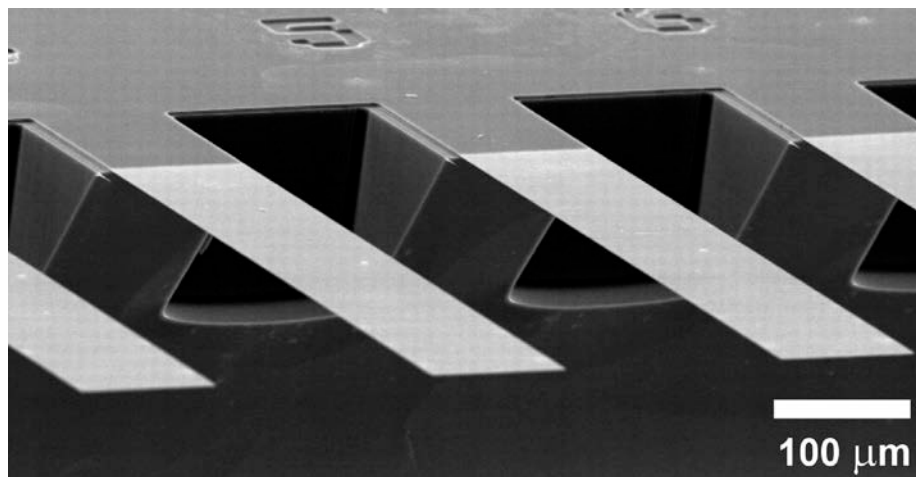


Figure 1-1: Scanning electron micrograph of a microfabricated silicon cantilever array (1  $\mu\text{m}$  thick, 500  $\mu\text{m}$  long, and 100  $\mu\text{m}$  wide, pitch of 250  $\mu\text{m}$ , spring constant 0.02  $\text{N m}^{-1}$ ; Micro- and Nanomechanics Group, IBM Zurich Research Laboratory, Switzerland) [4].

A microcantilever transducer directly converts changes in the Gibbs surface free energy created by cantilever's surface-analyte intermolecular interactions into a measurable

mechanical response [5]. The mechanical response is generally the bending of the cantilever that can be measured using different methods including optical, capacitance, and electrical. Figure 1-2 demonstrates how a microcantilever can be used for antigen-antibody interaction detection in a static mode of operation. Upon interaction of biomolecules on the cantilever's surface, a surface stress is induced which results in bending of the cantilever. The magnitude of bending deepens on the analyte concentrations [6].

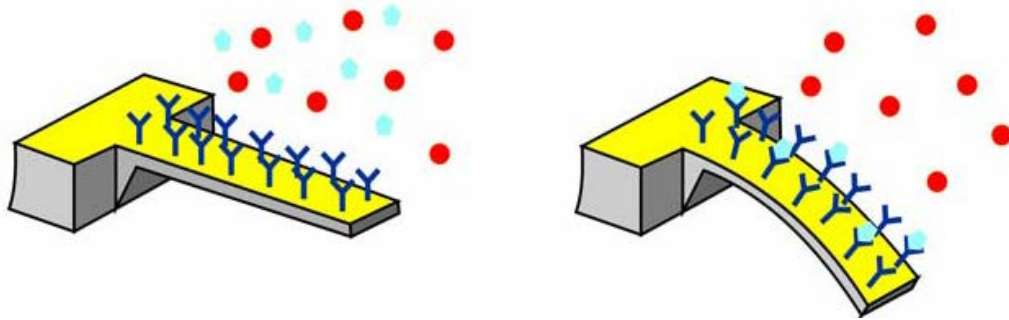


Figure 1-2: Labeled-free detection of Ag/Ab interaction into the surface of cantilever. The interaction generates a compressive surface stress, which causes the cantilever to bend [6].

In a mechanical transducer, the biosensing elements are immobilized on the transduction surface. Upon recognition of the biomolecules on the selective layer, a signal will be induced. This signal will be quantified in a measurable way by using different electronics. A schematic of a transduction mechanism is shown in Figure 1-3.

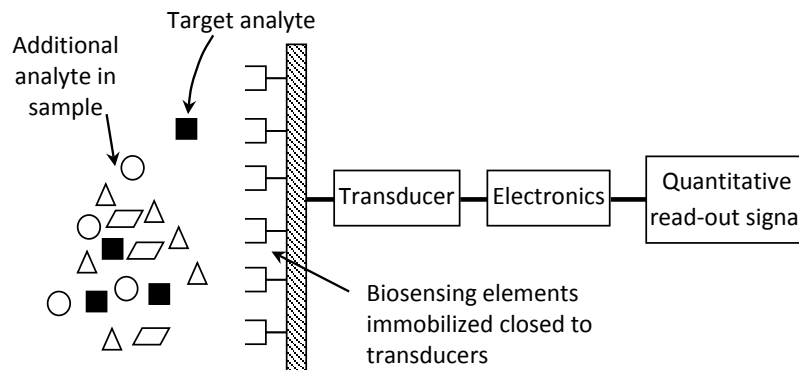


Figure 1-3: principals of transduction mechanism for biosensors

### ***1.1.2 Microfluidic systems for biosensing***

In the past twenty years, the exploration of biological systems from molecules, through cells, to small multicellular organisms has dramatically grown based on the developments in microfluidic systems. This enabling technology has several advantages compared with the conventional fluidic systems. Mainly it causes decreasing of the sample volumes and target analyte concentrations in ways that are not possible using conventional testing systems. Such a technology also has the benefit of scaling down the dimensions that enables a range of fundamental features to accompany system miniaturization such as reduced reagent consumption, high throughput, enhanced analytical performance, less waste, low unit cost, reduced energy consumption, and reduced dimensions when compared to macro-scale techniques [7].

In addition, small fluidic mechanical devices (or microfluidic systems) can show evidence of fast response times compared with macro-fluidic systems. They cause the chemical reaction or the biological interaction and processes to be observed on the time scales in the order of milliseconds or even less [4].

However, there are also some drawbacks by moving toward scaling-down of a fluidic system. Important disadvantages are the difficulties in mixing of different fluids of interest. The Reynolds number in microfluidic systems is typically in the range of 0.1~10 which mean that the flow regime is laminar (viscous flow) where the diffusion is minimum. Figure 1-4 shows a typical subsystem used to construct a microfluidic chip for bio-detection application.

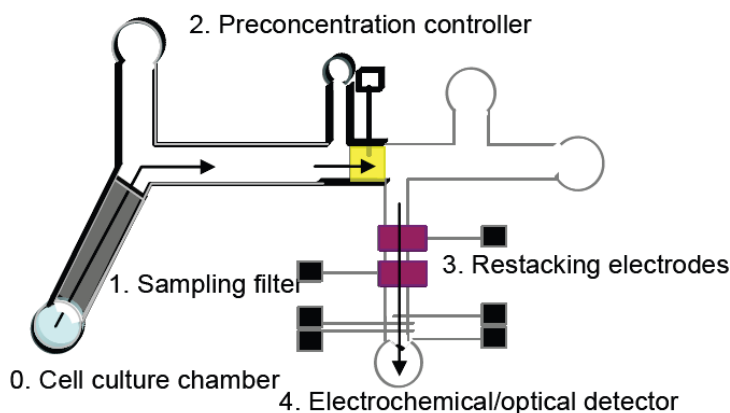


Figure 1-4: Schematic of a total analysis device showing the various functions on a single microfluidic chip [7].

### ***1.1.3 Gold Nanoparticles in biosensors***

Among different types of biosensors incorporated with various types of physiochemical transducers, optical biosensors are attracting more and more interest. Among those, sensors based on Surface Plasmon Resonance (SPR) have shown significant interest amongst researchers due to the unique advantages of these types of sensors such as simple detection mechanism and high possibility to be miniaturized and to be integrated with other lab-on-a-chip components [8].

These types of detection methods do not require any fluorescence labeling. In addition, the whole detection mechanism is accelerated, considering the potential to detect several targets in a complex biological sample [9].

The optical properties of gold colloids in the form of planar surface (SPR) as well as in the form of nanometer-sized particles (LSPR) are well established. With the advantages of SPR and localized SPR (LSPR), several studies focused on plasmonic properties of gold colloids [8].

In the last decade, nanometal-polymer composite films in the form of hybrid materials with inorganic nanoparticles immobilized and integrated into a polymer matrix attracted many researches in the field of life science for sensing applications [10]. Especially, gold and silver-poly (polydimethylsiloxane) PDMS nanocomposites are of considerable interest because of important PDMS properties including the simplicity of the preparation of PDMS-chips, low cost, good transparency, oxidative stability, and non-toxicity to cells [11]. Figure 1-5 shows a gold-PDMS nanocomposite and its SEM images. The corresponding Au-LSPR band of the composite is shown in Figure 1-6. There is an Au-LSPR band in the visible range (390 to 750 nm) for the gold at about 520nm.

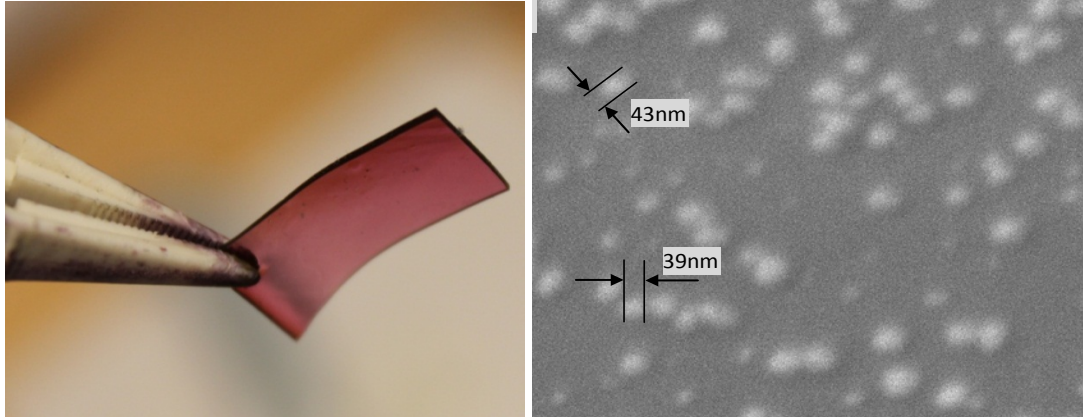


Figure 1-5: Gold-poly (PDMS) nanocomposite and its SEM image.

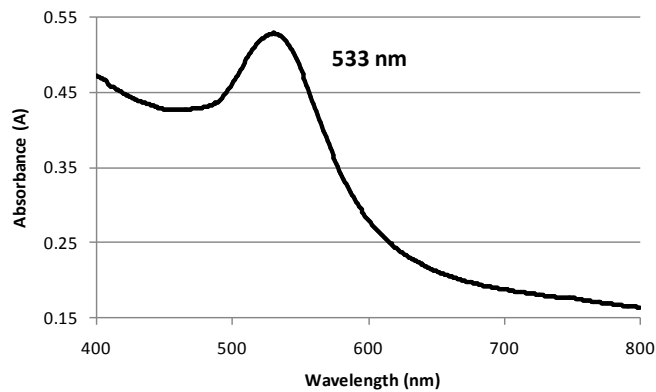


Figure 1-6: Typical spectrum of Au-PDMS nanocomposite. The peak absorbance is at of 533 nm.

In this thesis a biosensing platform is proposed based on three sensing mechanisms mentioned above. These mechanisms including: (1) mechanical transducers with high sensitivity and resolution, (2) microfluidic systems to reduce the required analyte volume with higher response time, and (3) gold-PDMS nanocomposites with their nontoxicity properties to cells and their high capability for immobilization of biomolecules on the surface of PDMS-based biosensing platforms.

## 1.2 Literature review

During the last decade, with the advancements in microfabrication, new biosensing mechanisms have been proposed. In this part we will look at some of papers which are close to our research.

### 1.2.1 *Micromechanical transducers*

Generally, bending of microcantilevers is induced by changes in the surface stresses while interaction between biomolecules such as proteins [5]. There are several papers which explained this induction effects in detail. Stoney pioneered presenting a simple model for this adsorption-induced surface stress and relates the stress to the cantilever deflection [12]. Many authors developed the model with more details or investigated the surface-stress behavior [13-19]. Very good reviews on MC, their applications and governing equations can be found in [1-3,20].

Micromechanical cantilever-based sensors operate in two modes: the *static mode* where the bending of the cantilever is measured and the *dynamic mode* where the change in resonance frequency of the cantilever is monitored [2]. The static mode is sensitive to surface stress changes and the dynamic mode is susceptible to mass variations [6]. There are different approaches for measuring the readout induced signal [21-25].

T. Thundat is one of the pioneers in the field of MC sensors and applications in biosensing. His papers in 1995 on the applications of MCs in chemical detection using resonance frequency shift opened a new window in the sensing applications of cantilevers [2,26,27]. However, the most developed microcantilever (MC) platform as biosensors

started in the sensing of 21st century. One of the most promising papers in this filed was published in 2000 by Fritz et al. [4]. In their paper, they presented a label-free method using an array of 8 cantilevers for DNA hybridization detection. They used a reference cantilever for multiple detection recognition. Their method has a sensitivity of 80nM for the complementary DNA oligonucleotide. The resulting beam deflection was measured by using optical methods and was in the range of 6-10 nm.

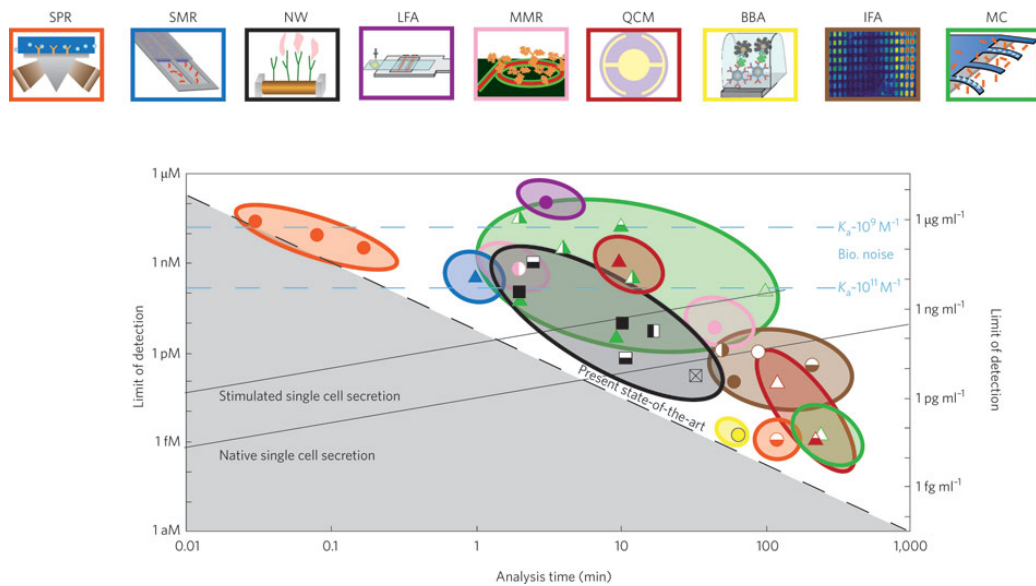


Figure 1-7: The limit of detection in moles and grams per millilitre versus the analysis time for the different types of biosensor for mechanical and non-mechanical sensors. (SPR: surface-plasmon resonance; SMR: suspended microchannel resonator; NW: nanowire; LFA: lateral flow assay; MRR: microring resonator; QCM: quartz crystal microbalance; BBA: biobarcode amplification assay; IFA: immunofluorescent assay; MC: microcantilever [1].

One of the important issues in the design of biosensors is the sensitivity of the sensor. A review paper recently published in [1] explains the sensitivity and resolution of different sensing mechanisms including both mechanical and non-mechanical biosensors. Figure 1-7 shows the detection limit of different biosensors presented in this paper. As it can be seen in this figure, SPR sensors generally have a very good response time (few seconds), but their detection limit is generally high. In contrast, in microcantilevers their detection

limit is very promising while their response time is in the range of few hours as the main drawback of this type of sensors.

To enhance the sensitivity of MC sensors, one method is to increase the surface area by adding nano-structures on the surface of the cantilever [5,28,29]. This would substantially increase the surface area of molecular interactions and results in a higher induced stress into the surface [5].

MCs have wide applications in sensing. There are many papers on different biosensing application [30] including virus detection [31,32], DNA hybridization [33-35], PSA detection [36,37] and Ag/Ab reaction detection [38,39]. There are other applications including analyte concentration detection [40], mass detection [41], and metal sensing [42].

### ***1.2.2 Microfluidic integrated cantilevers in biosensing***

Upon introduction of microcantilevers for biosensing, more advanced biosensors were developed by integration of microfluidics with microcantilevers. Burg [43], pioneered the integration of microcantilevers with microchannels in 2003 as a mass sensor. The integration of microfluidic systems with microcantilevers has a wide application in biosensing and especially in the field of mass detection [44,45]. The integrated system generally referred to suspended microchannel resonator (SMR) due to the main application of these types of sensors as a mass balancer. From Figure 1-7 it can be seen that the high response time of these systems is one of their main advantage of these types

of sensors. SMRs can achieve resolution down to femtogram ( $10^{-15}$  gram) [46] or even attograms [47] which makes them sensitive enough to detect even a single virus.

A paper published in 2007 [48] presented a suspended microchannel fabricated in silicon for single cell and nanoparticle mass detection. They used frequency shift method for detection. Figure 1-8 illustrates their mass measurement method.

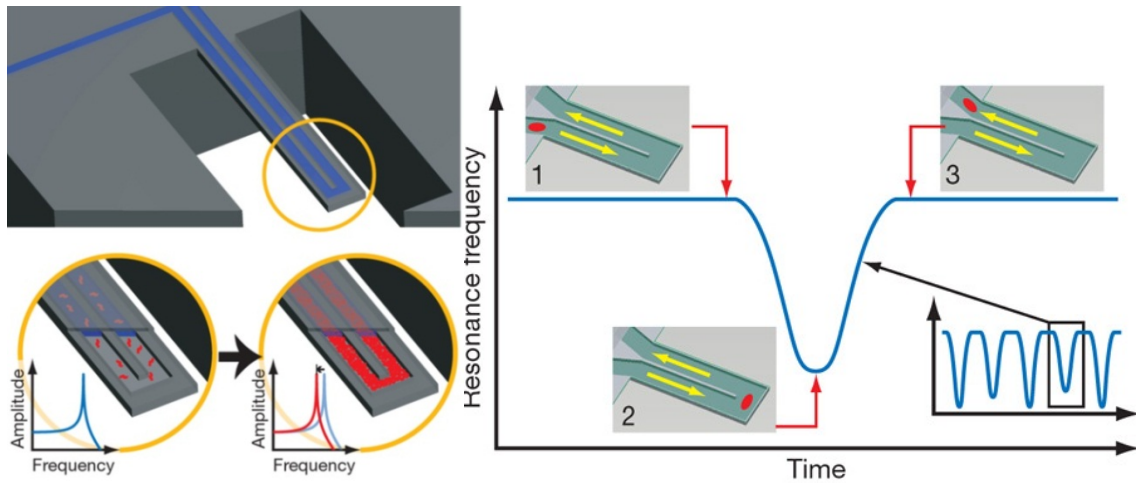


Figure 1-8: A suspended microchannel translates mass changes into changes in resonance frequency [48].

However most of the SMRs designed to be used as a mass balance, There are only very few papers on the application of microfluidic integrated cantilevers in different sensing applications. M. G. von Muhlen et al. [44] presented in 2010 a SMR for protein detection in serum where the glycoprotein ALCAM has been detected in undiluted serum at 300 pM concentrations in several minutes. Indeed there are many papers in mass sensing application of SMRs [49-51].

### ***1.2.3 Gold nanoparticles in biosensing***

One of the other issues that are the interest of this thesis is to use nanoparticles for biosensing. Metal-polymer nanocomposite or metal-polymer nanocomposite films are hybrid materials with inorganic nanoparticles immobilized and integrated into a polymer matrix. The interest in these hybrid materials, in particular, those based on gold, stems mostly from their optical properties. Applications of gold polymer and copolymer composites, for example, in water purification, targeted drug release, antimicrobial coatings have been reported as well [52].

Nanocomposites can be synthesized through different approaches [53-55], basically, either by *in-situ* methods, or by incorporating pre-made nanoparticles into a polymer matrix by using a common solvent. For a description of recent developments in the synthesis and applications of nanocomposite materials, see some excellent reviews and references herein [8-10,56,57].

Gold-PDMS nanocomposites are of considerable interest due to the simplicity of their preparation, low cost, good transparency, oxidative stability, and non-toxicity to cells. A major drawback is the strong hydrophobicity, and therefore, the inertness to biological molecules. To render the PDMS surface hydrophilic, functional groups have been introduced by low-pressure plasma treatments [58]. However, this effect is not stable and the hydrophobicity is regained over the time. Au-PDMS nanocomposites have been synthesized in various forms for applications including water purification and drug delivery [59]. Because of their strong plasmon band in the visible spectrum, arising from the excitation of plasmon by the incident light, gold nanoparticles (AuNPs) are

particularly suited for sensing applications. Due to the wide utilization of gold nanoparticles with various shapes in biosensing, biological labelling, etc., their association with PDMS, in the form of nanocomposite materials, opens new possibilities in microfluidic biosensing [11].

Generally, the biosensing properties of nanocomposites depend on quite a few parameters related to the conditions of their preparation, which is the nature of the precursor molecule, the concentration of the solutions, the temperature, the thickness of the film, etc. They are determinant for the distribution of the metal particles in the polymer matrix. On the other hand, and this is the most important issue, the polymer has to provide an appropriate environment for the metal nanoparticles in order to be able to interact with the biomolecules [60]. Because of its extreme hydrophobicity, PDMS does not promote the hydrophilic biomolecules to enter the inner domains of the polymer. However, it has been reported recently that, by varying the cross-linker concentration, the free volume of the film can be changed and the enclosure of various molecular entities can be facilitated [61].

AuNPs are very good candidate for detection of biomolecules in the form of Au-PDMS nanocomposite, when the AuNPs are immobilized on the surface of PDMS. Whowever, the interaction of nanoparticle and the surface is very important. For example, when the gold nanoparticles are embedded deep into the polymer, the biomolecules may be too far from the sensing volume of the particle. Since the biosensing properties are determined by the spatial distribution of the Au nanoparticles, it is important to be able to control this distribution. Therefore, the main goal is to explore some promising ways to increase the mobility of Au nanoparticles in order to concentrate most of them on the surface of the

film and thus, make them accessible to the surrounding environment containing the biomolecule of interest. Among them is the thermal treatment of nanocomposite [11]. LSPR-based biosensing (antigen/antibody interactions) consists of 4 main steps. In each step the LSPR of the nanocomposite will be recorded. The steps are schematically shown in Figure 1-9-a. The Au-LSPR corresponding for each step is also shown Figure 1-9-b. Generally for the sensing of biomolecules, the molecule of interest should be immobilized on the pre-immobilized gold nanoparticle. This will allow us to be able to locally follow the LSPR behavior of the Au-nanocomposite film while sensing protocol.

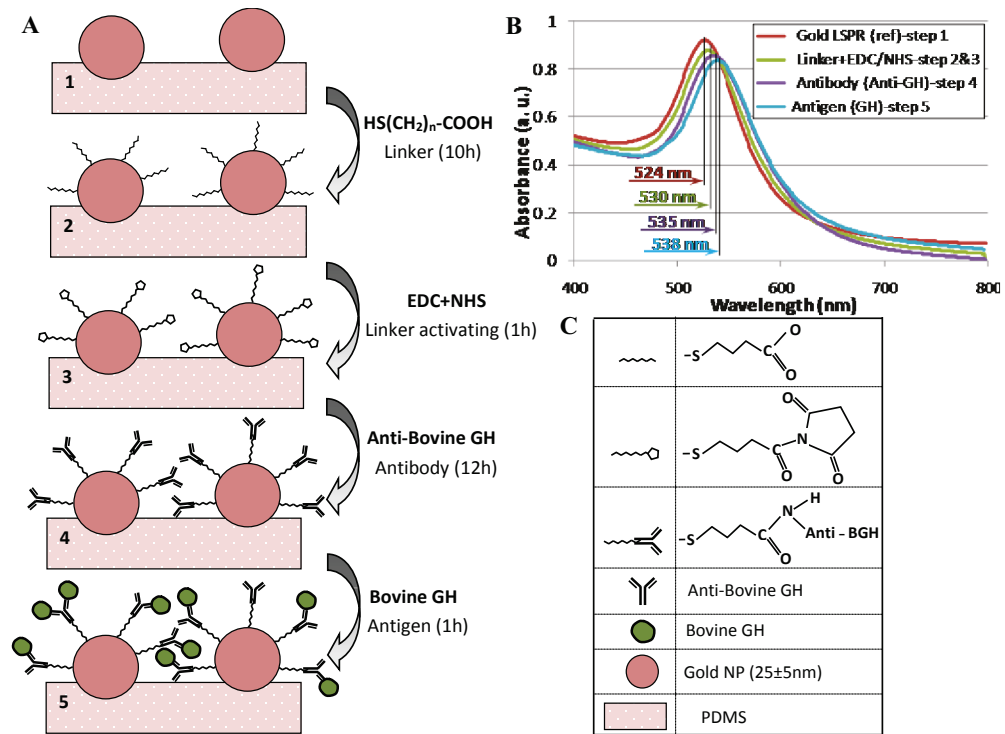


Figure 1-9: Schematic of the main steps of the biosensing experiment and their corresponding spectra; (A) Four steps of biosensing protocol; (B) Au-LSPR band corresponding to the steps depicted in A; (C) legend of the schematics.

There would be a plasmon red-shift between each step. More specifically, in the last step, the Au-LSPR shift is mostly due to the antigen/antibody interaction. The value of the

shift (in nm) is noble evidence for determining the sensitivity of the platform and is a function of the antigen concentration.

### **1.3 Thesis motivation**

From the first day that microcantilevers sensors were introduced as a new sensing platform by Thundat [26] to now, many types of miniaturized cantilevers have been fabricated either as a biosensor. However, one of the main drawbacks of cantilever biosensors is the high amount of analytes (proteins, DNA, polypeptides, etc.) that are required for sensing experiments as the cantilever must be submerged in the analytes. In addition, the cantilever bending read-out system (that can be optical or electrical) has to be designed sensitive enough to make it possible to measure deflection in the range of few nanometer [4] which limits the response time and sensitivity of the cantilevers as mentioned earlier [1].

To reduce the amount of analyte required for biosensing, integration of microchannels into the cantilever biosensors were presented in 2003. However, the main applications of these integrated cantilevers are limited to the mass detection through frequency shift measurement. It should be noted these integrated cantilevers are made of silicon which has a very high stiffness and therefore, the typical deflection of cantilever even for high concentrations of analyte is in the range of a few pm deflection ( $\approx 50\text{pm}$ ) [4]. This deflection is far beyond the limits of current measuring methods and therefore the application of suspended microchannels is limited to mass detection. Due to this, the term “suspended microchannel resonator (SMR)” is generally used for these types of sensors to show their application as a mass balance. Furthermore, the fabrication of buried

microchannel in a free-standing cantilever is complicated and encompasses several cumbersome fabrication steps.

Another point that should be considered is that while the microfluidic technology has been maturing well, a big surprise is that LoC systems are still not being used extensively. Recently Prof. G.M. Whitesides, in the editorial of *Lab on a Chip* [62], draws the attention of microfluidic researchers to the power of “*simple*” and “*cheap*” regarding the design of microfluidic devices that can be used extensively.

To the best of our knowledge, there is no method to integrate nanoparticles into a silicon microchannel to be able to immobilize the biomolecules in a SMR. This issue made it impossible to use SMRs in biomolecular recognition detection.

In this thesis, we propose a method for the fabrication of gold nanoparticles in a PDMS polymer. The method is then integrated in a microfluidic system to be able to immobilize gold nanoparticles on the surface of a PDMS microfluidic system. At the final stage, a polymeric cantilever biosensor with integrated microchannel is fabricated a sensitive biosensor. Due to very low elastic properties of the polymeric cantilever (around five order of magnitude less) compared to silicon, the deflection is much higher and therefore the sensitivity toward antigen/antibody interaction detection is extremely enhanced. Furthermore, the cantilever is fabricated through a simple method by using low-cost and biocompatible polymer (PDMS), which enable batch fabrication of the biosensors.

## 1.4 Thesis Objectives and Scopes

### 1.4.1 Objectives

The objective of present thesis is to develop a method to integrate gold nanoparticles on the surface of PDMS polymer inside a microfluidic system for biosensing application. The proposed method was finally applied into a suspended PDMS-microfluidics (SPMF) toward high sensitive detection of antigen/antibody interaction. Indeed, the sensor is a combination of nanotechnology and microfluidic chip into a microcantilever platform.

The proposed biosensor will be used to detect different molecular interactions, such as label free Ag/Ab interaction, DNA hybridization, DNA–protein interactions or protein–protein interaction, etc. In addition, there would be another application for the suggested microfluidic integrated cantilever such as a flow sensor for flow measurement. Also, the integrated system may be utilized for mass measurement with high mass resolution.

To move toward the main objective of this thesis work for fabrication of an integrated biosensor, we need the following sub-objectives to be answered:

1. Develop a method to synthesize AuNPs into the PDMS polymer network suitable for biosensing application
2. Integration of AuNPs in a microfluidic chip suitable for biosensing application
3. Fabrication of microcantilever with built-in channels
4. Integration of the developed microfluidic synthesis method of gold NPs (objective 2) with the fabricated cantilever platform (objective 3)
5. Biosensing (Ag/Ab interaction) experiment on the integrated biosensor

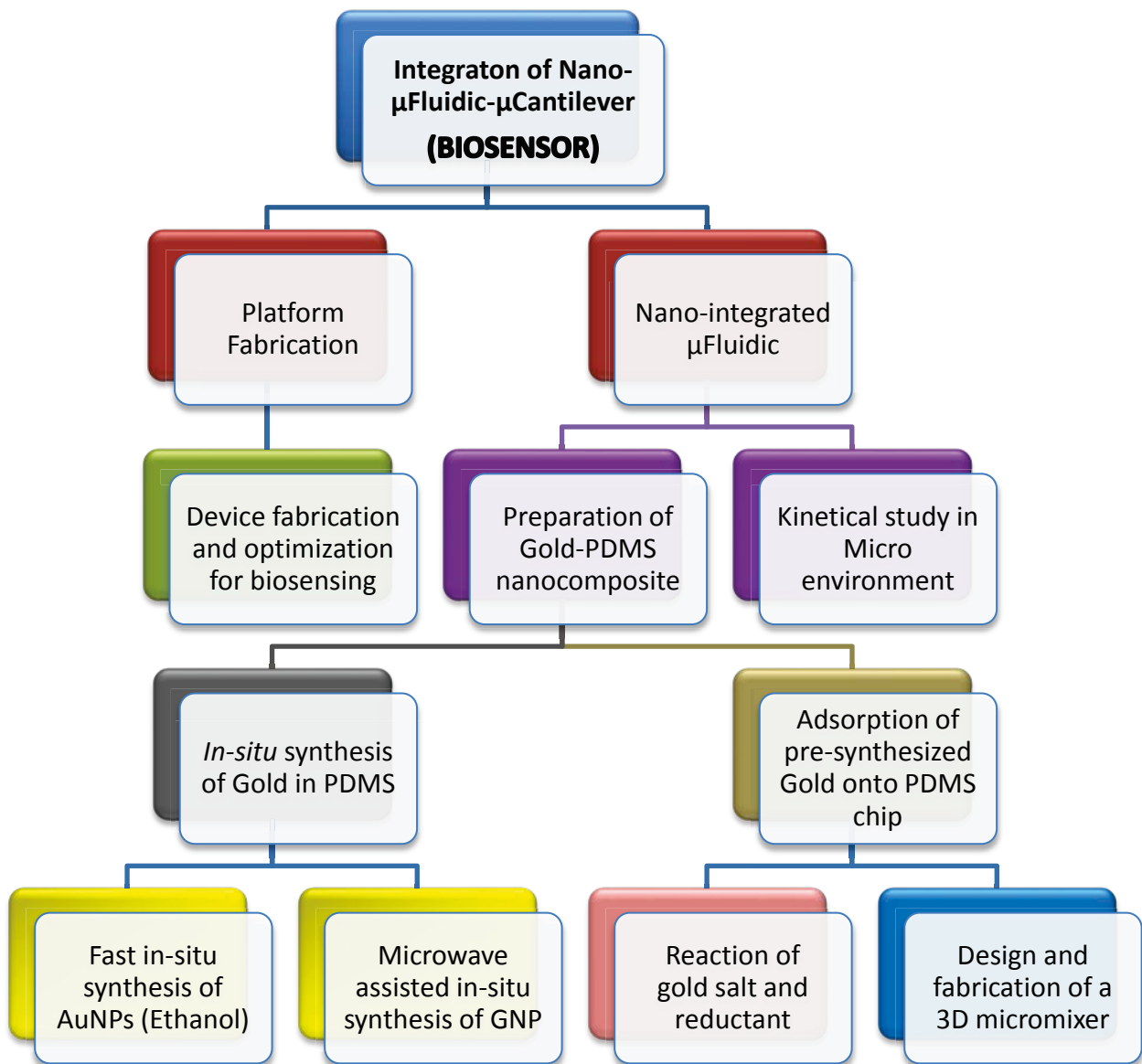


Figure 1-10: The main objectives of this thesis.

The main objective of this thesis and their dependent sub-objectives are also shown hierarchically in Figure 1-10.

### ***1.4.2 Sub-objectives***

Each objective contains several sub-objectives (as depicted in Figure 1-10). As mentioned, the first main objective is to develop a method for the synthesis of AuNPs in macro scale. To reach to this objective, we used two main approaches which including explained herein in detail: (1) *in-situ* method for gold-PDMS nanocomposite preparation based on reductive properties of PDMS; (2) Adsorption of pre-synthesized (pre-made) gold nanoparticle onto the PDMS. The sub-objectives are explained more herein:

1. Fabrication of gold-PDMS nanocomposite by *in-situ* methods: In these methods the gold particles are embedded in polymer network (they are immobilized into the polymer network). AuNPs are *adsorbed* into the polymer matrix. Several post-processing treatments can be performed on the nanocomposite to enhance the sensitivity of the fabricated platform.

Two different *in-situ* methods were presented in this thesis for preparation of gold-PDMS nanocomposite on the basis of reductive properties of PDMS including:

- (a) Using ethanol for fast synthesis of gold
- (b) Microwave-assisted *in-situ* synthesis of gold into PDMS.

2. Synthesis of gold nanoparticles to make the gold nanoparticle solution. The pre-synthesized particle then will be *adsorbed* onto the polymer surface. After the immobilization of the AuNPs on PDMS surfaces, they can be used for biosensing applications.

The gold nanoparticles were first synthesized inside a fabricated microreactor. The synthesis reaction performed inside the microreactor upon injection of gold salt and a reductant. However due to insufficient mixing, the size distribution of AuNPs was not

satisfactory and also the gold nanoparticles did not adsorbed onto the whole PDMS microfluidic chip. So, a micromixer where designed to improve the mixing of gold salt and reductant in order to improve the size distribution of synthesized nanoparticles.

3. In the next step, the *in-situ* method for fabrication of gold-PDMS nanocomposite was selected to be integrated into the microfluidic chip. The kinetics of the reaction in a microfluidic environment was studied thoroughly.

4. A method was proposed to fabricate PDMS microcantilever with an buried microchannel. The thickness of microcantilever was optimized for the highest response in terms of deflection.

5. Integration of pre-synthesized nanoparticles into the buried microfluidics of microcantilever. The integrated biosensor will be used for antigen-antibody interaction detection.

6. The nanoparticles will be integrated into the PDMS microcantilever by using the proposed *in-situ* method. Biosensing experiments were performed under different conditions to obtain the detection limit of the proposed biosensor.

## **1.5 Thesis contributions**

The main contribution of this thesis, for the very first time, an effective and sensitive polymeric microcantilever biosensor was presented with high sensitivity toward antigen/antibody interaction detection of growth hormones. The sensor development was made possible by introducing a new *in-situ* method for the fabrication (immobilization) of gold nanoparticles (AuNPs) on the surface of PDMS inside a microfluidic system.

Due to very low elasticity of the polymer (around five orders of magnitude less) compared to common silicon cantilevers, the deflection is extremely increased (about three orders of magnitude) and therefore the sensitivity notably improved.

The sub-contributions are categorized as follows:

- 1- A new method to enhance the biosensing properties of gold-PDMS nanocomposite by using ethanol solution.
- 2- A microwave-assisted *in-situ* method was presented for the fast fabrication of gold-PDMS nanocomposite with high sensitivity for bovine growth hormone detection.
- 3- A simple and cheap PDMS cascaded micromixer was proposed, modeled, fabricated and characterized with high efficiency in wide range of flow conditions.
- 4- The kinetics of *in-situ* synthesis of AuNPs in a microfluidic environment was studied in detail and the activation energy of the process was estimated experimentally.
- 5- A novel method presented for the fabrication of PDMS cantilever with an buried microchannel by using a 2-layered SU-8 mold.

The content of this thesis is written based on one published journal articles [63], one book chapter published by Wiley [64], two preliminary accepted journal articles [65], one under review journal article [66,67], and one journal article to be submitted [68].

## **1.6 Organization of the Thesis in Manuscript-based format**

This thesis is submitted in a manuscript-based format. In another word, all the chapters (excluding first and last chapter) of this thesis, are duplicated from the manuscripts were published, accepted or manuscripts which are under reviewing process for publication in scientific journals.

In the present chapter, a brief introduction on the application of microcantilevers, microfluidic systems and nanotechnology in biosensing is presented. A critical literature review and comprehensive survey on the last advancements in microcantilever biosensing and sensitivity of biosensors and integrated systems is then discussed. Even though the literature review is not elaborated in Chapter 1, a detailed literature review corresponding to topics will be covered in respective chapters as this thesis is prepared in a manuscript-based format. Chapter 2 to Chapter 8 are duplicated from one published journal article, one published book chapter, three under review journal articles, and one journal article to be submitted. Chapter 9 includes the summery and conclusion of the thesis and recommendations for future works.

To address the objectives of the thesis defined in Section 1.4, the chapters are organized in a cohesive manner. Moreover, the structure of the thesis is formatted according to the “Thesis Preparation and Thesis Examination Regulations” of the School of Graduate Studies at Concordia University. In doing so, the sections, figures, equations, and tables of the duplicated articles are accordingly numbered to address the regulations of the thesis preparation. At the end of the chapters, rather than individual reference lists of the papers, a single comprehensive reference list is presented in the Bibliography section. The detailed content of each chapter is as following:

Chapter 2, entitled “PDMS-Gold Nanocomposite Platforms with Enhanced Sensing Properties”, covers Sub-objective 1a of the “Thesis Objective and Scope” in Section 1.4. This chapter is based on a manuscript published in Journal of Biomedical nanotechnology as follows:

- H. SadAbadi, S. Badilescu, M. Packirisamy, R. Wüthrich, “PDMS-Gold Nanocomposite Platforms with Enhanced Sensing Properties”, *Journal of Biomedical Nanotechnology*, 8, 1–11, 2012.

Chapter 3, entitled “Microwave-Assisted Fabrication of Gold-PDMS Nanocomposite for Plasmonic Biosensing”, covers Sub-objective 1b of the “Thesis Objective and Scope” in Section 1.4. This chapter is based on a manuscript published as a book chapter and an accepted manuscript to be published in *Journal of Nanoscience and Nanotechnology* as follows:

- H. SadAbadi, S. Badilescu, M. Packirisamy, R. Wüthrich, “Synthesis and Characterization of Gold-Poly (dimethyl siloxane) Nanocomposites Obtained by In-Situ Microwave-Induced Reduction of Gold Ions”, *Nanocomposites: In-Situ Synthesis of Polymer-Embedded Nanostructures*, Wiley, book chapter, 2013.
- H. SadAbadi, S. Badilescu, M. Packirisamy, R. Wüthrich, “Microwave-Assisted Fabrication of Gold-PDMS Nanocomposite for Plasmonic Biosensing”, *Journal of Nanoscience and Nanotechnology*, 13, 6880-6887.

Chapter 4, entitled “High performance cascaded PDMS micromixer based on split and recombination flows for lab-on-a-chip applications”, covers Sub-objective 2 of the “Thesis Objective and Scope” in Section 1.4. This chapter is based on a manuscript accepted to be published in *RSC Advances* as follows:

- H. SadAbadi, M. Packirisamy, R. Wüthrich, “High performance cascaded PDMS micromixer based on split and recombination flows for lab-on-a-chip applications”, *RSC Advances*, 3, 7296-7305.

Chapter 5, entitled “Gold nanoparticles integrated PDMS microfluidic chip for lab-on-a-chip plasmonic biosensing of growth hormones”, covers Sub-objective 3 of the “Thesis Objective and Scope” in Section 1.4. This chapter is based on a published paper in *Biosensors and Bioelectronics* as follows:

- H. SadAbadi, S. Badilescu, M. Packirisamy, R. Wüthrich, “Gold nanoparticles integrated PDMS microfluidic chip for lab-on-a-chip plasmonic biosensing of growth hormones”, *Biosensors and Bioelectronics*, 44 (2013) 77–84.

Chapter 6, entitled “Fabrication of PDMS microfluidic integrated microcantilever”, cover sub-objective 4 of the “Thesis Objective and Scope” in Section 1.4. This chapter is based on a complimentary file to be submitted to Nature Nanotechnology.

Chapter 7, entitled “Micromixer integrated microreactor for adsorption of nanoparticles onto microchannel”, cover sub-objective 5 of the “Thesis Objective and Scope” in Section 1.4. This chapter is based on a complimentary file to be submitted to Nature Nanotechnology.

Chapter 8, entitled “Toward Femtomolar (fM) Sensing of Biomolecular Recognition”, covers Sub-objective 4 of the “Thesis Objective and Scope” in Section 1.4. This chapter is based on a manuscript to be submitted to Nature Nanotechnology as follows:

- H. SadAbadi, M. Packirisamy, R. Wüthrich, “Toward Femtomolar Sensitivity by Integration of Microfluidics with a Polymeric Microcantilever Sensor”, *Nature Nanotechnology*, to be submitted.

## **Chapter 2: PDMS-Gold Nanocomposite Platforms with Enhanced Sensing Properties**

In the present chapter, an *in-situ* method for fabrication of Au-PDMS nanocomposite is proposed. The method is on the basis of reductive properties of the curing (cross-linking agent) of the PDMS compound. The method was applied on a macro-scale sample. Then the fabricated platform was post-treated and optimized for the biosensing application. In this chapter, the effect of water and ethanol as two different medium (carrier fluids) for the *in-situ* method was investigated and the merits and de-merits of each medium was discussed in detail.

### **2.1 Introduction**

Metal-polymer nanocomposite or nanometal-polymer composite films are hybrid materials with inorganic nanoparticles immobilized and integrated into a polymer matrix. The interest in these hybrid materials, in particular, those based on Au and Ag, stems mostly from their optical properties. Nanocomposites show optical nonlinearities and/or ultralow or ultrahigh refractive indices and are suitable for applications such as color filters, optical sensors, data storages, waveguides, optical strain detectors, thermochromic materials, etc. Other applications of gold and silver polymer and copolymer composites, for example, in water purification, targeted drug release, antimicrobial coatings have been reported as well [52].

Nanocomposites can be synthesized through different approaches, basically, either by *in-situ* methods, or by incorporating pre-made nanoparticles into a polymer matrix by using a common solvent. In addition, physical methods such as chemical vapor deposition, ion implantation and thermolysis have been successfully used [69,70]. For a description of recent developments in the synthesis and applications of nanocomposite materials, see some excellent reviews and the references herein [9,10,56,57].

Gold and silver– PDMS nanocomposites are of considerable interest due to the simplicity of their preparation, low cost, good transparency, oxidative stability, and non-toxicity to cells. In addition, PDMS, the host polymer, has a low glass transition temperature ( $T_g$ ), excellent flexibility, high thermal and oxidative stability, good hemo- and biocompatibility. A major drawback is the strong hydrophobicity, and therefore, the inertness to biological molecules. To render the PDMS surface hydrophilic, functional groups have been introduced by low-pressure (low-temperature) plasma treatments, corona discharge treatments, etc. to promote the filling of the microchannels with aqueous solutions and to facilitate PDMS microchip bonding as well [58,71,72]. However, while freshly modified surfaces show good or moderate wettability, this effect is not stable and the hydrophobicity is regained over the time. The hydrophobic recovery is usually accounted for by the migration of the low-molecular weight constituents from the bulk to the polymer surface. Au-PDMS nanocomposites have been synthesized in the form of gels, foams and films for applications including water purification and drug delivery [59]. Because of their strong plasmon band in the visible spectrum, arising from the excitation of plasmon by the incident light, gold nanoparticles are particularly suited for sensing applications. Due to the wide utilization of gold nanoparticles with various

shapes in biosensing, biological labeling, etc., their association with PDMS, in the form of nanocomposite materials, opens new possibilities in microfluidic biosensing. We and other groups have prepared Au-polymer nanocomposites by *in-situ* nanoparticle formation methods and obtained well-dispersed nanoparticles [11,73-75]. However, the bio-sensing properties of the as-prepared nanocomposite films have been found to be poor. We have shown in a previous paper that the sensitivity of the Ag – PDMS platforms can be increased by functionalization, followed by a post-synthesis thermal treatment at moderate temperatures, treatment that induces an important morphological change [76].

Generally, the biosensing properties of nanocomposites depend on quite a few parameters related to the conditions of their preparation. They are determinant for the distribution of the metal particles in the polymer matrix. On the other hand, and this is the most important issue, the polymer has to provide an appropriate environment for the metal nanoparticles in order to be able to interact with the biomolecules [60]. Because of its extreme hydrophobicity, PDMS does not promote the hydrophilic biomolecules to enter the inner domains of the polymer. However, it has been reported recently that, by varying the cross-linker concentration, the free volume of the film can be changed and the enclosure of various molecular entities can be facilitated [61].

It is well established that the decay length of the electromagnetic field for Localized Surface Plasmon Resonance (LSPR) sensors depends on the size, shape, and composition of nanoparticles and it is not more than 5-15 nm, permitting the detection of very thin layers of adsorbate molecules [77-80]. However, if the gold nanoparticles are embedded deeper into the polymer, the biomolecules may be too far from the sensing volume of the

particle. In addition, if the interaction between the particles and the polymer chains is too strong and the nanoparticles are entangled in the polymer network, their mobility may be restricted. Since the biosensing properties are determined by the spatial distribution of the Au nanoparticles, it is important to be able to control this distribution. We have explored some promising ways to increase the mobility of Au nanoparticles in order to concentrate most of them on the surface of the film and thus, make them accessible to the surrounding environment containing the biomolecule of interest. Among them is the thermal post-synthesis treatment of Au-PDMS nanocomposite that has been proved to be an adequate method to improve the distribution of Au nanoparticles in polymers. In our work, Au-PDMS nanocomposite materials are intended to be further used for microcantilever sensing and, therefore, a high degree of elasticity is required. For this reason, a lower concentration of cross-linking agent has to be used, and, the resulting low free volume of the polymer does not favor the introduction of a high amount of gold nanoparticles. Swelling experiments have been thought to be useful to expand the polymer network and allow aqueous solvents to infiltrate the material.

In this work, we are reporting our results on the improved *in-situ* synthesis of Au-PDMS nanocomposite and on the improved sensitivity of the platforms prepared with the morphologically modified material. At the same time, the relationship between the amount of gold nanoparticles and the mechanical properties and the porosity of the samples was established.

## 2.2 Experimental

### 2.2.1 Materials

Sylgard® 184 elastomer kit for PDMS fabrication is purchased from Dow Corning Corporation. Gold chloride trihydrate ( $\text{HAuCl}_4 \cdot 3\text{H}_2\text{O}$ ) is from Alfa Aesar and 1-pentanol, toluene, N, N-dimethylformamid 2-propanol and ethyl alcohol are from Sigma Aldrich.

### 2.2.2 Fabrication of PDMS and synthesis Au-PDMS

For polydimethylsiloxane (PDMS) fabrication, the base polymer and curing agent were mixed (with 10:1 ratio by weight). After mixing, the fabrication was followed by degasification of the mixture by using a vacuum desiccator for 10 minutes. To ensure the highest smoothness of the PDMS surface, a silicon wafer previously silanized in vapor phase is used as a mold. The degasified mixture was then poured in the flat mold. The thickness of PDMS was between 500  $\mu\text{m}$  to 1 mm. After a second degasifying process (10 minutes) the mold has been kept in oven at 70°C overnight for curing. Afterward, the cured PDMS was peeled off from the mold and cut in 1 cm $\times$ 4 cm samples.

Solutions of chloroauric acid were prepared with different concentrations (0.2% to 1.5%) for the aqueous solution and from 0.02% to 0.8% for the ethanol solution. For the fabrication of gold-PDMS nanocomposite, the samples were immersed vertically in the corresponding solutions, at room temperature for different times. Figure 2-1 shows the as-prepared samples from both solutions and during the incubation. The figure illustrates how fast the formation of gold is in samples immersed in ethanol solution compared with

the samples in aqueous solution. The time of incubation for both samples was 48 hours. For each group, at least four samples were prepared and tested for optical and mechanical characterization.

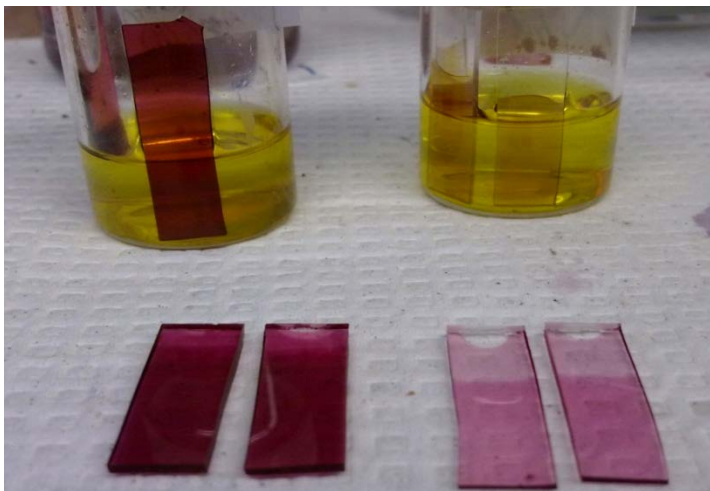


Figure 2-1: Prepared and incubated samples in an ethanol (left) and aqueous (right) solution of the gold salt (incubated for 48h in 0.6% in ethanol solution and 1.0 % in aqueous solution).

Basically, the curing agent in PDMS reduces the gold ions to the gold particles embedded into the polymer network. Due to the low amount of curing agent in PDMS prepared with a 10:1 ratio, low concentration of aqueous chloroauric acid will not result in the formation of the composite. Based on our experiments, concentrations lower than around 0.25% cannot be used for the synthesis. However for the ethanol solution, the composite can be prepared from solutions as diluted as 0.02%. For future reference, the gold samples prepared by immersing the PDMS in an aqueous solution of chloroauric acid will be referred as “water samples”. “Ethanol samples” refer to those prepared from ethanol gold salt solution.

As mentioned earlier, the amount of curing agent determines directly the rate of AuNP formation in the PDMS matrix, because it acts as a reducing agent. In other words, by increasing the amount of the curing agent (or fabricating PDMS with a ratio less than the

standard one of 10:1), the amount of gold on the PDMS surface can be easily increased. However, increasing the amount of the curing agent will result in a decreasing of PDMS elasticity. Mechanical tension tests have performed on PDMS to show the effect of curing agent on the elasticity.

The gold nanocomposites have been characterized by UV-Visible spectroscopy and Scanning Electron Microscopy (SEM).

### ***2.2.3 Post processing synthesis processes of the gold nanocomposite***

To enhance the properties of the Au-PDMS network for specific biosensing applications, two methods have been employed: annealing of the samples and expansion of polymer network by swelling.

#### **2.2.3.1 Annealing**

To improve the distribution of the gold nanoparticles embedded in the PDMS a heat treatment has been applied. To do this, the samples prepared using the *in-situ* method described in detail in section 2.2, have been heated gradually, from room temperature up to 300°C-350°C and then kept at the maximum temperature for 30 min.

#### **2.2.3.2 Swelling of Au-PDMS**

Another treatment performed on the PDMS samples was the mechanical expansion of the polymer matrix. The swollen samples have more free spaces in their polymer network compared with their non-swollen counterparts. In the free spaces, more nanoparticles can interact with the biomolecules and the sensitivity will be enhanced.

The annealed samples were weighed and then immersed in toluene for 24 hours. After removing the toluene from the surface of the sample with filter paper, the swelled nanocomposite was weighed and then kept for 24 hours in an oven at 60°C. The last step is performed to ensure that the toluene which diffused into the polymer has been completely removed. The dried sample was weighed again and the swelling ratio was calculated based on the following equation:

$$S = \frac{W_T - W_D}{W_D} \times 100 \quad (2-1)$$

Where  $W_T$  is the weight of each sample immediately after removing from toluene and  $W_D$  is the weight of each sample after the drying process. Repeated swelling and shrinkage cycles have been carried out as well.

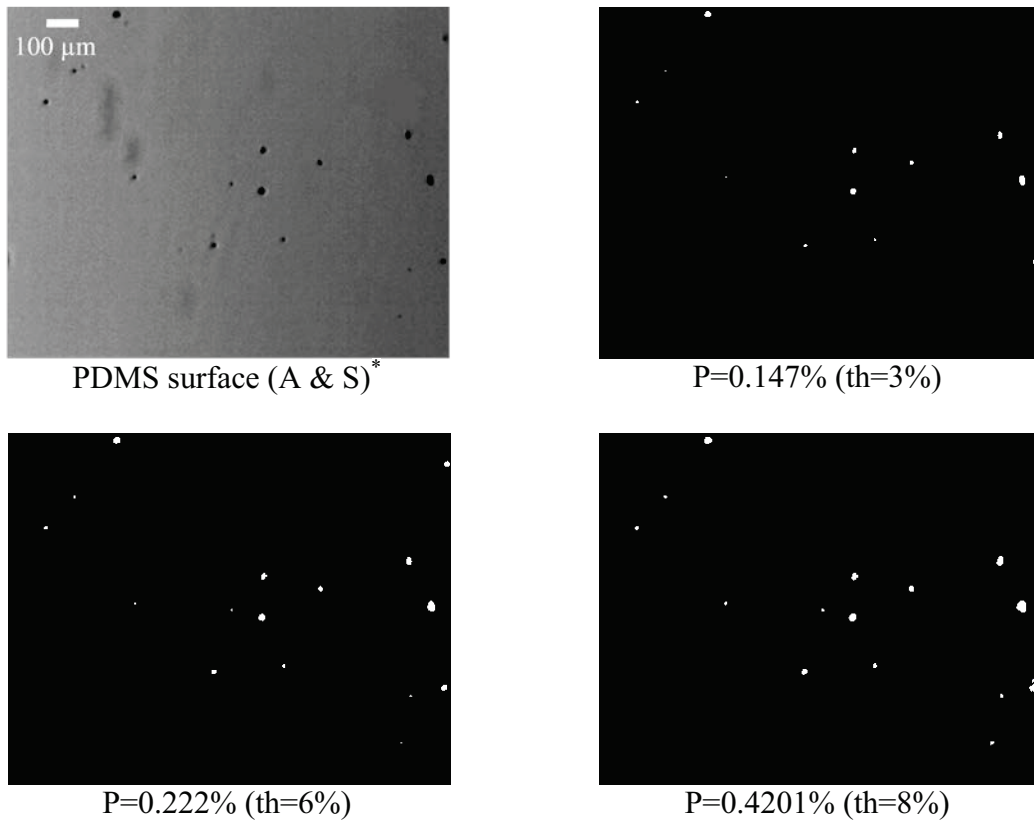
#### ***2.2.4 Tension test***

The tension test has been performed by using a BOSE ElectroForce® 3200 test instruments. The testing was performed on as-prepared and post-processed (annealed and swollen) samples. The stress-strain graph for each sample is obtained and the slope of the graph corresponds to the module of elasticity.

#### ***2.2.5 Porosity measurement***

To calculate the porosity, the surface images of the samples were used. A Matlab® code was used to discriminate between the area with and without porosity, by establishing a specific threshold (th). In the images, the area without porosity was assigned as black, while the area with porosity as white. The porosity is calculated as the ratio between

these two areas. The established threshold is affecting the boundaries between the PDMS surface and the pore areas. The value of the threshold is selected to have the best estimation of all pores in the modified image compared with the actual image. Figure 2-2 shows the effect of threshold on the porosity measurement of treated PDMS sample.



\* A & S = Annealed and Swollen

Figure 2-2: The influence of threshold on the porosity evaluation.

In this figure different values of threshold and the effect of thresholds on the size and number of pores is illustrated. Figure 2-2 shows that, when the threshold increases, porosity increases as well. The best value of the threshold that can estimate all the pores with their actual sizes has been found to be  $th = 6\%$  [81].

### 2.2.6 Sensitivity Tests

The sensitivity of the nanocomposite with respect to dielectric media with different refractive indices has been performed. For this test, six solvents have been selected. The refractive indices of these solvents are given in Table 2-1. The sensitivity can be obtained from the equation of the  $\Delta\lambda_{\max} / \Delta n$  dependency where  $\Delta\lambda_{\max}$  is the Au LSPR band shift in nm and  $\Delta n$  is the refractive index difference between the solvent and DI-water.

Table 2-1: Refractive index of different solvents used for sensitivity test.

<b>Environment</b>	<b>Refractive index (n)</b>
Deionized water	1.33
Ethyl alcohol	1.36
2-propanol	1.38
1-pentanol	1.41
N, N-Dimethylformamide	1.43
Toluene	1.50

### 2.2.7 Biosensing protocol

Biosensing experiments have been performed by utilizing the as-prepared annealed and swollen samples, in both water and ethanol solutions. The protocol that is used for biosensing is described below. The first step consists in the functionalization of gold nanoparticles with a 11-mercaptopundecanoic acid solution (NanoThink® ACID11) in ethanol (5mM), by immersing the sample in the solution for at least 5 hours. After attaching the linker, the conventional carbodimide coupling chemistry (EDC/NHS) is

used to activate the carboxyl groups, before attaching the antibody. The activation is carried out by keeping the sample in a 1:1 (vol) mixture of N-(3-dimethylaminopropyl)-N'-ethylcarbodiimide hydrochloride (EDC, 0.4M) and N-hydroxysuccinimide (NHS, 0.1M) for 2 hours. The next step consist of attaching the antibody (anti-bovine albumin antibody produced in rabbit in PBS) followed by attaching the antigen (albumin from bovine serum) by immersion in the corresponding solutions. The samples were washed with PBS between the steps.

## **2.3 Results and Discussion**

### ***2.3.1 In-situ synthesis and characterization of the Au-PDMS nanocomposite***

The *in-situ* fabrication process was studied by measuring repeatedly the UV-Visible spectra of the PDMS samples immersed in the aqueous solution of chloroauric acid (HAuCl<sub>4</sub>), directly in the cuvette of the spectrophotometer. The same measurements have been done by using a solution of the gold precursor in ethanol. The evolution of the reaction of formation of gold nanoparticles in the polymer matrix is shown in Figure 2-3. In this figure the LSPR band of each sample at different times is shown. Figure 2-4 reflects the kinetics of formation of gold nanoparticles by following the absorbance of Au LSPR band, in both water and ethanol solution of gold salt.

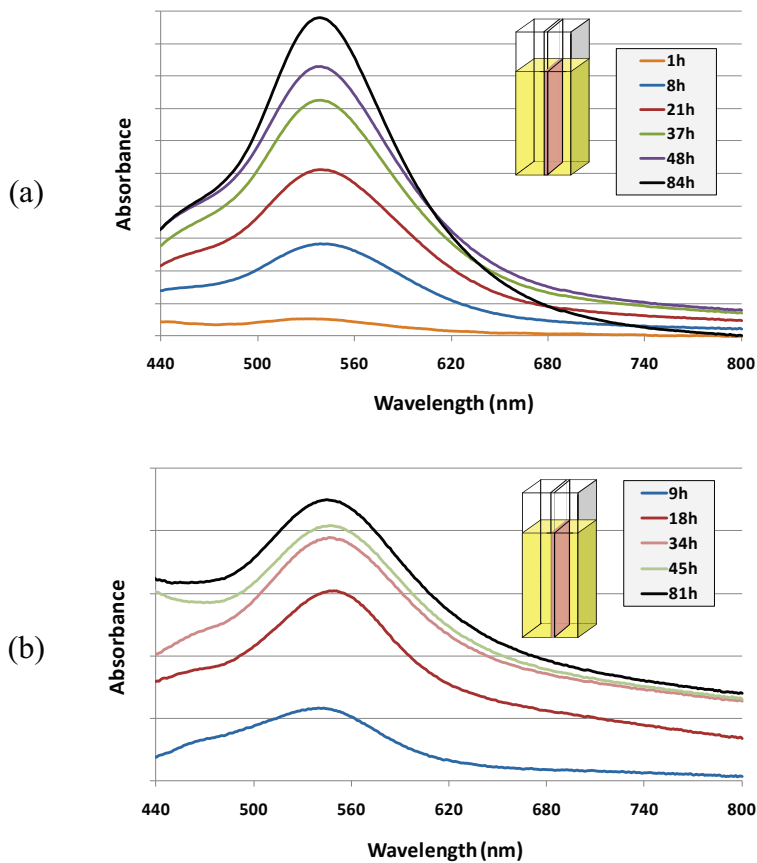


Figure 2-3: Evolution of the *in-situ* reduction reaction. The inset shows the setup of the measurement. (a) Evolution of the spectral pattern for gold prepared from the solution of the gold precursor in ethanol, (b) Evolution of the spectral pattern for the synthesis of gold from an aqueous solution of the precursor.

The results show that the reaction proceeds much faster when the gold precursor is dissolved in ethanol. Indeed, the slope of the first segment of the graphs corresponding to ethanol solution (Figure 2-4-a) is three times higher than that of the graph shown in Figure 2-4-b. In the ethanol solution, there seems to be three distinct stages: during the first 7 hours, the rate of the reaction is very high, the PDMS sample (self-standing film) is red and the color becomes stronger with the time. After that, the reaction rate slows down and the reaction is almost completed after 70 hours, depending on the concentration of the solution.

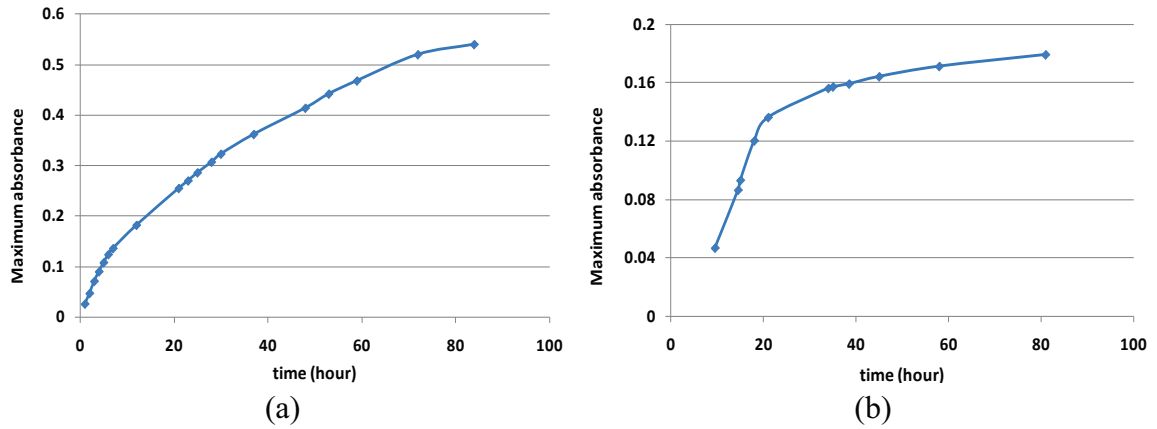


Figure 2-4: Evolution of the reduction reaction (a) Absorbance versus time of the Au LSPR band for the synthesis in ethanol solution “ethanol sample”, (b) Absorbance versus time for the synthesis in aqueous solution “water sample”.

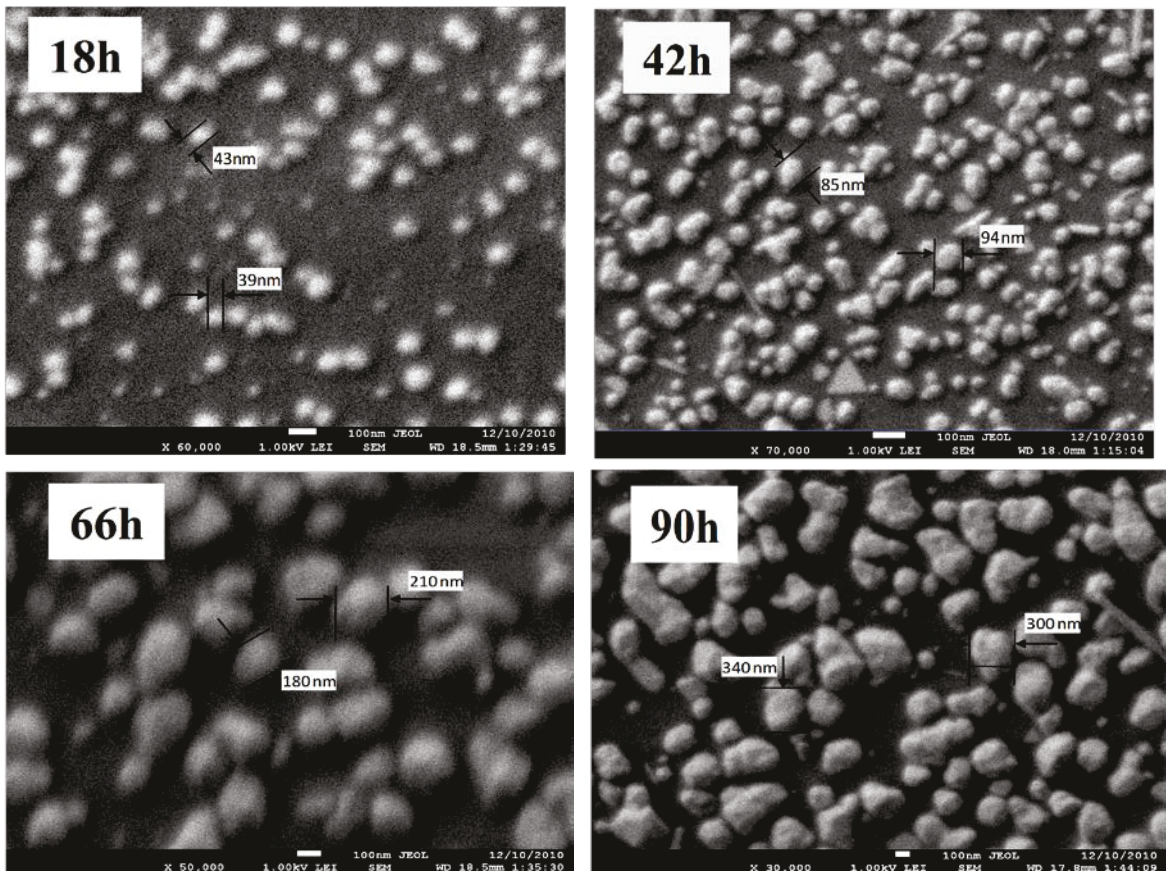


Figure 2-5: SEM images showing the evolution with time of the size of nanoparticles prepared from the ethanol solution of the gold precursor.

The reaction is much slower for the aqueous solution of the gold precursor and the color of the final sample is lighter showing a lower amount of Au nanoparticles, compared to the sample synthesized from ethanol. This result is in agreement with Tamai's data on the permeation rates of water and ethanol in PDMS membranes [82]. The authors have shown that, although the ethanol has a smaller diffusion coefficient than water, its permeation rate is larger because of the considerably larger solubility. It has also been reported recently that the difference between the permeation rates of water and ethanol is even larger in the case of PDMS nanocomposites [83].

To have more information about the distribution of nanoparticles on the PDMS surface, SEM images have been taken from the samples prepared from ethanol solution. Figure 2-5 shows the growth of gold nanoparticles during the *in-situ* synthesis for different incubating times (from 18 h to 90 h) from a solution of 0.4% gold precursor in ethanol. The increasing size of gold nanoparticles with respect to time is shown in Figure 2-6.

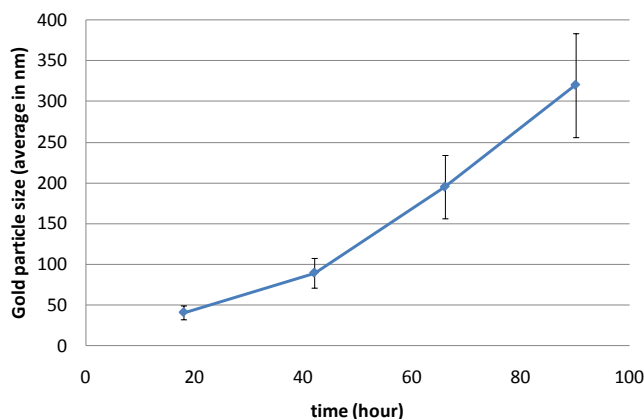


Figure 2-6: Average size of gold nanoparticles versus time.

The SEM images as well as the graphs in Figure 2-6 show that the Au particles grow considerably with the immersion time and form large aggregates.

### 2.3.2 Annealing and swelling of the as-prepared Au-PDMS nanocomposites

Our results show the importance of the order in which the post-synthesis treatments are performed. Sensitivity measurements on treated samples showed good results when the samples were annealed before swelling.

The nanocomposite samples prepared through the *in-situ* method are further annealed at high temperature. Figure 2-7-a and b shows the SEM images of ethanol and water samples, respectively, before annealing. Any temperature higher than 375°C would not be recommended as at this temperature the PDMS sample would start to deform.

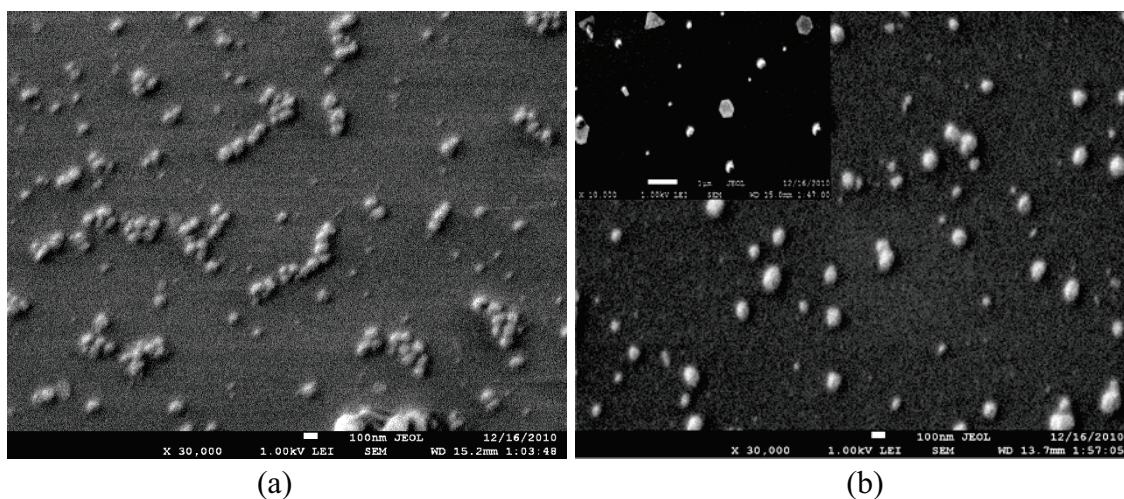


Figure 2-7: SEM images of Au-PDMS samples before annealing (a) prepared from ethanol solution, (b) prepared from an aqueous solution. The inset shows an enlarged image prepared from an aqueous solution, showing Au nanoparticles with different shapes.

As expected, the images show high density of Au nanoparticles on the surface of the samples prepared from the ethanol solution (Figure 2-7-a)

Figure 2-7-b shows that, while, the nanocomposites prepared from an aqueous solution contain well-dispersed Au nanoparticles with wide range of nanoparticle sizes, the sample prepared from an ethanol solution shows the presence of quite large aggregates,

mostly linear with almost the same particle sizes. After annealing the samples, the SEM images have shown that the aggregates are transformed in individual particles. And, the dispersion of Au nanoparticles in the polymer matrix is improved for all the samples.

The inset of Figure 2-7-b also shows that for the water sample sometimes there are some triangular and hexagonal nanoparticles, while, no asymmetrical nanoparticles have been seen in samples prepared from ethanol solution.

Figure 2-8 shows the SEM image of the annealed sample prepared in ethanol. It can be seen that the annealed samples contains well-dispersed nanoparticles compared with the non-annealed (Figure 2-7-a) samples.

The spectra of the as-prepared and annealed nanocomposites are given in Figure 2-9, together with the spectrum of the annealed sample swollen in toluene for 24 hours.

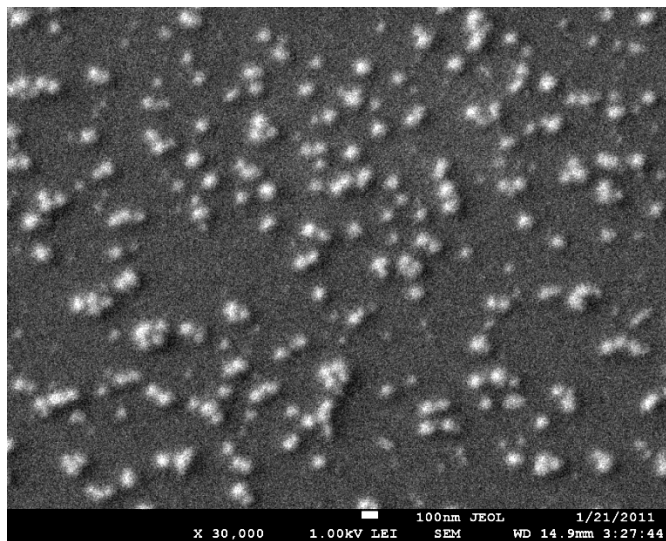


Figure 2-8: SEM image of ethanol sample after annealing at 300°C.

The figure shows that, generally, the Au plasmon band shifts to shorter wavelengths (blue shift) after both annealing and swelling in toluene. The blue shift after annealing, reflects the improved morphology, in terms of uniformity of the nanoparticles distribution as depicted in Figure 2-7-a (before annealing) and Figure 2-8 (after annealing).

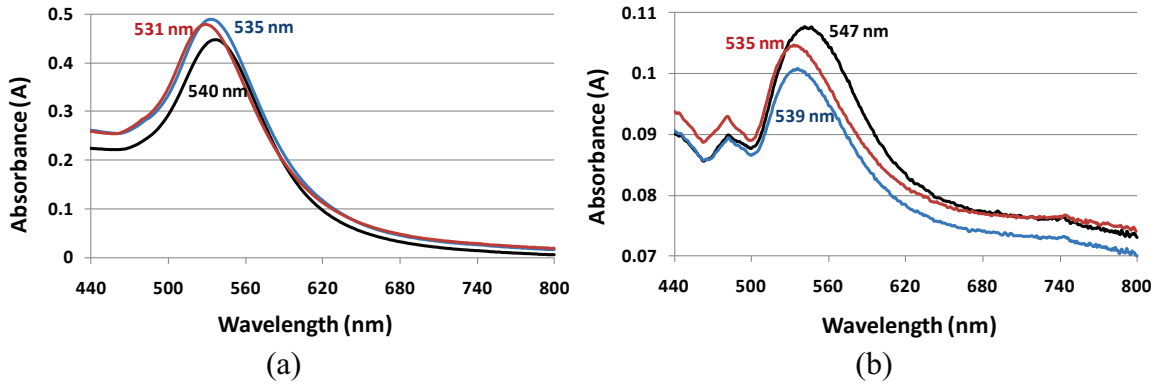


Figure 2-9: Au LSPR band corresponding to the Au-PDMS film prepared from (a) ethanol solution (b) aqueous solution. (Black curve; as prepared, blue curve; annealed sample and red curve; annealed and swollen sample).

In view of the biosensing experiments, the swelling and shrinkage of Au-PDMS nanocomposite samples was repeated several times and the corresponding swelling degrees were calculated. The SEM image of the swollen nanocomposite is shown in Figure 2-10.

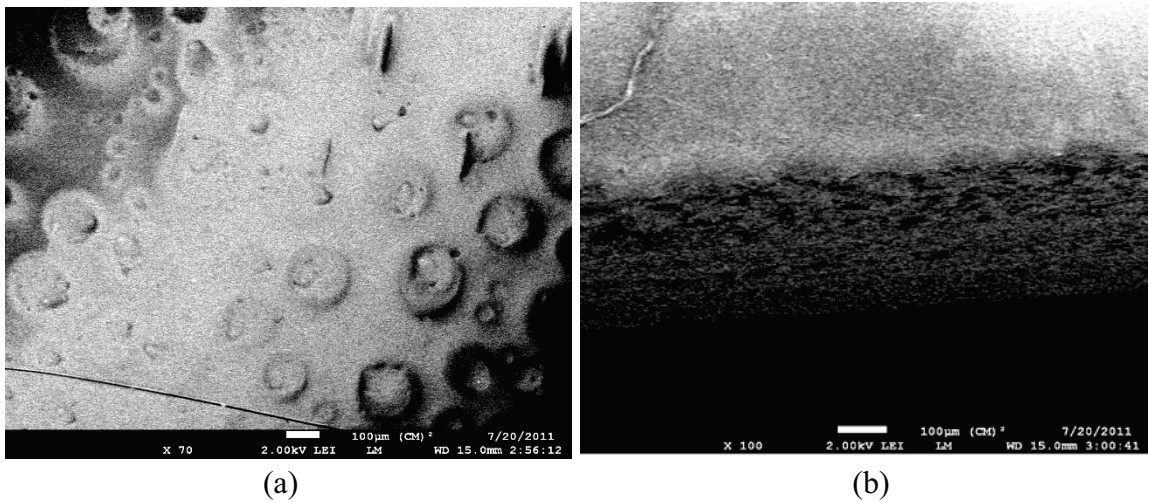


Figure 2-10: SEM image of the Au-PDMS swollen in toluene (a) surface image, and (b) cross-section image.

Figure 2-10 shows the voids (pores) formed in the polymer matrix after swelling. A number of “craters” like openings can be seen on the surface and a network of voids

traverse the whole cross-section of the film, confirming the increased inner surface of the polymer network.

The results of the swelling experiments show that, after 24 hours, the swelling degree is in the range of 48-54 % for both ethanol- and water-prepared samples, however, slightly (2-3%) lower for the samples prepared from the precursor dissolved in ethanol. The swelling degree could not be further increased by leaving the samples in toluene for another 2-3 days.

### ***2.3.3 Mechanical properties of PDMS and Au-PDMS nanocomposite***

To demonstrate the effect of the amount of the curing agent on the elasticity of PDMS, tension tests have been performed on samples prepared with two different ratios. The ratios of 10:1 and 4:1 are selected. The results are shown in Table 2-2. The results show that by using a higher ratio, samples with a higher elasticity will result. For each case, four similar samples were tested and the average value is shown in the table.

Table 2-2: Module of elasticity for PDMS with two different ratios (MPa)

Sample type	PDMS (10:1)	Aver. PDMS (4:1)
As-prepared	1.27 MPa	0.74 MPa
Treated (A & S)*	1.22 MPa	0.65 MPa

\* A & S = Annealed and Swollen

The tension test is used to show how the presence of AuNPs affects the mechanical properties of the samples. Samples (fabricated as described in section 2-2) were incubated in the ethanol solution of the gold salt (0.8%) for 24 and 72 hours, respectively.

Four identical samples were tested for both as-prepared and post-processed nanocomposites and the results are shown in Figure 2-11. In this figure, the error bar shows the maximum and minimum values measured for each case. The value of elasticity (in MPa) shows that, by increasing the amount of NGPs embedded into the PDMS matrix, the elasticity increased.

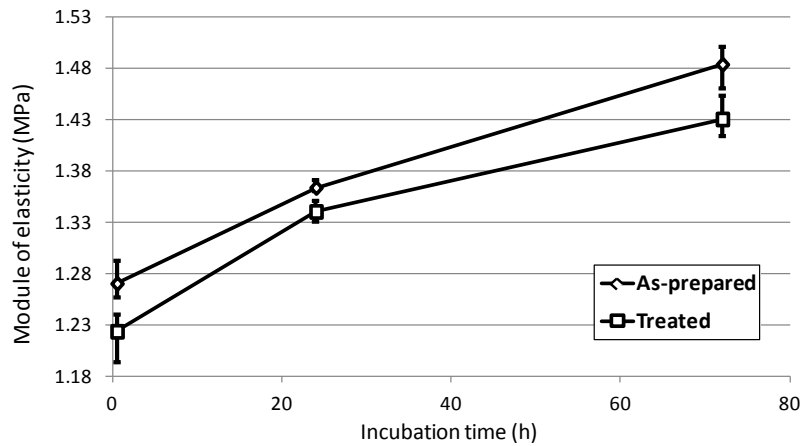
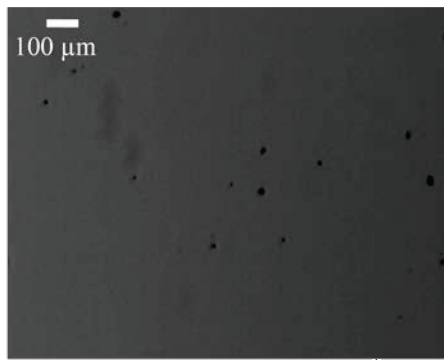


Figure 2-11: Module of elasticity of Au-PDMS nanocomposite

### 2.3.4 Porosity

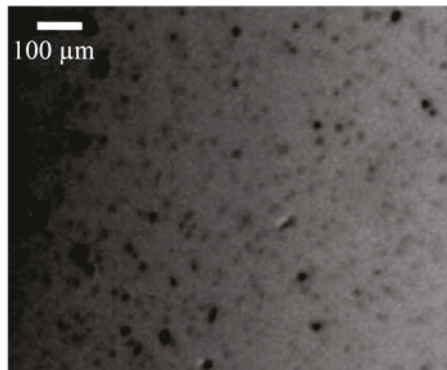
Figure 2-12 shows the porosity results. It can be seen that the porosity of the nanocomposite material is significantly higher than of the PDMS alone. The porosity of the nanocomposite ranges from 3.9% to 8.9% compared to the porosity of the matrix material which is only around 0.2%. This can be accounted for by the presence of the majority of gold nanoparticles on the surface of the sample.



PDMS surface (A & S)\*



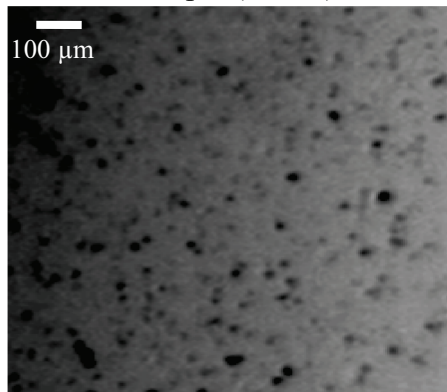
P=0.222 %



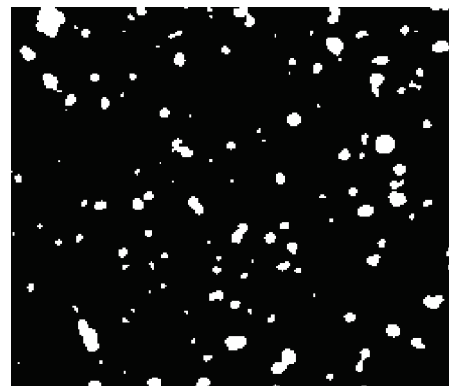
Ethanol sample (A & S)\* - 24h



P=3.896 %



Ethanol sample (A & S)\* - 72h



P=8.887 %

\* A & S = Annealed and Swollen

Figure 2-12: Porosity measurement for PDMS and gold nanocomposites

### 2.3.5 Sensitivity test

Sensitivity tests have been performed for samples prepared under various conditions and the results are shown in Figure 2-13 and Figure 2-14. The sensitivity values are summarized in Table 2-3.

Table 2-3: Sensitivity of different types of Au-PDMS nanocomposites.

Type of the sample	Sensitivity (nm/RIU)	R <sup>*</sup>
Ethyl alcohol	32	0.99
Ethyl alcohol (A) <sup>*</sup>	43	0.99
Ethyl alcohol (A & S) <sup>**</sup>	62	0.99
Water	46	0.95
Water (A) <sup>**</sup>	59	0.97
Water (A & S) <sup>***</sup>	71	0.97

\* Regression coefficient

\*\* A = Annealed

\*\*\* A & S = Annealed and Swollen

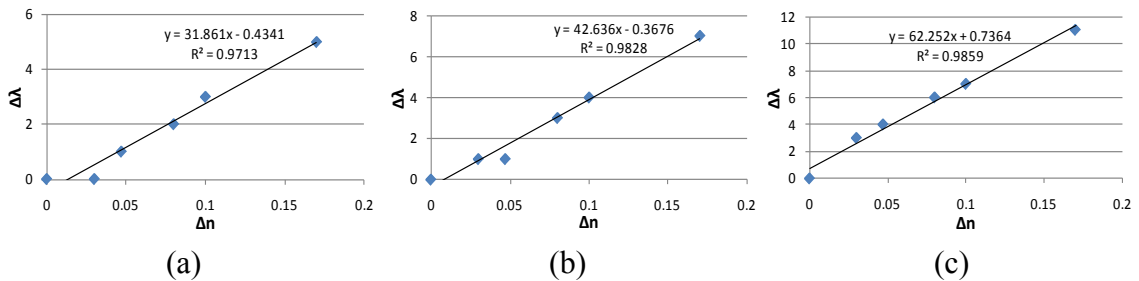


Figure 2-13: Sensitivity tests on the platforms prepared from ethanol solution. (a) as-prepared (b) annealed only (c) annealed and swollen.

The results indicated while the sensitivity results that are obtained for Au-PDMS nanocomposites prepared from an aqueous solution is a slightly better; however the regression coefficients of ethanol samples are higher than those in water. The relative low sensitivity values can be accounted for by the strong hydrophobicity of the polymer.

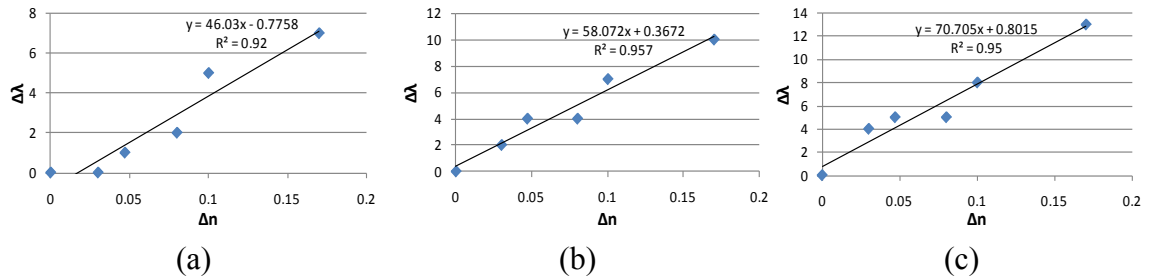


Figure 2-14: Sensitivity tests on the platforms prepared from aqueous solution. (a) as-prepared (b) annealed only (c) annealed and swollen.

### 2.3.6 Biosensing experiments

The samples prepared and treated as described above were tested for biosensing and the results are summarized in Figure 2-15 and Figure 2-16 for the samples prepared from the gold precursor dissolved in ethanol and water, respectively.

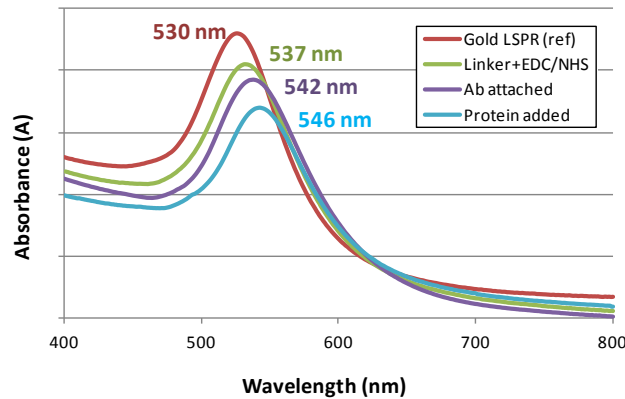


Figure 2-15: Biosensing experiments with the Au-PDMS platform prepared from the 0.8% ethanol solution of the gold precursor (was kept for 7h in the solution) (a) Au LSPR band corresponding to the annealed and swollen sample, (b) Au LSPR band corresponding to the Au functionalized with the linker molecule (11-mercaptoundecanoic acid solution in ethanol (5mM)) (c) Au LSPR band after adsorption of the antibody, and (d) after adsorption of the antigen.

The results showed a good sensitivity of the sensing platform toward biomolecular interaction. For ethanol sample the Au LSPR band red shifted from  $\Delta\lambda=7$  nm for the linker,  $\Delta\lambda=5$  nm after attaching the Ab and  $\Delta\lambda=4$  nm with attaching the complimentary Ag corresponding to the Ab. The shift to the longer wavelength in each case is due to the increased refractive index of the environment. During the last step (addition of the Ag) the shift is mainly due to the Ab-Ag interaction.

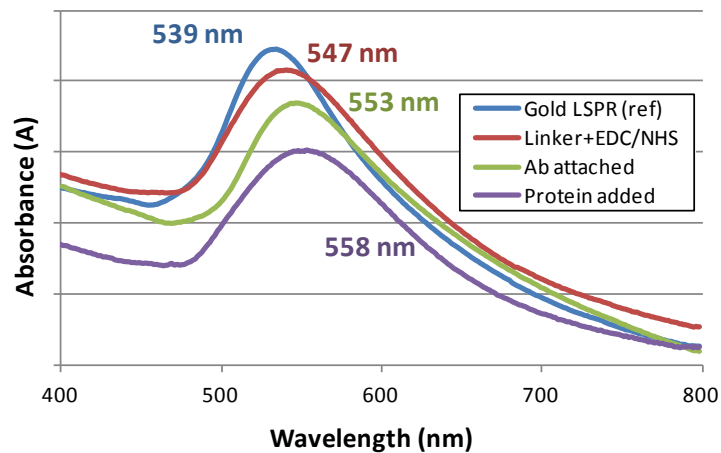


Figure 2-16: Biosensing experiments with the Au-PDMS platform prepared from the 1.5% aqueous solution of the gold precursor (was kept for 72h in the solution) (a) Au LSPR band corresponding to the annealed and swollen sample, (b) Au LSPR band corresponding to the Au functionalized with the linker molecule (11-mercaptopundecanoic acid solution in ethanol (5mM)) (c) Au LSPR band after adsorption of the antibody, and (d) after adsorption of the antigen.

For the water sample the shift was a few nm larger. The slightly higher sensitivity of the samples prepared from an aqueous solution can be accounted for slightly more expanded network upon swelling. In addition, the sample prepared from an aqueous solution may be less hydrophobic, possibly, because the migration of siloxane oligomers to the surface is prevented. However the samples prepared from ethanol solution have a high density of gold nanoparticles and microfluidic sensing of these samples are anticipated.

## 2.4 Conclusion

Au-PDMS nanocomposites were prepared through the *in-situ* method, by using the gold precursor dissolved, either in water or in ethanol. It is shown that, because of the high permeation rate of ethanol in PDMS, the rate of Au nanoparticles formation is significantly higher when the precursor is dissolved in ethanol. The nanocomposite materials were treated thermally and, subsequently swollen in toluene in order to improve the Au nanoparticles distribution in the polymer matrix and increase the free volume of the polymer. The results show that, because of the presence of gold nanoparticles, the nanocomposite's porosity is around 40 times higher than that of PDMS. In addition, the elasticity of nanocomposite has been found higher (around 20%) than that of PDMS. Sensitivity tests performed on different platforms showed that high sensitivities around 70 nm/RIU were obtained for both annealed and swollen samples. Biosensing experiments were carried out with the post-processed nanocomposites prepared with the two methods. Preliminary sensing experiments have demonstrated the good sensing properties of Au-PDMS nanocomposites. The results are relevant for the microfluidic sensing.

## **Chapter 3: Microwave-Assisted Fabrication of Gold-PDMS Nanocomposite for Plasmonic Biosensing**

In the previous chapter an *in-situ* method was proposed. However, one of the main drawbacks of the method was very long reaction time with water solution. However, we proposed a method to speed up the process by using ethanol medium and the results show the reaction accelerated more than one order of magnitude (around 10.5 time faster). We found serendipity, that it is possible to accelerate even more (about two order of magnitude improvement) the *in-situ* reaction using microwave radiation. In this chapter, a microwave-assisted method for the *in-situ* fabrication of Au-PDMS nanocomposite is proposed. The method applied on a macro-scale sample and the sensitivity of the platform was obtained as the platform was used further for biosensing application.

### **3.1 Introduction**

Metal-polymer nanocomposite films are hybrid materials with nanometer-sized inorganic nanoparticles (NP) immobilized and integrated into a polymer matrix. The scientific and technological interest in these hybrid materials, in particular, those based on gold, stems mostly from their optical properties. The inorganic nanoparticles used to enhance the optical and mechanical properties of the polymer are called “optically effective additives” and they lead to new functionalities of the polymer-based materials [84,85]. Nanocomposites are suitable for applications such as color filters, optical sensors,

stress/strain sensor, waveguides, thermo-chromic materials, water purification, and targeted drug release [52,86,87].

Nanocomposites can be synthesized through different approaches, either by *in-situ* methods, or by incorporating pre-made NPs into a polymer matrix, by using a common solvent. *In-situ* methods are beneficial to avoid the aggregation of inorganic particles inside the polymer matrix, leading to isolated primary particles. For a description of recent developments in the synthesis and applications of nanocomposites, see some excellent reviews and the references herein [9,56,57,88,89].

Gold and silver – polydimethylsiloxane (PDMS) nanocomposites are of considerable interest due to the simplicity of their preparation, low cost, good transparency, oxidative stability, and non-toxicity to cells [90]. A major drawback of PDMS is the strong hydrophobicity, and therefore, the inertness to biological molecules. To render the PDMS's surface hydrophilic, functional groups have been introduced by low-pressure plasma treatments, corona discharge treatments, etc. to promote the filling of the microchannels with aqueous solutions and to facilitate PDMS microchip bonding as well [58,71]. Because of their strong plasmon band in the visible spectrum, gold nanoparticles are particularly well-suited for sensing applications. Due to their wide utilization for biosensing, biological labeling, etc., their association with PDMS, in the form of nanocomposite materials, opens new possibilities in microfluidic Biosensing [90]. We, and other groups [11,63,74], have prepared Au-PDMS nanocomposites by *in-situ* nanoparticle formation methods and obtained well-dispersed nanoparticles with a narrow size distribution. In our previous papers [63] we have reported that the sensitivity of the

Au-PDMS platforms can be increased by performing a post-synthesis thermal treatment at moderate to high temperatures.

For sensing application, the polymer has to provide an appropriate environment for the metal nanoparticles, in order to be able to interact with the biomolecules [60]. Because of its extreme hydrophobicity, PDMS does not promote the strongly hydrophilic biomolecules to enter the inner domains of the polymer. Also, if the gold nanoparticles are embedded deep into the polymer, the biomolecules may be too far from the sensing volume of the particle. In addition, if the interaction between the particles and the polymer chains is too strong and the nanoparticles are entangled in the polymer network, their mobility may be severely restricted. Since the biosensing properties are determined by the spatial distribution of Au nanoparticles, it is important to be able to control this distribution. In order to concentrate the majority of the nanoparticles on the surface of the sample and make them accessible to the surrounding environment, we have explored some promising ways to increase the mobility of Au nanoparticles. Among them, the thermal post-synthesis treatment of Au-PDMS nanocomposite has been proved to be an adequate method to improve the distribution of Au nanoparticles in polymers without compromising on mechanical strength of the platform [63].

Recently, microwave (MW) heating has been explored as a promising technique for nanoparticle synthesis [91-95]. Microwaves are electromagnetic radiations with frequencies ranging between 0.3–300 GHz. Due to the low frequency of the irradiation, the dipoles have time to respond to the alternating electric field and, therefore, will rotate which will increase the collisions between the particles giving rise to dielectric heating [96]. Due to the internal and volumetric heating, the thermal gradients during microwave

processing are avoided, providing a uniform environment for the reaction. Since microwave irradiation is a volumetric phenomenon, the heat is generated in the irradiated volume with a homogenous distribution. Microwave-assisted synthesis method has been successfully applied for the preparation of a variety of nanosized inorganic materials. Unfortunately, the exact nature of the interaction of the microwaves with the reactants during the synthesis of materials is somewhat unclear and speculative [95]. The microwave synthesis, which is generally quite fast, simple, and energy efficient, has been developed, and used for Au, Ag, Mg, Ni, ceramic materials, etc. [73,91,97,98]. Compared with conventional methods, microwave synthesis has the advantages of very short reaction time, small particle size, narrow particle size distribution, high surface area and high purity of the materials. Microwave heating generates immediately nucleation sites in the solution, which considerably increases the rate of reactions and the kinetics is much improved [95].

Microwave irradiation has been used for the preparation of gold and silver nanoparticles under various conditions [73,91,93,94,97,99] but the microwave-assisted *in-situ* synthesis in a polymer matrix has not been yet explored. All the works cited above, used the microwaves for heating and the synthesis were carried out in solution [93]. In this chapter, we report a method of synthesis of Au-PDMS nanocomposite in the solid state. The method makes use of the properties of microwaves to increase the rate of reaction that takes place at the solution-solid interface. The Au-PDMS nanocomposite is prepared by a microwave-assisted method and the morphology of the material is optimized for biosensing applications. The mechanism of the formation of Au nanoparticles on the PDMS surface is discussed as well.

The sensitivity of the nanocomposite platform was determined and the biosensing capability has been tested by using an immunosensing protocol for the detection of bovine growth hormone.

## **3.2 Material and methods**

### ***3.2.1 Materials***

Poly (dimethylsiloxane) (PDMS) is fabricated by using a Sylgard® 184 elastomer kit (Dow Corning Corporation). Gold chloride trihydrate ( $\text{HAuCl}_4 \cdot 3\text{H}_2\text{O}$ ) was purchased from Alfa Aesar and 1-pentanol, toluene, N, N-dimethylformamid, 2-propanol and ethyl alcohol, from Sigma-Aldrich. Nanothink® 18, TWEEN® 20, N-Hydroxysuccinimide (NHS), and N-(3-Dimethylaminopropyl)-N'-ethylcarbodiimide hydrochloride (EDC) were purchased from Sigma Aldrich. A monoclonal Bovine growth hormone antibody and bovine growth hormone (bST) antigen were purchased from Dr. Parlow National Hormone and Peptide Program in California, USA.

### ***3.2.2 Fabrication of PDMS***

For the fabrication of PDMS, the base polymer and the curing agent are mixed (ratio 10:1 by weight). The fabrication is followed by removing the air bubbles from the mixture, under vacuum, in a desiccator for 10 minutes. To have a smooth PDMS surface, a silanized silicon wafer is used for molding. The mixture is then poured in the flat mold and, after a second degasifying process (10 minutes), the mold is kept in oven at 60°C for

at least 5h for curing. Afterward, the cured PDMS is peeled off from the mold and cut in 1 cm×4 cm samples. The thickness of the PDMS samples is around 1 mm.

### ***3.2.3 In-situ synthesis of Au-PDMS nanocomposite***

Solutions of chloroauric acid ( $\text{HAuCl}_4 \cdot 3\text{H}_2\text{O}$ ) in ethanol are prepared with concentrations ranging from 0.1% to 5%. To fabricate the nanocomposite, 60  $\mu\text{L}$  of the ethanol solution of the chloroauric acid was dropped on the PDMS sample. Then the solution is spread over the whole surface of the sample, after keeping it for at least 10 minutes in contact with the PDMS. The samples are then introduced into a microwave oven (GE model 1140, 1100W) and irradiated for different times. Figure 3-1, shows the procedure and some of the samples prepared with different irradiation times of 30, 60, and 90 sec. To study the gold nanoparticle (AuNP) size distribution on the PDMS surface, UV/Vis spectroscopy and Scanning Electron Microscopy (SEM) imaging are employed.

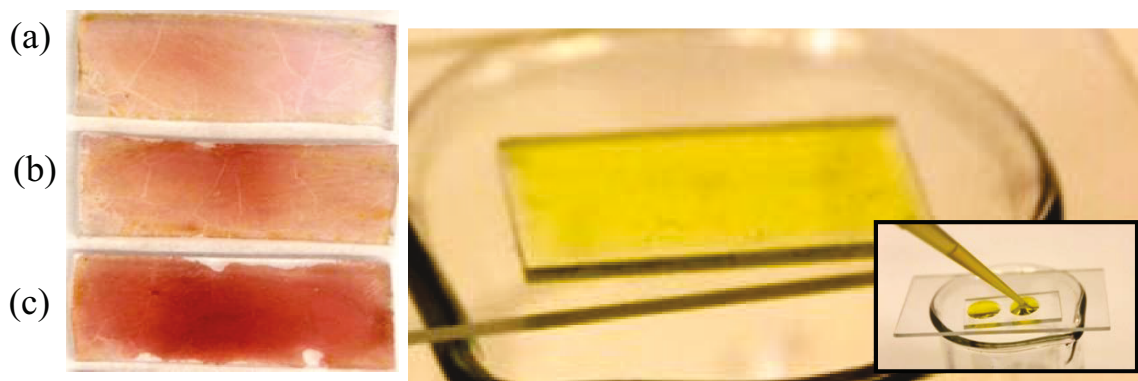


Figure 3-1: Procedure for the preparation. The ethanol solution (60 $\mu\text{L}$ ) of the gold salt (1%) is dropped on the PDMS surface (as shown in inset). The figure shows the solution expanded on the sample's surface, before irradiation. The samples are irradiated for different times varying from (a) 30s; (b) 60s; and (c) 90s.

### ***3.2.4 Annealing process***

A post-synthesis heat treatment (annealing process) was used to optimize the properties of the Au-PDMS surface film for biosensing applications. Heat treatment has been applied to increase the concentration of Au nanoparticles on the surface of the sample as well as to improve the distribution of the particles formed into the polymer network. To achieve this, the samples prepared using the *in-situ* method described above, have been heated gradually, from room temperature to 300°C-350°C and then kept at the maximum temperature for 30 minutes.

### ***3.2.5 Tension test***

To investigate the effect of presence of AuNPs on mechanical properties, specifically, on the module of elasticity of PDMS nanocomposite, the tension test was used [100]. The Au-PDMS nanocomposite will be further used for a structural application and, therefore, a high degree of strength (elasticity) is required. The tension test has been done using a BOSE ElectroForce® 3200 test instrument. The tension tests were performed for both the as-prepared and the annealed samples and the results are given in section 3.2. The stress-strain graph for each sample was obtained and the slope of the graph corresponding to the module of elasticity was calculated.

### ***3.2.6 Sensitivity Test***

In general, the Au band corresponding to the localized surface plasmon resonance (LSPR), has been found to shift to longer wavelengths (red shift) as the refractive index

( $n$ ) of the surrounding medium is increased [60,101]. The sensitivity of the Au-nanocomposite platform toward environments with different refractive indices has been performed. To do this, five solvents with different refractive indices have been used. The sensitivity has been calculated from the variation of  $\Delta\lambda_{\max}$  against  $\Delta n$ , where  $\Delta\lambda_{\max}$  is the gold LSPR band shift in a solvent (in nm) compared with the LSPR band position measured in deionized water, and  $\Delta n$  is the refractive index difference between the solvent and DI-water and is equal to  $\Delta n = n_{\text{solvent}} - n_{\text{water}} = n_{\text{solvent}} - 1.33$ .

### ***3.2.7 Biosensing protocol***

Label-free biosensing tests have been performed by using the annealed samples. The bST antibody (anti-bovine growth hormone) (anti-BGH) obtained in mouse and the corresponding antigen (bST) (bovine growth hormone) (BGH), were used for this test.

The protocol used for biosensing is described here. The first step consists in functionalizing the gold nanoparticles with 11-mercaptopundecanoic acid solution (NanoThink® ACID11) in ethanol (5mM), by immersing the sample in the solution for 5 hours. After attaching the linker, the conventional carbodiimide coupling chemistry (EDC/NHS) is used to activate the carboxyl groups, before attaching the antibody. The activation is carried out by keeping the sample in a 1:1 ratio (vol) mixture of N-(3-dimethylaminopropyl)-N'-ethylcarbodiimide hydrochloride (EDC, 0.4M) and N-hydroxysuccinimide (NHS, 0.1M) for 1 hour. The next step consists of attaching the antibody that is diluted in a PBS buffer solution (200ng/ml) to the functionalized Au NPs, followed by washing the sample several times with a 0.01% TWEEN®20 solution in PBS. The next step is attaching the antigen (80ng/ml) (bST in PBS) by immersion of the

sample in the corresponding solution. The samples were washed with PBS afterward. After each step the samples were dried and the spectra of the samples were recorded. Upon attaching biomolecules to the GPN, the Au-LSPR band shifts to longer wavelengths (red shift) [102-104] as discussed in detail in section 3.4.

### **3.3 Results and Discussion**

#### ***3.3.1 Microwave-induced reduction of gold ions***

As mentioned in Section 3.2.3, the first step in the fabrication of the nanocomposite is spreading the gold solution on the surface of PDMS, before irradiation. However, because of the strong hydrophobicity of the PDMS's surface, the solution can be spread only after minimum 10 minutes of contact between the solution and the sample surface.

In order to study the interaction between the solution and the surface, samples were prepared by keeping the solution on the surface for times varying from 5 minutes to 15 minutes. Afterward, the samples were washed thoroughly and their spectra were recorded (Figure 3-2-a). The spectra show the existence of the Au plasmon band even before MW irradiation as an evidence of formation of gold seeds on the surface. The formation of gold seeds on the surface is accompanied by the reaction of the gold salt in the solution with the cross-linking agent present in PDMS due to its reducing properties as illustrated schematically in Figure 3-2-b. However, the samples are colorless, and the SEM images of the sample do not show the presence of nanoparticles, probably because the particles are in the range of sub-nanometers, that is, smaller than the resolution of the SEM

instrument. It was suggested that the reduction reaction takes place between the gold precursor and curing (cross-linking) agent of the polymer [74].

From these results, it can be inferred that, the formation of the sub-nanometer sized gold seeds on the PDMS surface, alters the surface properties and allows the spreading of the solution on it. In addition, the seeds, most probably, initiate the formation of larger AuNPs on the surface, during the microwave irradiation.

The next step in the preparation procedure is the irradiation of the samples in a microwave oven. The experiments indicated that, by keeping the irradiated samples in the atmosphere, the color of the samples is changing with time. Indeed, immediately after irradiation, the samples appear gray-yellowish but, after keeping them at room temperature for an hour, the color turns to red. Figure 3-2-c (1-2-3) illustrate the change of color for a sample irradiated for 90 seconds and their corresponding spectra Figure 3-2-c (left) show that the position of the Au LSPR band shifts to shorter wavelengths (blue shift) along with the color change. After leaving the sample for 75 minutes at room temperature, the Au band shifts from 551 nm to 533 nm and the color is stabilized afterward.

To accelerate AuNPs formation, instead of keeping the samples for 75 minutes in the atmosphere (room temperature), they can be immersed in ethanol (99%), immediately after MW irradiation, and kept for at least 30sec. The spectra show that, in both cases, the resulting nanocomposites are identical.

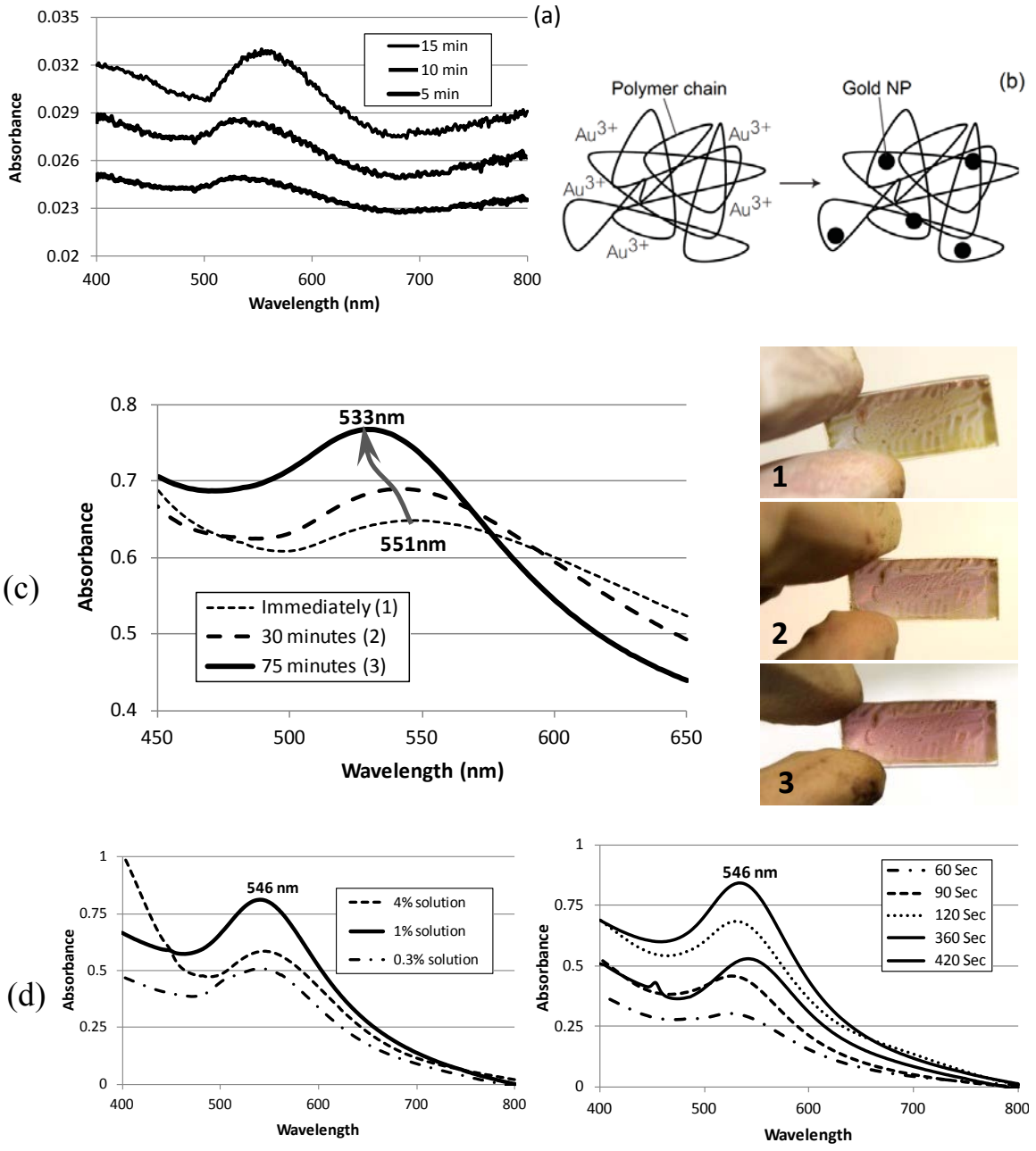


Figure 3-2: (a) Spectra of samples prepared by keeping the solution on the PDMS surface for varying times. The existence of the Au LSPR band proves the formation of gold seeds on the surface; (b) the schematic of formation of gold NPs in the polymer matrix; (c) keeping the sample on room temperature after irradiation change the color of the sample: (1) immediately after MW irradiation; (2) 30min after irradiation; (3) 75min after irradiation. (d) Effect of the irradiation time (concentration of gold precursor is 1%) (left) and of the concentration of the gold salt in solution (irradiation time of 360 sec) (right) on the spectra of the samples.

A possible explanation of the above observation is the following. The microwave irradiation may have two different effects. The first may be a change in the surface properties, by inducing the formation of polar groups on the surface. It is possible also that microwaves bring about a change in the distribution of the curing agent in the polymer, which results in a large amount on the surface. This later effect determines the formation of a high density of gold aggregates on the surface (gray-yellowish color) as shown in Figure 3-2-c (1). Upon immersing the sample in ethanol, a part of the aggregates are carried by ethanol into the polymer network and, consequently, the color turned to red, because more individual AuNPs will remain on the surface as shown in Figure 3-2-c (3). If the grey-yellowish sample is kept in the atmosphere, the same process will happen but at a much slower rate for 75 minutes.

The morphology of the nanoparticles prepared through the reduction of gold ions on the surface of PDMS depends on both the irradiation time and the concentration of the precursor solution. Spectra of Figure 3-2-d show the effects of irradiation time and that of the concentration. From the spectra, it can be inferred that a 1% solution of gold salt, irradiated for 360 second, results in a sample with an Au LSPR band that corresponds to a relatively broad size distribution.

The SEM results (not given here) show that, for an irradiation time less than 15 sec, no particles can be seen on the surface. By increasing the irradiation time, for example to 50 seconds, small nanoparticles begin to grow on the surface and their sizes are in the range of  $10\pm 2\text{nm}$ . For 90 seconds irradiation, the particle size reaches  $25\pm 5\text{nm}$ . Further increasing the irradiation time, results in the formation of linear aggregates.

It should be noted that, in all cases, the spectra display a broad band due to the wide size distribution of gold nanoparticles in the polymer matrix and to a pronounced particle aggregation. In addition, the background absorbance of the samples is relatively high. To improve the distribution of the gold nanoparticles embedded in the surface of PDMS, a heat treatment has been employed.

Samples prepared with different times of irradiation by using the 1% solution of gold salt have been prepared and then annealed and their corresponding Au-LSPR bands are obtained. The spectra indicate that, in order to prepare a nanocomposite with a narrow size distribution of gold nanoparticles, a 1% solution of gold precursor has to be spread on the PDMS surface and be irradiated for 90 seconds.

It should be noted that in all cases, the samples, either are kept for least 75 minutes at room temperature or are immersed in ethanol, before annealing, to stabilize the color of the samples as mentioned earlier.

SEM images have been used to show the distribution of gold nanoparticles embedded into the PDMS surface. The images, before and after the annealing post-process, are given in Figure 3-3-a and Figure 3-3-b respectively. The figures show that, after annealing at high temperatures, the aggregated particles are transformed into individual particles, uniformly distributed into the surface. The inset in Figure 3-3-b shows low-magnification of the annealed sample and illustrates a uniform distribution of particles on a large ( $2\mu\text{m}\times 2\mu\text{m}$ ) area of the sample.

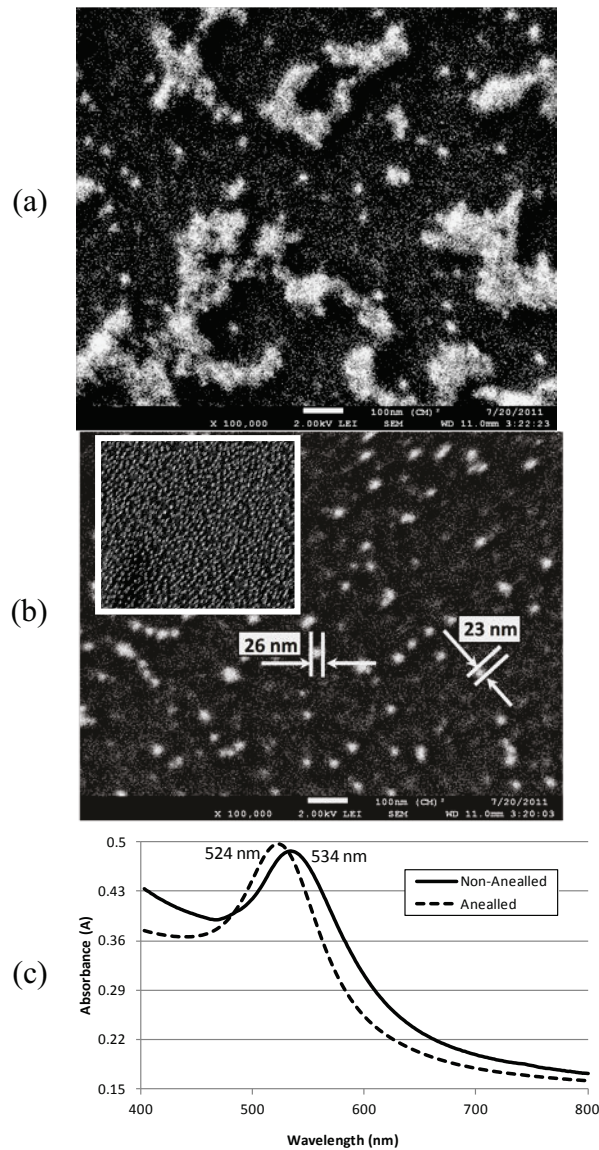


Figure 3-3: SEM images of Au-PDMS nanocomposite, (a) as-prepared sample; (b) annealed sample at 300-350°C. The inset shows the distribution of particles on a large  $2\ \mu\text{m} \times 2\ \mu\text{m}$  area of the sample. (c) Effect of the annealing process on the position of the Au-LSPR band.

The spectra corresponding to the as-prepared and annealed samples are given in Figure 3-3-c and show that, after annealing, the Au plasmon band shifts to shorter wavelengths (blue shift). This blue shift reflects the improved morphology during the annealing process, in terms of uniformity of the nanoparticles distribution as shown in the SEM images in Figure 3-3-a and Figure 3-3-b.

### 3.3.2 Mechanical properties

As it has been mentioned, the cross-linking (curing) agent has the role of a reducing agent during the *in-situ* synthesis. In contrast, increasing the amount of curing agent reduces the modulus of elasticity ( $E$ ) of the PDMS platform. To investigate the effect of the amount of the curing agent on the elasticity of PDMS, tension tests have been performed on samples prepared with two different ratios of polymer to curing agent. The ratios of 10:1 and 4:1 are selected and the tension test results are shown in Table 3-1. The results show that, by using a higher ratio, samples with a higher elasticity are obtained. For each case, four similar samples were tested and the average values are shown in the table.

Table 3-1: Module of elasticity ( $E$ ) for PDMS with two different ratios (MPa) and the effect of presence of AuNPs on the module of elasticity of PDMS

Sample Type	Non-Annealed (as prepared) sample	Annealed (post processed) sample
PDMS (4:1 ratio)	0.74±0.08 MPa	0.77±0.06 MPa
PDMS (10:1 ratio)	1.27±0.04 MPa	1.31±0.07 MPa
Au-PDMS nanocomposite (10:1)	1.47 ±0.1 MPa	1.52 ±0.1 MPa

The tension test is also used to show how the presence of gold nanoparticles affects the mechanical behavior of the nanocomposite. Samples (fabricated as described in section 2.2) were irradiated for 90 sec by using the 1% solution of the gold salt. Four identical samples were tested for both the as-prepared and annealed nanocomposites in each case

and the average results are given in Table 3-1. The results show that the introduction of gold nanoparticles in the polymer increases the module of elasticity up to 20%. In addition, the high elasticity of the annealed sample indicates the existence of some of the gold nanoparticles inside of the polymer network, even after the annealing process.

### ***3.3.3 Sensitivity of the platform and biosensing***

#### **3.3.3.1 Sensitivity of the nanocomposite platform**

In order to demonstrate the sensitivity of the platform, measurements were conducted in media of different refractive indices (RI). By increasing the refractive index of the surrounding medium, the Au-band is shifted to longer wavelengths (red shift) as shown in Figure 3-4. The sensitivity test is a good method to assess the biosensing capability of a sensing platform. A higher sensitivity shows that the platform is more sensitive to the surrounding environment. The sensitivity graph for the as-prepared and annealed samples is depicted in Figure 3-4.

The results show that the annealed sample has a sensitivity as high as 102 nm/RIU which makes it very useful for label-free biosensing of polypeptides and proteins. The sensitivity is lower for the non-annealed samples with about 61nm/RIU. This result could be due to the presence of high aggregates on the surface.

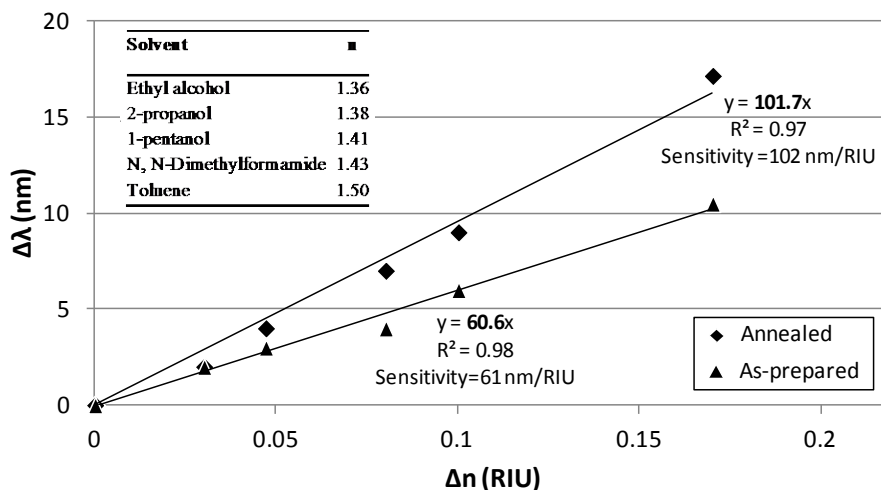


Figure 3-4: Sensitivity of nanocomposite sensing platforms (the nanocomposite is prepared by using a 1% gold precursor solution with an irradiation time of 90sec) for both as-prepared and annealed samples. The regression coefficient (R) is given for each graph.

### 3.3.3.2 Biosensing of the growth hormone

Somatotropin (ST) is a polypeptidic growth hormone naturally produced by the anterior pituitary gland in mammals. Its biological effects of bovine ST are associated with growth, development, and reproductive functions. Previously various methods have been reported for estimation of bST concentration in biological media such as ELISA, a radioimmunoassay (RIA), fluorescent LoC method [104].

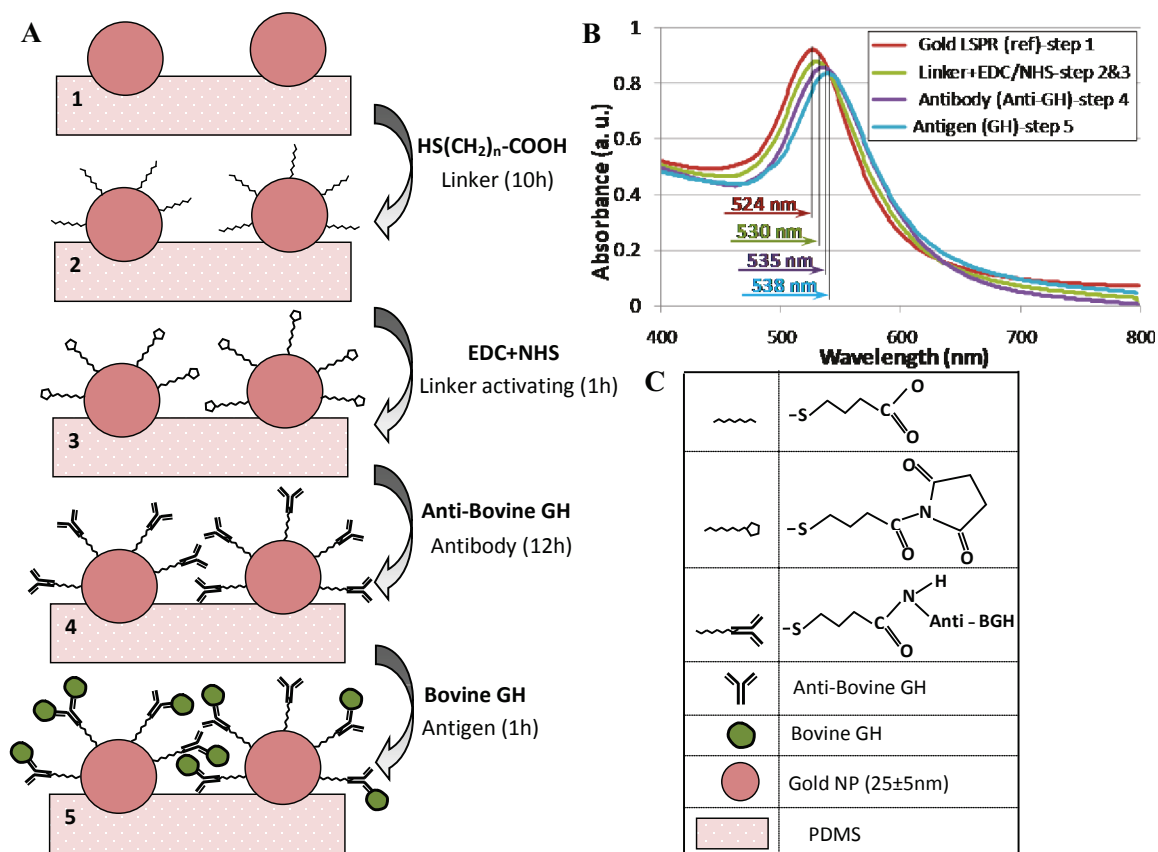


Figure 3-5: Schematic of the main steps of the biosensing experiment and their corresponding spectra; (A) Four steps of biosensing protocol; (B) Au-LSPR band corresponding to the steps depicted in A; (C) legend of the schematics.

Recently, a novel LSPR biosensing method for screening of recombinant bST (rbST) in milk has been reported by our group [105]. In this work, because of our experience in the field, we investigated this novel Au-PDMS nanocomposite platform for the detection of the polypeptide hormone.

The samples prepared and annealed as described in section 2 were tested for biosensing application. The biosensing experiment consists of immobilization of antibody on gold nanoparticles embedded on PDMS and detection of the antigen/antibody (bovine growth hormone in mouse) interaction using the Au plasmon band. The experiment consists of four main steps which are schematically depicted in Figure 3-5-a. The spectra

corresponding to the different steps of the biosensing experiment are shown in Figure 3-5-b.

The results showed a good sensitivity of the sensing platform in detecting the antibody-antigen interaction. In this case, the Au LSPR band red shifted by  $\Delta\lambda = 6$  nm after adding the linker and ECD+NHS (activation solution),  $\Delta\lambda = 5$  nm after attaching the Ab (anti-BGH) and  $\Delta\lambda = 3$  nm with attaching the complimentary antigen (BGH) corresponding to the Ab. The shift to longer wavelength in each case is due to the increased refractive index of the environment. During the last step (addition of the Ag) the shift is mainly due to the Ab-Ag interaction.

One of the issues that can influence negatively the biosensing experiments is the possibility of leaching of nanoparticles from the polymer network. In the specific case of Au-PDMS nanocomposite, because of the strong interaction of particles with polymer chains (Figure 3-2-b), there is very low chance of leaching [106]. In addition, taking into account the large size of AuNPs (~25nm) even in the case of a weak leaching, there would not be toxicological effects [107]. Indeed, a test for leaching was performed by keeping the sample for a long time (minimum 5 days) in water or ethanol and the spectral results were negative.

### **3.4 Conclusion**

In this work, a novel microwave assisted *in-situ* preparation of gold-poly(dimethylsiloxane) (Au-PDMS) nanocomposite is proposed and optimized for biosensing application. Ethanol was used due to its high permeability in the PDMS polymer network which accelerates the rate of the reduction of gold. In addition, microwave-assisted

synthesis has the advantages of very short reaction time, small particle size and narrow size distribution of the synthesized particles.

It is found that during the interaction between the PDMS surface and the precursor solution (before irradiation), sub-nanometric sized gold seeds were formed on the surface which initiate the growth of gold nanoparticles during the irradiation step. Microwave assisted synthesis resulted in uniformly distributed AuNPs in the polymer matrix. An annealing process at high temperature is employed to improve the particles size distribution. The SEM and UV/Vis spectra of the annealed samples show a uniform distribution of particles on the large area of the sample.

Sensitivity tests are performed to show how the Au-band is shifted (red shift) by increasing the refractive index of the surrounding medium. The sensitivity test showed a high sensitivity of 102nm/RIU in the case of the annealed sample. This illustrates that the optimized platform exhibits very good biosensing capabilities. The platform is used further for plasmonic antigen-antibody interaction detection of growth hormone. The immunosensing of the bST proves that the fabricated platform is a good candidate for biosensing. The results obtained in this work are relevant for microfluidic biosensing.

In addition, the mechanical tension test revealed that the presence of AuNPs improves the mechanical properties of the polymer at least 20%. Since the Au-PDMS nanocomposite will be further used for structural application, a high degree of strength is required.

## **Chapter 4: High performance PDMS micromixer based on split and recombination flows for lab-on-a-chip applications**

Beside *in-situ* methods which explained in the previous two chapters, another method to immobilize AuNPs into the PDMS is to introduce the pre-made nanoparticles to a surface. The particle will be adsorbed by the affinity of the particle toward the surface. To make the particles in a microfluidic environment, first we have to fabricate a micromixer, to enhance the reaction in a microreactor. In this chapter a cost-effective and simple 3-layer PDMS passive micromixer has been designed, optimized, simulated, fabricated and successfully characterized. The mixing mechanism is based on splitting and recombining the flow.

### **4.1 Introduction**

While the microfluidic technology has been maturing well, a big surprise is that LoC systems are still not being used extensively. Through the fabrication of microfluidic devices which possess two fundamental and demanding features including “*low-cost*” and “*simple*”, it is very likely to move toward the next step of using LoCs for wide applications [62].

One of the most challenging tasks in the LoC systems is efficient mixing. In biochemical analysis systems which work under a microfluidic environment, achieving better mixing

in a short period of time as well as a short fluidic system is crucial in order to improve the reaction. Due to low Reynolds number in microfluidic systems (flows with  $Re \sim 0.01-10$ ), the flow regime is laminar and consequently the mixing mechanism becomes mostly diffusion dominant [108-110].

Micromixers are generally classified into two main categories: passive and active. In passive micromixers, the mixing is performed by changing the geometry of the mixer in order to increase the possibility of having turbulence in the flow. In contrast, in active micro mixers, the mixing task is performed by an active element which produces disturbances externally through moving parts [110-113]. Compared to active mixing mechanisms, passive micromixers have simpler design and therefore can be well integrated for lab-on-a-chip (LoC) application [114,115].

Besides being low-cost and simple, another important issue that has to be considered in the design of micromixers is their working flow rate which strongly depends on their applications. Micromixers are mostly used in two main categories including chemical microreactors and immunoassay biosensors [116]. Microreactors are operate normally at relatively small flow rates [117]. In addition, in biosensing applications, the flow rate should be small enough to enhance biomolecule interactions in order to achieve an acceptable sensitivity[118]. Typical flow rates for these applications are 1-20 $\mu$ l/min or less [118-122] indicating that the mixing is determined mostly by diffusion.

In the last decade, various types of passive micromixers have been developed and fabricated including 2D structures such as tesla structure [115], sawtooth structure [123], and various T-type mixing mechanisms with obstacles [124] and fin arrangements [125]

inside the microchannels. Through these structures, researchers try to increase the possibility of creating disturbances for better performance [126]. However, their acceptable performance could only be achieved in high flow rates ( $\sim 100\mu\text{l}/\text{min}$  and more) which are too far from the applicable range mentioned earlier [108,115,124,127,128]. Furthermore, another drawback of these micromixers is the long length of the microchannels, which are in the order of a few centimeters [115].

To achieve better mixing performances in shorter lengths, several complex 3D structures have been proposed [129,130]. Examples include 3D structures for twisting flow [109] and *split-and-recombine* structures [127,129,131,132]. Nevertheless, they used very complicated 3D structures that use multiple fabrication steps which make them to be too far from being “*cheap*” and “*simple*” [129-133]. Using of polymeric materials for low-cost fabrication of micromixers is a good example of enabling wide applications of integrated LoC devices [128,131,134].

In the present chapter, we propose a 3D micromixer with high efficiency, based on split-and-recombination of the flow. We attempt to reach “*cheap*” and “*simple*” goals by introducing a simple 3-layer PDMS structure. The device is designed and optimized. The mixing is simulated and its performance is compared to that of a T-type mixer by developing a new mathematical-based method for the estimation of the mixing efficiency. The micromixer was fabricated and the flow is visualized in the chip. Finally, a mixing experiment was accomplished to evaluate its performance quantitatively in the real conditions. The results show a very good mixing performance at low flow rates (1-

20 $\mu$ l/min). Due to the simplicity of the proposed micromixer, the mixing unit can be easily integrated with micro-total analysis systems ( $\mu$ -TAS).

## 4.2 Design

### 4.2.1 Design Principle

The proposed passive micromixer is based on the split-and-recombination of flow to maximize the surface contact between two fluids of interest. The mixing mechanism of a T-type mixer and the proposed mixer is shown in Figure 4-1. In the Figure 4-1-a, a T-type mixer is depicted. The T-type streamlines show that there is only one contact area between the two fluids. In this figure, the concentration distribution along the microchannel is also shown. In the Figure 4-1-b, the concentration distribution along the microchannel is also shown.

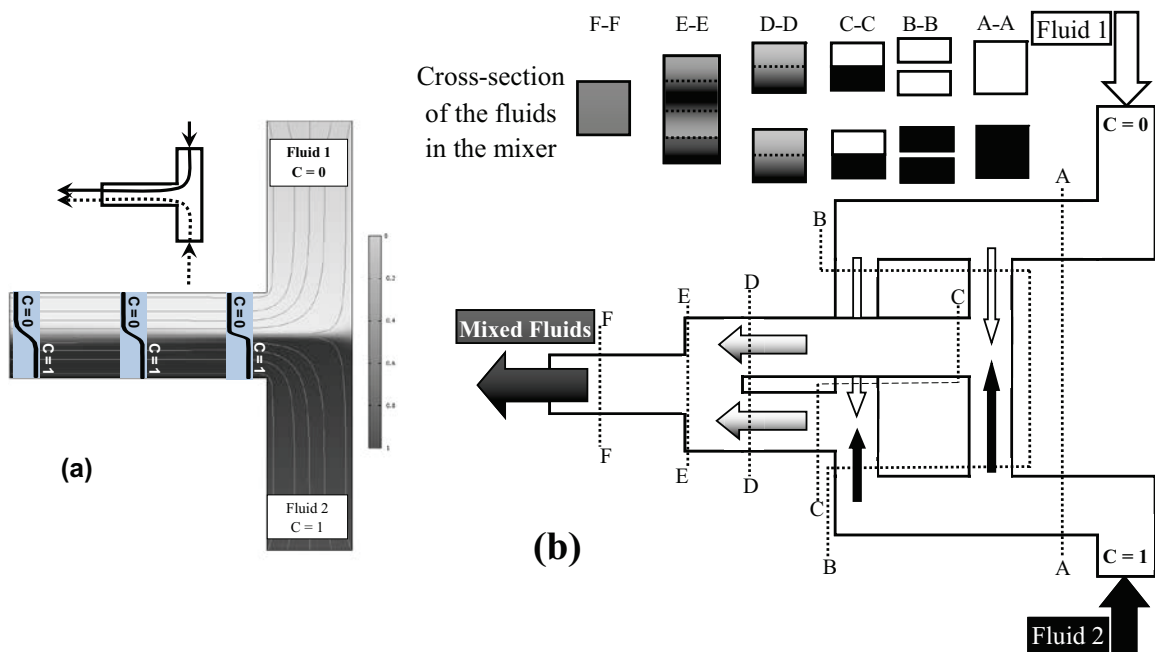


Figure 4-1: Mixing mechanism; (a) T-shape mixer; (b) the proposed 3-layer micromixer. Each inlet is split into two sub-streams. The streams are finally recombined at the outlet.

As shown in Figure 4-1-b, the proposed device has a microchannel configuration that can guide the fluids to produce alternate layers at the outlet in order to maximize the diffusion. The input fluids 1 and 2 were dispensed equally in a set of microchannels and then were re-arranged in a new layered configuration. In the design, there are two simple T-type sub-mixers which will be mixed at the final step to have a complete mixing. Through this design, each inlet is dispensed into two sub-streams and at the final stage they will be reunified in a way that maximizes the surface contact between the two flows of interest.

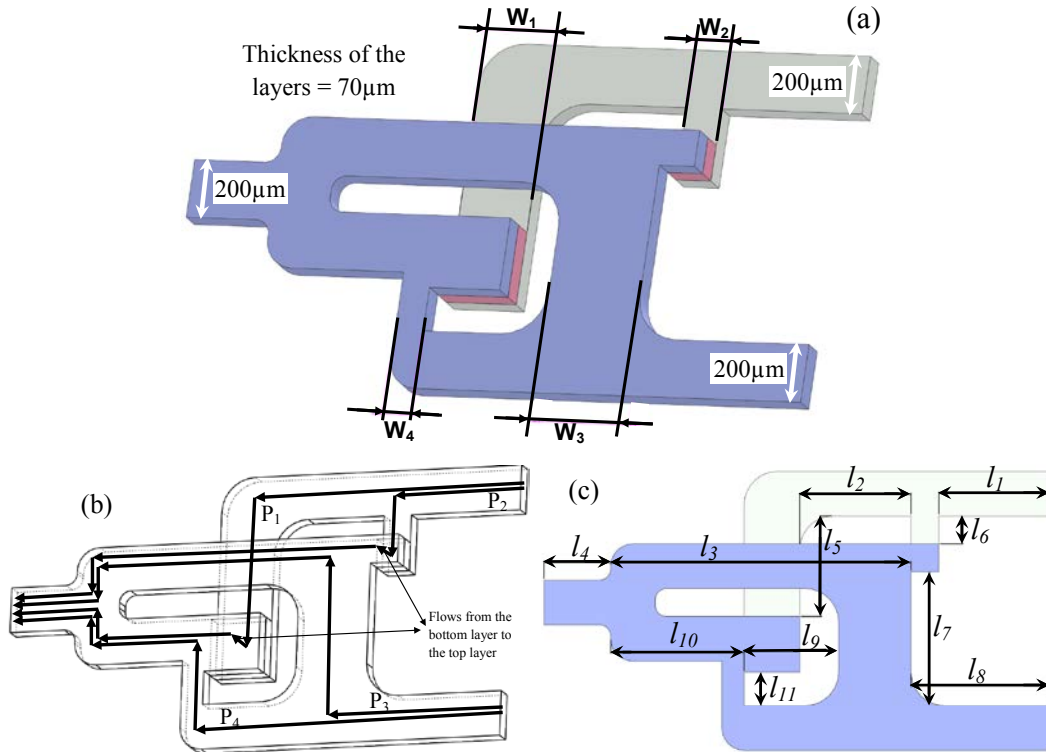


Figure 4-2: The 3D view of the micromixer. (a) The variables namely, the width of the channels ( $W_1$ – $W_4$ ) have to be optimized to have equal contributions from the inlets to maximize the mixing performance, (b) four available paths ( $p_1$  to  $p_4$ ) from inlets to the outlet, (c) micromixer dimensions used for optimization.

A 3-D view of the device is shown in Figure 4-2-a. From this figure, it can be seen that, the micromixer contains 3 layers. The fluid 1 in the first (bottom) layer will be dispensed into two sub-streams and will be carried through the second layer into the third (top) layer where mixing will happen with the fluid 2 which is already dispensed in this layer.

#### ***4.2.2 Optimization of the micromixer dimensions***

In order to maximize the mixing performance, we should adjust the channel widths  $W_i$  where  $i=1,2,3,4$ . The dimensions are schematically shown in Figure 4-2-a. The maximum performance for a specific inlet flow rate can be reached, when each microchannel with the width of  $W_i$  contributes equally to the outlet flow. To mathematically express how each part of the inlet (with the size of  $W_i$ ) applies a resistance to the flow from inlet to the outlet, equation of *head loss* in channel was used. Head loss ( $h$ ) in a pipe with the length of  $L$  can be obtained from the equation [135]:

$$h = f \frac{L V^2}{D} \quad (4 - 1)$$

Where  $D$  is the pipe hydraulic diameter and it is equal to  $D=4A/P$ , where  $A$  and  $P$  are area and perimeter of the channel, respectively,  $V$  is the fluid velocity and  $f$  is the friction factor that is determined experimentally. For low Reynolds number ( $Re$ ) flow or laminar flow regime which is applicable in microfluidic systems, there is a simple relation between friction factor  $f$  and  $Re$  that can be expressed as the following equation:[135]

$$f = \frac{64}{Re} \quad (4 - 2)$$

Where  $R_e$  is Reynolds number and  $R_e = \rho VD / \mu$  where  $\rho$  is the fluid density and  $\mu$  is the dynamic viscosity of the fluid. In addition to the head loss in the pipe, there are also minor head losses ( $h_m$ ) in bends, Tees (both combining and dividing), etc., which can be calculated from the equation  $h_m = KV^2/2$  where  $K$  is the friction coefficient that is determined experimentally and is tabled in the fluidic handbooks.[135]

Considering the thickness of  $h$  for the microchannels, when the flow with the rate of  $Q$  is flowing in a channel with the width of  $W$  and length of  $L$ , the following equation can be used to calculate the head loss:

$$h = \frac{8\mu QL}{\rho} \frac{(h + w)^2}{h^3 w^3} \quad (4 - 3)$$

There are two possible flow paths from each inlet to the outlet. Hence, we have the total of four possible paths from the inlets to the outlet that is shown in Figure 4-2-b by  $P_i$  where  $i=1$  to 4. The value of head loss in each path is assumed to be  $h_i$  where  $i = 1, 2, 3, 4$ . Head loss in each path is a function of the variables ( $W_i$ ) and the length of the channels ( $l_j$  where  $j=1$  to  $11$ ) as shown in Figure 4-2-c. In addition, in each pass, there are bends, Tees or change in the channel dimensions, which produce minor head losses ( $h_{mi}$ ) and should be considered in the calculation of total head loss in each pass. So the head losses,  $h_i$ , in paths  $P_i$  are as follows:

$$\begin{aligned} h_1 &= f_1(w_1, w_2, w_3, w_4, l_j) + h_{m_1} \\ h_2 &= f_2(w_1, w_2, w_3, w_4, l_j) + h_{m_2} \\ h_3 &= f_3(w_1, w_2, w_3, w_4, l_j) + h_{m_3} \\ h_4 &= f_4(w_1, w_2, w_3, w_4, l_j) + h_{m_4} \end{aligned} \quad (4 - 4)$$

In this design, the length  $l_j$  are selected as constant and therefore the head losses are only dependent of variables  $W_i$ . In order to have equal flow rates through these paths, these head losses should be equal or the following conditions are applies for the optimization of widths:

$$\begin{cases} h_1 = h_2 \\ h_1 = h_3 \\ h_1 = h_4 \end{cases} \rightarrow \begin{cases} f_1 - f_2 = 0 \\ f_1 - f_3 = 0 \\ f_1 - f_4 = 0 \end{cases} \quad (4 - 5)$$

As we can see, there are four unknowns and three equations. To be able to solve this set of nonlinear and coupled equations, a constraint is created by setting  $W_4=75\mu m$  and the other three widths ( $W_1$ ,  $W_2$ , and  $W_3$ ) are determined. The optimum widths are obtained as the following:  $W_1=200\mu m$ ,  $W_2=100\mu m$ ,  $W_3=260\mu m$  and  $W_4=75\mu m$ .

### 4.3 Simulation model

The simulation of the mixer with optimized dimensions is performed to evaluate the mixing performance under different inlet flow rates. The COMSOL® Multiphysics MEMS module is used for the finite element (FE) analysis of the Navier-Stokes incompressible fluid flow in microfluidic environment. The water is used as the fluids to be mixed containing solutes with two different concentrations of  $C=0$  and  $C=1$  in order to have normalized concentration at the outlet. The diffusion coefficient of the solute in water was set to  $2.5 \times 10^{-10} \text{ m}^2/\text{s}$ . FEM of the 3D CAD model is used for simulation. The whole 3D volume is discretized with the maximum element size of  $4.5\mu m$ . The convergence limit for the normalized relative error was set  $1 \times 10^{-7}$ .

### 4.3.1 Simulation performance assessment

The following method was established in order to assess the simulation results. For each case, the profile of concentration in the outlet is obtained along a line at the middle of its depth. In the Figure 4-3-a and Figure 4-3-b typical concentration variation for a T-type and for the new mixer is shown by a black line. In this figure, the red lines correspond to the worst case where there is no diffusion between two fluids of interest. The green line depicts the case where the fluids were mixed fully.

The hatched area represents the amount of diffusion of one fluid into the other. Mixing efficiency,  $\eta$ , is defined as the ratio between the hatched area that represent mixing and the area between the green and red line that corresponds to full mixing using the following equation:

$$\eta \% = \frac{\text{area corresponds to mixing}}{\text{area corresponding to fullt mixing}} \times 100 = \frac{\int_0^1 (\text{hatched width}) dx}{0.5 \times \int_0^1 dx} \times 100 \quad (4-6)$$

The area corresponding to fully mixing (showed in gray in Figure 4-3) between the green and red line is obtained as 0.5 as the final concentration is equal to 0.5 and the width of the channel is normalized. This measurement of  $\eta$  will be used for performance characterization.

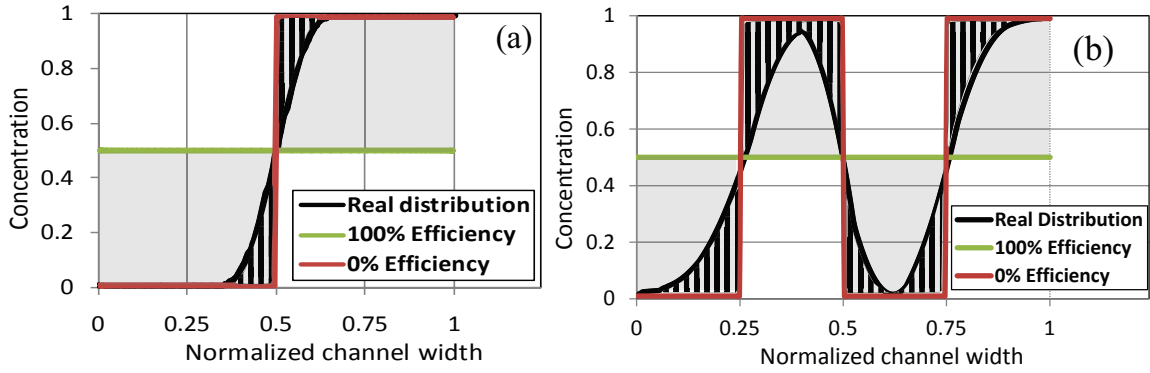


Figure 4-3: Performance assessment of mixing; (a) T-type micromixer, (b) proposed micromixer.

### 4.3.2 Simulation results

The simulation performed by using the mentioned parameter and the results for T-type and the proposed device are depicted in Figure 4-4-a and Figure 4-4-b respectively. In order to compare the efficiency, the outlet profile is obtained for a point along the chip at the lengths of 3.8mm from the inlet that is shown as C-C cross-section in Figure 4-4 and in all graphs the mixing efficiency  $\eta$ , was obtained at this point. Even the actual channel length at the measuring section for the proposed mixer is longer than the conventional T-mixer due to 3D configuration, by the thickness of the middle layer, same chip distance is chosen to obtain minimum footprint. The simulation results for the high flow rate of  $20\mu\text{l}/\text{min}$  are shown in Figure 4-4. In this figure, in each type, the simulations are shown in the form of cross-section concentration distribution at three different cross-sections of the channel. In addition, variation of concentration at middle line is also shown for the proposed and T-type mixers.

Based on the performance criteria, the new mixer can achieve a mixing efficiency as high as 76% even at a high flow rate of  $20\mu\text{l}/\text{min}$  ( $R_e \sim 3$ ) while a T-type mixer shows only  $\eta=21\%$ . The mixing efficiency is shown in Figure 4-5 for various flow rates between

0.2 $\mu$ l/min and 50 $\mu$ l/min. Considering the mixing efficiencies of higher than 80% for fully mixed flows, the proposed mixer can achieve full mixing for the flow rates up to 15 $\mu$ l/min ( $R_e < 2.2$ ).

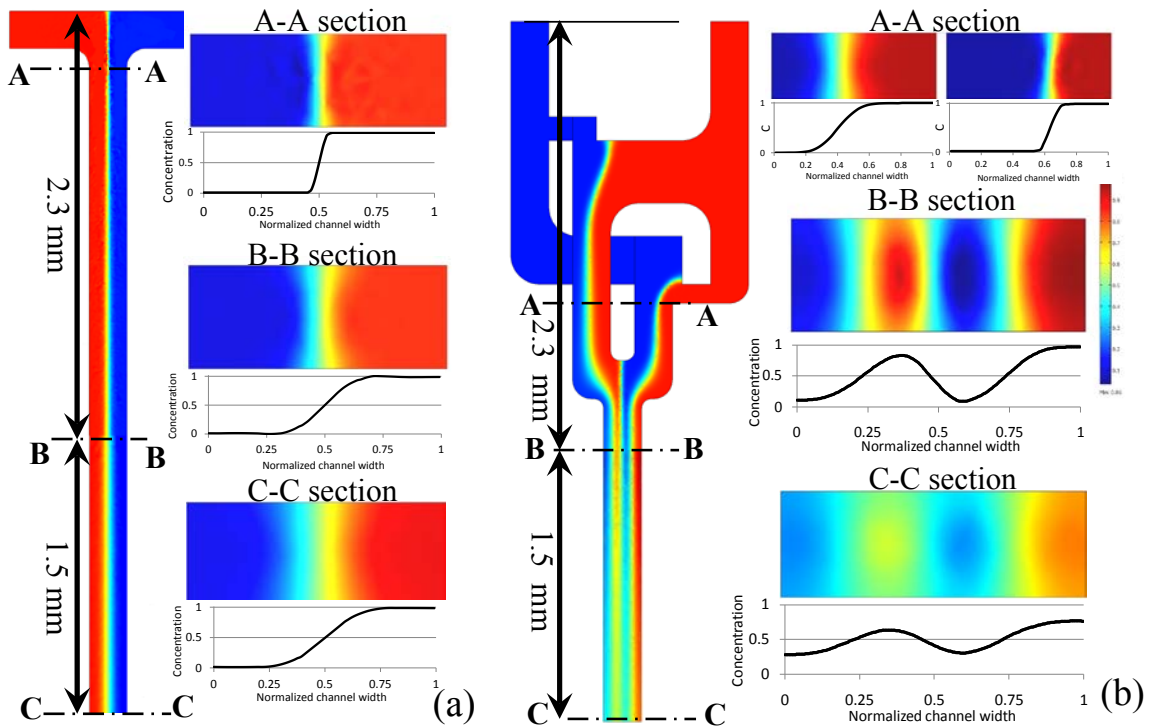


Figure 4-4: Simulation results at flow rate of 20 $\mu$ l/min; (a) T-type mixing with  $\eta=20.9\%$ , (b) the proposed micromixer ( $\eta=76.3\%$ ).

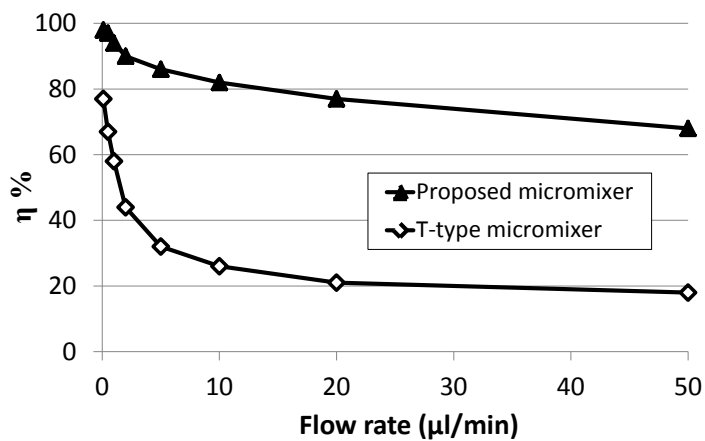


Figure 4-5: Comparison of mixing performance of the proposed micromixer and a T-type micromixer at different flow rates.

Figure 4-5 indicates very high efficiency for the low flow rates due to the enhanced diffusion-based mixing mechanism of the proposed mixer. However, there is a relatively low mixing performance for high Reynolds numbers ( $R_e > 4.0$ ) when the flow rate is higher than  $30 \mu\text{l}/\text{min}$ . There is a promising way to resolve this problem by combining several mixing units. Considering the proposed micromixer as a mixing unit, one can combine several units to build a mixing module.

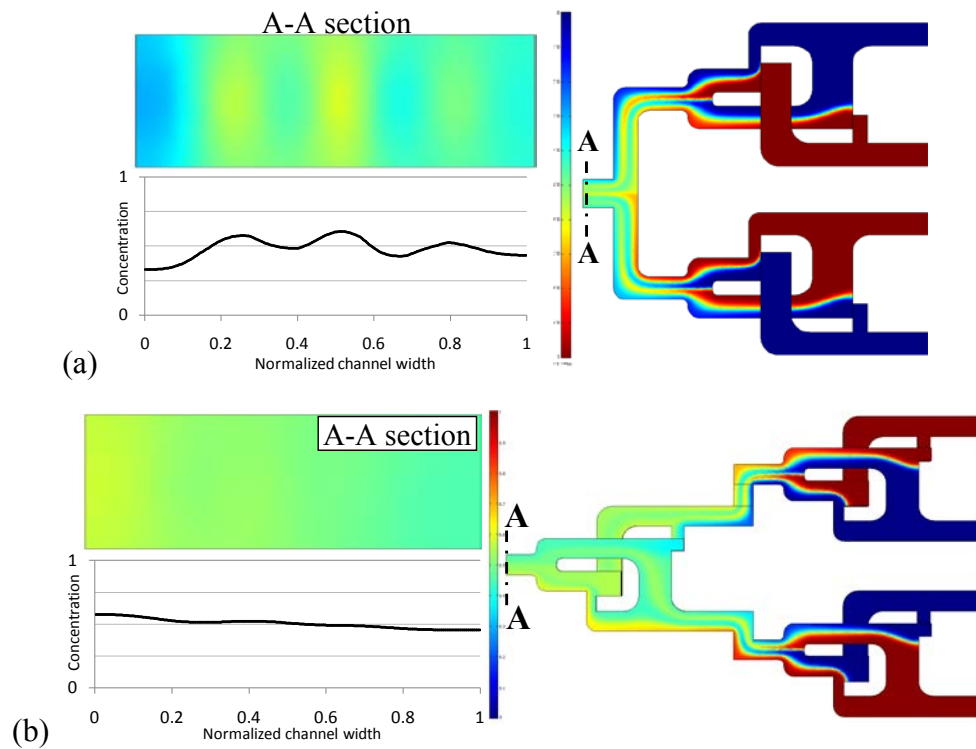


Figure 4-6: Simulation of combination of several mixing units for achieving better mixing performance at a high flow rate of  $50 \mu\text{l}/\text{min}$ ; (a) two units ( $\eta=82.5\%$ ) and (b) three units ( $\eta=91.6\%$ ).

The simulation results for mixing modules that are made up of two and three mixing units are shown in Figure 4-6. In each case, the concentration distribution at the outlet cross-section is shown. The results show that at a high flow rate of  $50 \mu\text{l}/\text{min}$ , the mixing efficiency of a mixing module that is built from two and three mixing units is 83% and

92% respectively. The mixing efficiency for various flow rates between 2 $\mu$ l/min to 100 $\mu$ l/min is shown in Figure 4-7. The results show that the combined micro mixers can reach fully mixing for high Reynolds number of  $Re < 13.5$  corresponding to the flow rate up to  $Q=100\mu$ l/min. One could conclude that the proposed mixer configuration enables very high mixing efficiency even at high flow rates.

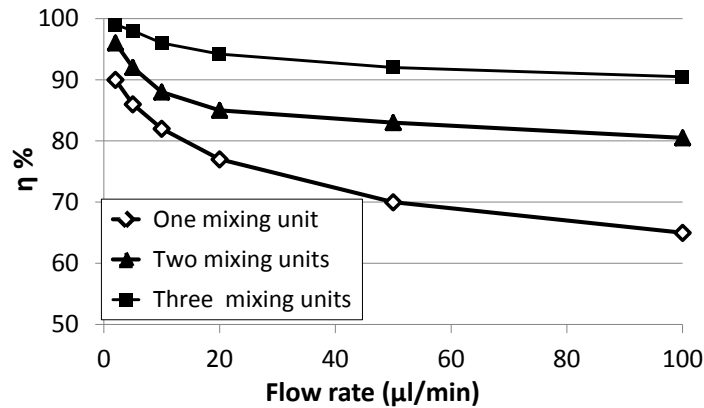


Figure 4-7: Mixing performance with different combination of mixer units at different flow rates.

#### 4.4 Fabrication

The proposed micromixer was fabricated using poly(dimethylsiloxane)(PDMS). Sylgard® 184 elastomer kit from Dow Corning Corporation was used for PDMS fabrication. For fabrication, the base polymer (pre-polymer) and the curing agent (cross-linking agent) are mixed with 10:1 ratio by weight. The device consists of three layers. Therefore, there are three individual masks for the fabrication of the mold for each layer.

The schematic of fabrication steps of the mixer is depicted in Figure 4-8-a. In this figure, three SU-8 molds and their corresponding PDMS layers includes lower (L), middle (M) and upper (U) layers are shown. Standard patterning of SU-8-2035 photoresist (from MicroChem) was used for the fabrication of the molds. For each layer, the SU-8 was spin

coated (at 500rpm for 10 sec followed by 1500rpm for 35s) and then soft baked at 95°C for 12 min. The soft backed SU-8 then was exposed to UV light followed by a post baking process for 10 min at 95°C. After that, the SU-8 was developed and finally the mold is hard baked at 150°C for 30 minutes. To be able to use these layers as a mold for PDMS fabrication, all molds are silanized.

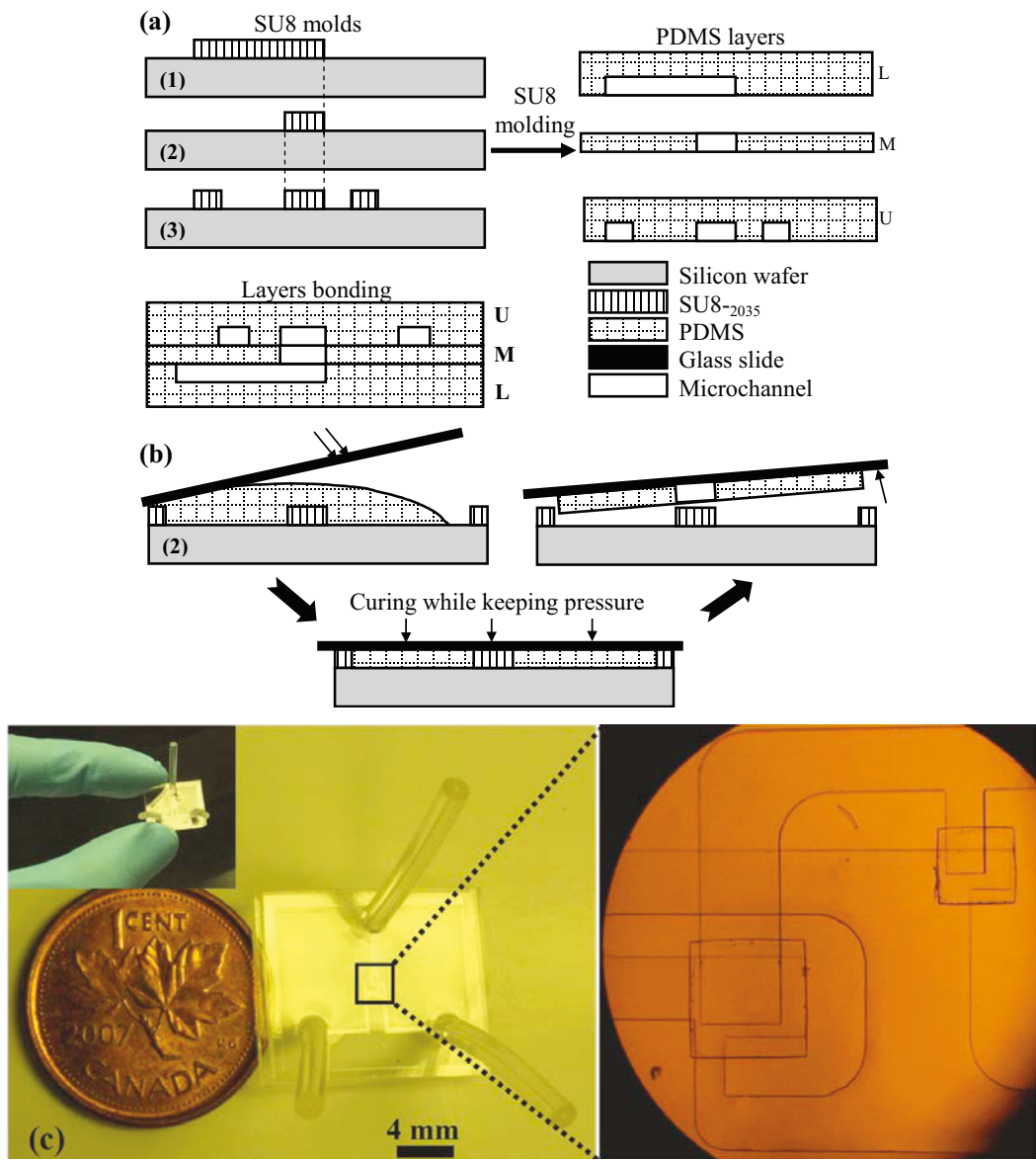


Figure 4-8: Fabrication process of the micromixer; (a) three SU-8 molds used for fabrication of the mixer (b) PDMS thin layer fabrication process to make the middle layer (80µm thick); (c) the fabricated device and the close-up shows how 3-layers are aligned to form the mixer.

As shown in Figure 4-8-a, the proposed PDMS device includes two thick layers (U and L) and a thin middle layer (M) with the thickness of  $80\mu\text{m}$ . The fabrication process of the thin layer is schematically shown in Figure 4-8-b. For the fabrication of the thin layer, PDMS was poured on the mold and then a semi-silanized glass slide was placed on PDMS to let the excess of PDMS to be removed from the mold. While keeping the pressure on the glass slide, the PDMS thin layer was cured at  $100^{\circ}\text{C}$  for an hour. Afterwards the semi-silanized glass slide with PDMS thin layer can be easily peeled off from the mold as the mold was already silanized. Oxygen plasma was used to bond the middle layer to the bottom thick PDMS layer. After this bonding, the glass layer is replaced by the top thick PDMS layer to seal the channels. The fabricated device is then used for real mixing experiments and flow visualization.

One of the important issues in the bonding process is the correct alignment of the layers. This is crucial as the middle thin layer allows the fluid to be passed through its hole from the first (bottom) layer to the third (top) layer. Therefore, any miss-alignment will result in malfunctioning of the device. To reduce the bonding errors, a clearance of  $15\mu\text{m}$  is considered in the size of features of middle layer. These size changes are also considered in the calculation of minor head losses for finding of optimum channel widths.

## **4.5 Experimental mixing results**

### ***4.5.1 Flow visualization***

In order to characterize the realized device and compare the simulation with the experimental results, red and green colored water was introduced to the inlets. A syringe

pump is used to pump two dies with different flow rates. A camera attached to a microscope recorded the visualized flow. The experimental results for the flow visualization show the efficient mixing of two dies. Figure 4-9 shows the flow of the two colored fluids in the microchannels and demonstrates how the sub-streams split into two flows and then combine into the outlet. In the Figure 4-9-a a high flow rate of 400  $\mu\text{l}/\text{min}$  was used ( $Re \sim 55$ ) to diminish diffusion and to show four equal sub-streams in the outlet. These equal sub-streams in the outlet prove that the optimization part was done successfully. In Figure 4-9-b the mixing is shown at flow rate of 40  $\mu\text{l}/\text{min}$ . From this figure it can be observed that the thickness of the green flow is diminishing along the flow which shows the flows are mixing efficiently by diffusion.

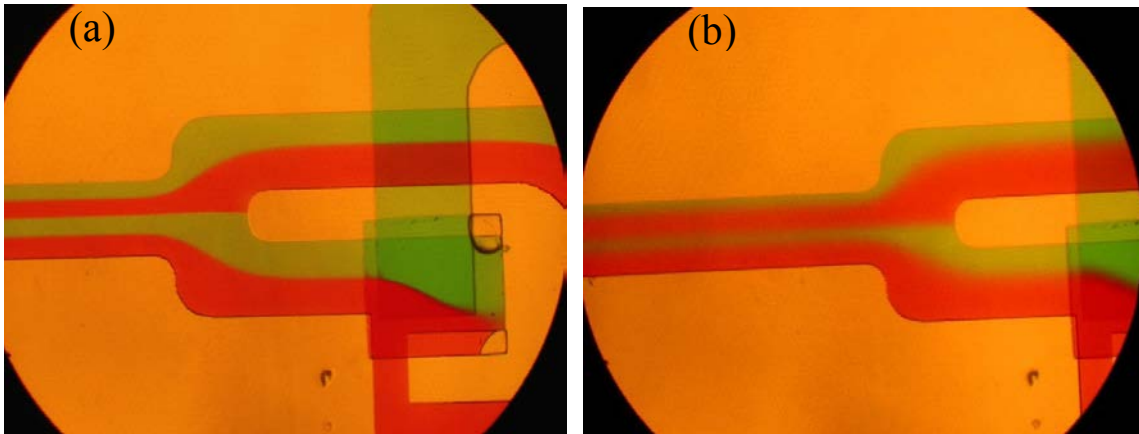


Figure 4-9: Flow visualization of the proposed micromixer using green and red flows. (a) High flow rate of 400 $\mu\text{l}/\text{min}$  ( $Re \sim 55$ ) to minimize the diffusion for better visualization; (b) The thickness of the green flow is decreasing along the flow which shows the green flow is diffusing into the red at rate of 40 $\mu\text{l}/\text{min}$  ( $Re \sim 5.5$ ).

#### ***4.5.2 Mixing testing of acid and base***

In the previous experiment, the mixing is assessed qualitatively by using the colored flows. In order to determine the performance of the proposed micromixer quantitatively,

an experimental layout is designed to obtain the variation of mixture concentration profile at the outlet. Figure 4-10-a and d show the layout and the fabricated chip, respectively.

In order to assess the performance of mixing, variation of pH value along the width of the channel is measured by branching the outlet into four branches as depicted in Figure 4-10-a. More number of branches would be beneficial for better evaluation of the pH variation in the channel. The outlet of mixer channel is divided into four branches with equal width as a result of having four sub-streams in the micromixer outlet. The pH value which is measured in each branch is represented by the average pH of sub-stream (with the thickness of  $50\mu\text{m}$ ) of the micromixer at its middle point which is schematically depicted in Figure 4-10-a. The configuration is designed in a way to ensure that each of the four sub-streams is connected to one of pH meters to be able to precisely study the concentration at the outlet cross section.

The mixing experiments consist of mixing an acid (hydrochloric acid) and a base (sodium bicarbonate). To make solutions 0.83ml of concentrated HCl (37%) from Fisher Scientific was diluted into 1L of DI-water to make 10mM HCl solution with a pH of 2 and 400mg of NaOH was solved in 1L DI-water to have a 10mM base solution with a pH of 12. When complete mixing of acid and base occurs, pH of the mixed solution would be 7. The solutions were introduced into the mixer with similar flow rates using a syringe pump. Each outlet was collected and a pH meter was used to measure the pH. The test was performed at different inlet flow rates. The typical measured pH graph that was used to estimate the efficiency is shown in Figure 4-10-b corresponding to  $200\mu\text{l}/\text{min}$ . The hatched area in this figure represents the mixed fluids and red and green lines correspond

to no-mixing and full-mixing situations respectively. The differences between the measured pH and the pH=7 (full mixing) was used to calculate the efficiency.

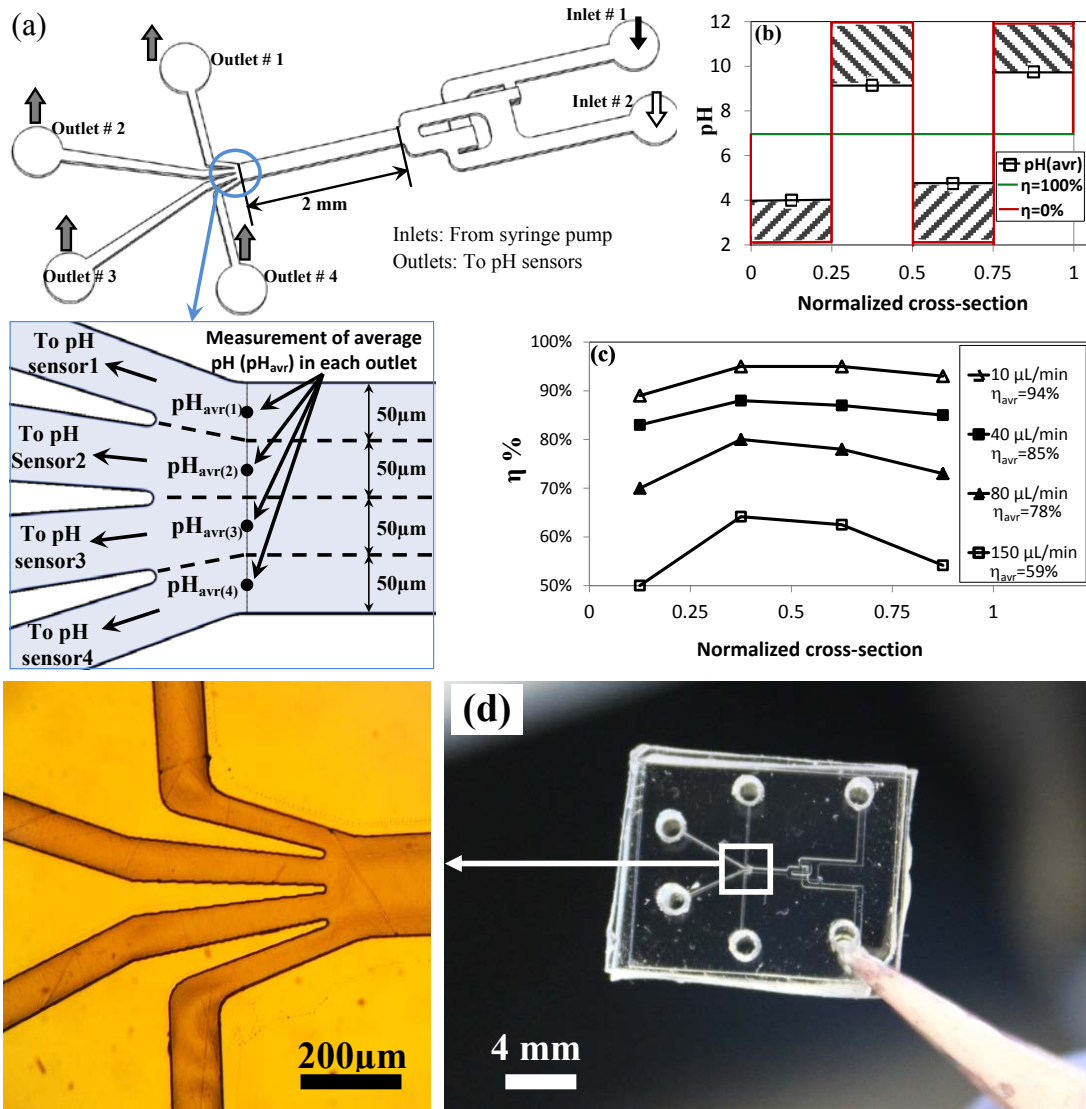


Figure 4-10: Evaluation of the micromixer performance in real conditions; (a) a layout with four branches designed to precisely measure the variation of pH in the cross-section of the mixer outlet, (b) measured pH used for estimation of efficiency. The black line shows measured values and the hatched area represents the mixed fluids, (c) The variation of efficiency along the outlet cross-section and the average efficiency for each flow rates, (d) the fabricated device.

The variation of efficiency along the outlet cross-section at different flow rates is shown in Figure 4-10-c. The average efficiency ( $\eta_{avr}$ ) for each flow rate is also shown in this

figure. From this graph is it clear that the mixer achieves very high efficiencies specifically at low flow rates. The two liquids can be assumed as fully mixed for the flow rates less than around 50 $\mu$ l/min.

## 4.6 Conclusion

A "*simple*" and "*cheap*" PDMS micromixer is designed, optimized, fabricated, and successfully characterized in this work. The 3D mixing mechanism is based on *split-and-recombinant* flows through a 3-layer design. The mixer channel dimensions are then optimized in order to reach high performance. A quantitative method is proposed to evaluate the mixing efficiency of simulation results. The simulation results show the proposed mixer can achieve fully mixing ( $\eta > 80\%$ ) for flow rates up to 15 $\mu$ l/min ( $R_e < 2.2$ ) which is acceptable for the typical micromixer working range.

The device was fabricated and the flow was visualized in the channels. Mixing experiments were designed in order to precisely evaluate the variation of concentration at the outlet and to assess the mixing performance quantitatively. The experiment performed by branching the outlet into four branches due to having four sub-streams in the mixer outlet. The results show that the mixing is even better than the simulation results. A mixing efficiency of 85% obtained at flow rates of 40 $\mu$ l/min meaning fully mixing for  $R_e < 5.5$ . The results established the proposed mixer as a good candidate to be used in real chemical and biological applications that generally operates in low flow rate regime. The whole PDMS structure of the device makes it possible to be easily integrated with other microfluidic devices in a LoC platform for clinical diagnostics and point-of-care applications.

## **Chapter 5: Gold nanoparticles integrated PDMS microfluidic chip for lab-on-a-chip plasmonic biosensing of growth hormones**

As we already reported in chapter 2, the *in-situ* synthesis of gold nanoparticle was presented and used in a macro-scale environment. Toward the main objective of the work, we should carry out the synthesis method inside a microfluidics.

In this chapter, the integration of *in-situ* method in a microfluidic environment has been performed. In addition, the kinetics of the reaction in the micro-scale has been studied thoroughly and then the results compared with the macro-scale reaction obtained in chapter 2. At the final step, the proposed integrated microfluidic LSPR-sensor has been used for bovine growth hormone detection.

### **5.1 Introduction**

The development of biosensors for the detection of different biomolecules is an extremely important problem in life science and clinical diagnostics. With the recent advances in optics, microfabrication and nanotechnology, new biosensing methods are emerging for the development of sensitive and low-cost integrated biosensors.

The development of immunosensors based on the plasmonic properties of gold colloids is expanding rapidly [136]. The interest in the LSPR-based biosensors lies on their unique properties allowing label-free and real-time biomolecular analysis with possible detection

of biomolecular interactions (antigen-antibody interaction, DNA hybridization, etc.) at low-concentrations [137]. In addition, the simple detection mechanism of optical-based biosensors makes it possible to be integrated with different sensing platform for lab-on-a-chip application such as integrated microfluidic devices [138-140].

Microfluidics based biosensing is of interest for a wide spectrum of scientists from physicists and chemists to biologists due to their high-throughput and low-cost mass fabrication [141]. The combination of microfluidic devices with LSPR biosensors offers some significant advantages from both technologies and results in an improvement of overall performance of the biosensor. Indeed, a microfluidic device dramatically reduces the required sample/reagent volume. In addition, miniaturized channel footprints may results in an accelerated immunoreactions and a fast response [121].

Several papers on the integration of nanoparticles into the microfluidic devices for biosensing application have recently been published [142,143]. However, in the majority of these works, pre-synthesized NPs were introduced into the microfluidic system [144-148]. In addition, physical methods were also used to fabricate nanoparticles inside a microfluidic chip such as soft-lithography [149] and physical vapor deposition [150]. There are very few works that use *in-situ* methods for the synthesis of nanostructures [122] and nanoparticles [151] inside a microchannel for different bio-applications.

Furthermore, in the case of a microfluidic environment when the small dimensions induce some distinct properties, kinetic data are scarce [141]. Studying the kinetics of a chemical reaction provides a mathematical tool for the clear understanding of the underlying mechanism.

Miniaturization of the reaction platforms provides new opportunities for advanced synthesis, and opens the way for a broad range of novel applications [108,138]. In microreactors, both heat and mass transport are considerably accelerated due to large surface area to volume ratios within the microchannels, allowing rapid and homogeneous mixing. A great variety of nanoparticles have been synthesized in a microfluidic environment and their quality in terms of size distribution has also been emphasized [119,152,153]. The majority of these works were carried out by mixing liquid reactants in a microfluidic channel, using either a continuous flow, or droplet-based methods. In spite of the qualitative assessment of the high reaction rates in microchannels, few works are focused specifically on the evaluation of the kinetic parameters [120,154,155]. In the case of *in-situ* (heterogeneous) reaction, the reaction takes place inside, or on the surface of a polymer network and one of the reactants is the polymer itself or a component of the polymer compound and therefore the reaction rate is slower. The reaction results in the formation of a composite material, for instance, a gold–polymer nanocomposite, when a gold precursor solution is introduced into the polymer. To the best of our knowledge, the kinetics of an *in-situ* synthesis has not been studied in a microfluidic environment.

In this work, a novel nano-integrated microfluidic biosensor is proposed for the detection of Ag-Ab interaction through LSPR properties of gold nanoparticles. For this purpose, the kinetics of the *in-situ* synthesis of Au-PDMS nanocomposite in a microfluidic chip is thoroughly investigated. The particularities of this reaction compared with the reaction carried out in macro level are highlighted and the reduction mechanism of the gold ions in the microchannel is discussed.

The SEM images and spectroscopy were used for the characterization of nanoparticles. The sensitivity of the synthesized nanoparticles to the surrounding medium is then studied to assess the biosensing capability of the sensing platform. The microfluidic biosensor is then used for the detection of bST (or bovine growth hormone (BGH)). The results show a high potential of the proposed biosensor for clinical applications.

## **5.2 Material and methods**

### ***5.2.1 Materials***

Sylgard® 184 elastomer kit from Dow Corning Corporation was used for PDMS fabrication and SU-8-2035 was purchased from MicroChem. Gold chloride trihydrate ( $\text{HAuCl}_4 \cdot 3\text{H}_2\text{O}$ ) was purchased from Alfa Aesar and 1-pentanol, toluene, N, N-dimethylformamid, 2-propanol and ethyl alcohol, from Sigma-Aldrich. Nanothink® 18, TWEEN® 20, N-Hydroxysuccinimide (NHS), and N-(3-Dimethylaminopropyl)-N'-ethylcarbodiimide hydrochloride (EDC) were purchased from Sigma Aldrich. A monoclonal Bovine Growth Hormone antibody (anti-BGH or bST) in mouse and BGH antigen were purchased from Dr. Parlow National Hormone and Peptide Program in California, USA.

### ***5.2.2 Fabrication of PDMS microfluidic chip and in-situ synthesis of Au-PDMS***

For the fabrication of PDMS microfluidic chip (or cell), SU-8 photoresist (from MicroChem) standard patterning process was used. The procedure for the SU-8 mold fabrication consists of several steps. For mold fabrication, the SU-8 was spin coated (at

500rpm for 15 sec followed by 1500rpm for 30s) on a cleaned wafer and then soft-baked at 95°C for 10 min. The soft-backed SU-8 was exposed to UV light followed by a post-baking process for 7 min at 95°C. Afterward, the SU-8 was developed. Finally the mold is hard-baked at 200°C for 15 minutes. The mold was silanized in vapor phase to enable removing PDMS from the mold after curing. These steps are schematically illustrated in Figure 5-1a (steps 1 to 4).

For PDMS fabrication, the base polymer (pre-polymer) and the curing agent (cross-linking agent) are mixed (ratio 10:1 by weight). The fabrication is followed by removing the air bubbles in a vacuum desiccator for 10 minutes. The mixture is then poured into the SU-8 mold and, after a second degasifying process the mold is kept in oven at 60°C for curing overnight. Afterward, the cured molded PDMS is peeled off from the mold as shown in Figure 5-1a (step5). A flat PDMS layer (Figure 5-1a-step 6) was then bonded using oxygen plasma treatment with the prepared channel layer to close the channel. In Figure 5-1a a chip with two channels of 400 $\mu$ m width is shown. For simplicity, it will be referred as C400-2 (400-2 microfluidic chip), where the first and second terms indicate for the number of channels and the width of channel, respectively. In this work two microfluidic chips (C400-1 and C400-2) were used for the experiments.

Aqueous solutions of chloroauric acid with different concentrations were prepared. For the fabrication of gold-PDMS nanocomposite in a macro environment, the flat PDMS samples were cut into 1cm $\times$ 4cm pieces and the samples were incubated in the gold precursor solution for different times [63]. To prepare the gold nanocomposite inside the microfluidic chip, the solution was introduced into the microchannel with a syringe ( $\sim$ 5 $\mu$ l) and then the whole chip was kept at different temperatures for different times. To

avoid the evaporation of the solution, the inlet/outlet was closed. In Figure 5-1a fabricated microchannels with gold nanocomposite (red channels) is shown. The synthesis time of this cell was 48 hours.

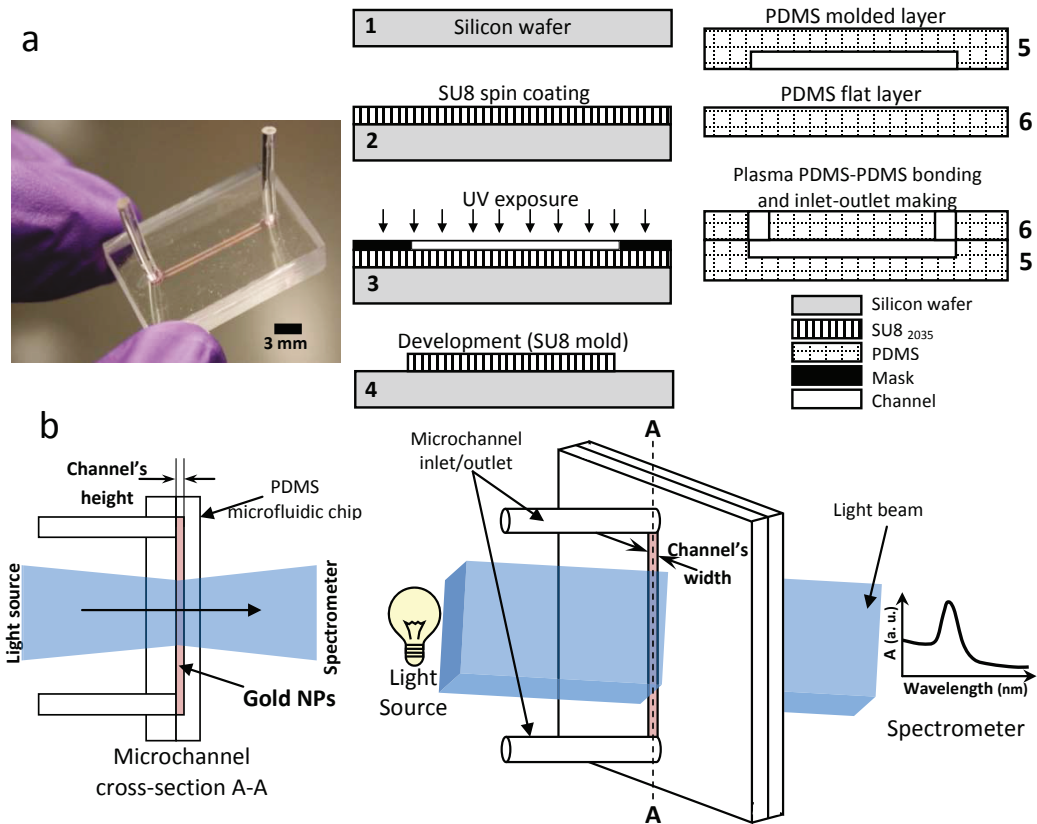


Figure 5-1: Fabrication procedure of microfluidic chip and measurement of its spectral band (a) Step-by-step fabrication procedure of SU-8 mold and PDMS microfluidics. The figure shows a chip with two channels (C400-2) and the red color of the channels indicates the synthesized AuNPs; (b) the microfluidic chip was placed directly in a spectrophotometer in order to measure the gold plasmon band.

As it shown in our previous work [63], the curing agent in PDMS reduces the gold ions to gold nanoparticles embedded into the polymer network. The relatively high concentrations of the gold precursor were used in order to increase the rate of the

reaction. The effects of concentration of gold precursor (ranging from 0.5% to 2%) and of the temperature (22°C, 40°C, and 50°C) on the kinetics of the synthesis reaction was investigated. The gold nanocomposites formed in the microchannel have been characterized by UV-Visible spectroscopy and Scanning Electron Microscopy (SEM).

The gold plasmon bands of the chips were measured using a UV/Vis spectrophotometer (LAMBDA 650 UV/Vis Spectrophotometer from PerkinElmer) as shown in Figure 5-1b. Due to low magnitude of the absorbance (low amount of Au nanoparticles in the channel) for some cases, the spectrum is a bit noisy and a denoising MATLAB® code based on wavelet analysis was used to remove the low frequency noises [156].

To obtain the size distribution of particles from SEM images, Gwyddion 2.28, a modular program for data visualization and analysis was used. To obtain the graphs, several SEM images with similar magnification were used.

In addition, the samples were annealed to improve the distribution of gold NPs embedded in PDMS. Heat treatment also increases the concentration of Au NPs on the surface of the sample. For annealing, the samples have been heated from room temperature to 300°C in 10 minutes and then kept at this temperature for 30 min. It was observed that temperature higher than 350°C is not suitable as it resulted in deformation of the chip.

### ***5.2.3 Sensitivity Tests***

Generally, the Au-LSPR band has been found to shift to longer wavelengths (red shift) as the surrounding medium's refractive index ( $n$ ) is increased [101]. The sensitivity of the Au-nanocomposite microfluidic platform with respect to the environments with different refractive indices has been investigated. For this purpose, five solvents with different

refractive indices have been selected. Each solvent was passed through a C400-2 and the corresponding LSPR band was recorded. The sensitivity for each chip (both annealed and non-annealed samples) has been calculated from the plot of  $\Delta\lambda_{max}$  against  $\Delta n$ , where  $\Delta\lambda_{max}$  is the gold LSPR band shift in a solvent (in nm) compared with the LSPR band position measured using deionized water, and  $\Delta n$  is the refractive index difference between the solvent and DI-water and is equal to  $\Delta n = n_{solvent} - n_{water}$  where  $n_{water} = 1.33$ .

#### ***5.2.4 Biosensing protocol***

Label-free biosensing tests have been performed by using the annealed C400-2. The bST antibody (anti-BGH) obtained in mouse and its corresponding antigen (Ag) was used for biosensing experiments.

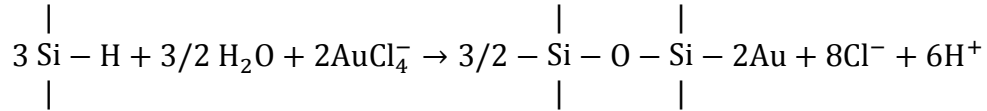
The first step of biosensing protocol consists in functionalizing the gold nanoparticles with 11-mercaptoundecanoic acid (NanoThink® ACID11) in ethanol (5mM), by introducing the solution into the microchannel and keeping it for at least 5 hours. After attaching the linker, the conventional carbodiimide coupling chemistry (EDC/NHS) is used to activate the carboxyl groups, before attaching the antibody (Ab). The activation is carried out by injecting a mixture of N-(3-dimethylaminopropyl)-N'-ethylcarbodiimide hydrochloride (EDC, 0.4M) and N-hydroxysuccinimide (NHS, 0.1M) for 1 hour (1:1 ratio by volume). The next step consists of attaching the antibody dissolved in a PBS buffer solution (200ng/ml) to the functionalized Au NPs, followed by washing the microchannel several times with a TWEEN® 20 solution in PBS (0.05%). The last step is attaching the Ag dissolved in a buffer solution by injecting the growth hormone solution into the microchannel. The samples were washed with PBS afterward. The spectra of the

microfluidic cell were recorded after each step. Different antigen concentrations were tested to obtain the limit of detection of the proposed biosensor.

## 5.3 Results and Discussion

### 5.3.1 *In-situ synthesis and kinetical study of the reaction*

The following reduction reaction between the gold ions and curing (cross-linking) agent has been suggested [74]:



To characterize the Au-PDMS nanocomposite form inside the microchannel, UV/Vis spectroscopy was used. The formation of gold-PDMS nanocomposite has been studied by using cells with different configurations. Based on the results, the absorbance found to vary linearly with the number of channels and width of the channel. For instance, for similar synthesis conditions (time, temperature, and gold salt concentration), the absorbance of a cell with 3 channels is about 3 times higher than that of a cell with only one channel with similar widths. However, due to small values of absorbance for microfluidic cells, higher absorbance generally has the advantages of less noise in the spectra and an improved accuracy in the measurements.

To study the kinetics of gold synthesis in a microfluidic environment, the UV-Visible spectra of a microfluidic chip (C400-1) under different conditions of concentrations (1% and 2% of gold salt) and temperatures (22°C, 40°C and 50°C) were measured (Figure 5-2a and Figure 5-2c).

Figure 5-2-a shows that the kinetics of formation of AuNPs is similar for 1% and 2% gold concentrations. However, the absorbance is higher for higher concentration of the gold salt, due to a higher number of particles formed in a unit area. The graph shows that the evolution of the reduction reaction can be described through three main phases: induction, when there are only a few particles on the surface; the actual formation step when, the absorbance shows a linear relationship with time and, finally, the step of saturation. As it is shown in Figure 5-2a, the induction step takes around 3-5 hours and the saturation phase was reached only after around five days (130hrs) of reaction.

The long induction and reaction times can be accounted by the particularities of this *in-situ* reaction. The reaction takes place between the gold ions in an aqueous solution and the cross-linking agent (a vinyl silicon compound) that is embedded in the polymer network. The amount of the cross-linking agent (curing agent) available for the reduction of  $\text{Au}^{3+}$  depends on the ratio of pre-polymer and cross-linking agent used for the fabrication of PDMS. These reductant molecules are migrating toward the surface of the channel and their diffusion is very slow (dashed arrows in Figure 5-2f). The effect of the concentration of the cross-linking agent on the rate constant is shown in Figure 5-2b. It can be seen that the rate constant increased considerably when the PDMS is fabricated by using a higher amount of cross-linking agent (4:1 compared to 10:1). This also confirms that assumption regarding the role of the cross-linking agent as a reductant.

In addition, the effect of temperature was investigated to have a more clear understanding of the kinetics of the reduction of gold ions in a micro environment. Figure 5-2c shows the first 30 hours of evolution of the reaction in a C400-1 corresponding to three different temperatures (22°C, 40°C, and 50°C). The absorbance-time slope (linear segment of

Figure 5-2c) was used to calculate the apparent reaction rate constants. The apparent rate constants of the reduction reaction ( $k^*$ ) are shown in Table 5-1 for different temperatures. In this table, the induction time (in minutes) and the half-life of the reaction,  $\tau_{1/2}$ , are also given. The data were derived here from spectrometric measurements and therefore they denoted as apparent rates and apparent activation energy.

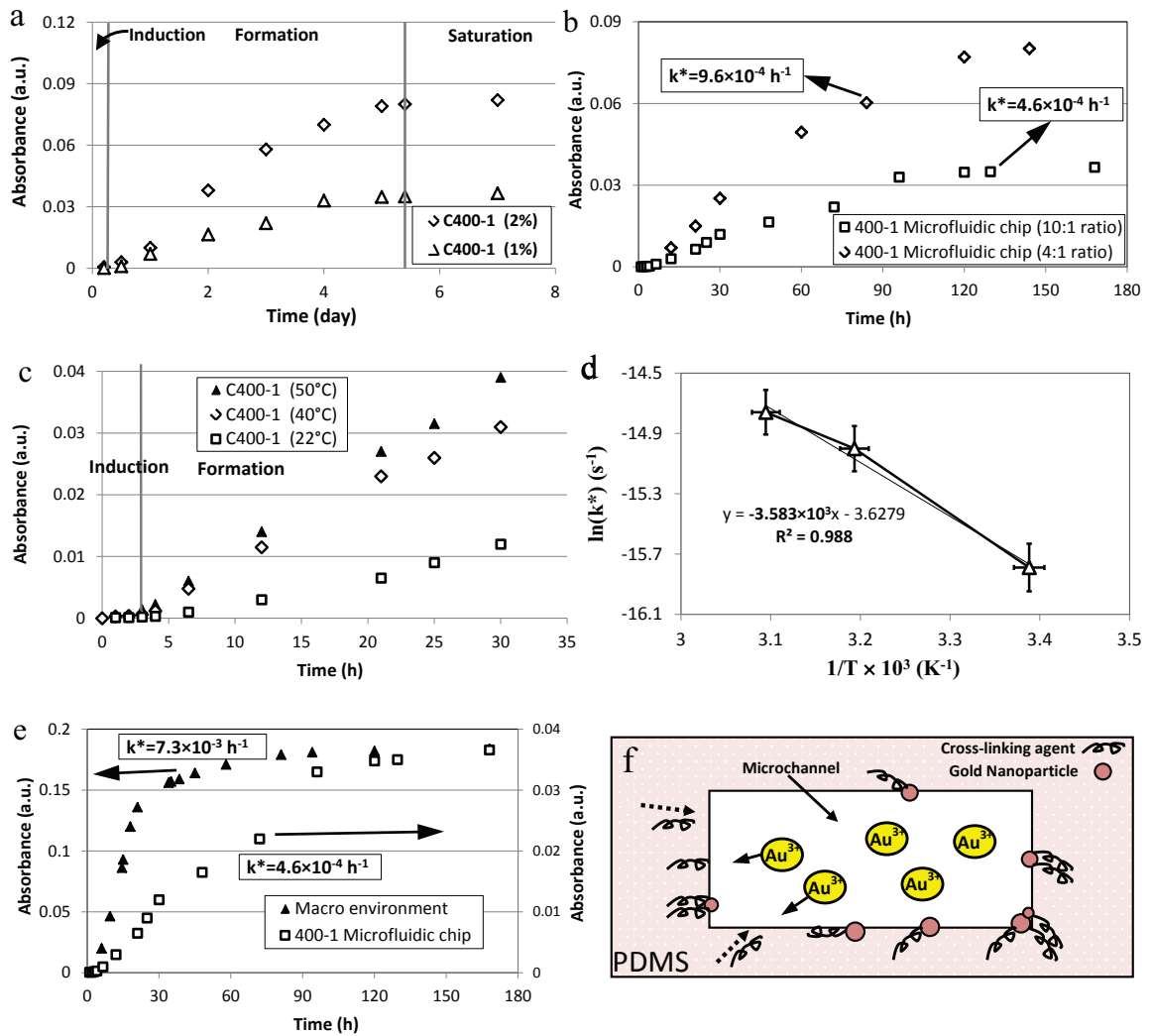


Figure 5-2: Study of the kinetics of the reduction reaction; (a) Absorbance-time plots of the reaction in C400-1 corresponding to 1% and 2% gold salt concentrations at room temperature, (b) The effect of PDMS cross-linking agent on the evolution of gold nanoparticles formation (c) The effect of temperature on the evolution of formation of gold nanoparticles by using a 1% gold salt solution (d) Arrhenius plot for the calculation of apparent activation energy (e) comparison of evolution of the gold into PDMS in microchannel and in macro-scale environment, (f) Illustration of microfluidic chip cross-section and the migration of reducing agent toward the channel wall.

Table 5-1: The apparent rate constants of the formation of gold NPs at different temperatures

Temperature (°C)	Induction Time (min)	$\tau_{1/2}$ (min)	$k^*$ (h <sup>-1</sup> )
22 ±0.5	330	3960	0.5×10 <sup>-3</sup>
40 ±0.5	240	3540	1.1×10 <sup>-3</sup>
50 ±0.5	180	3360	1.4×10 <sup>-3</sup>

The Arrhenius equation is used to calculate the activation energy  $E_a$  of a reaction as follows:

$$k = Ae^{-E_a/RT} \rightarrow \ln(k) = -\frac{E_a}{R} \frac{1}{T} + \ln(A) \quad (5-1)$$

Where  $A$  is the pre-exponential (or frequency) factor,  $k$  is the rate constant of the reaction at the temperature  $T$  (in Kelvin) and  $R$  is the universal gas constant ( $R=8.314 \text{ J/mol.K}$ ).

The activation energy is expressed in  $J/mol$ .

Considering that the gold ion reduction reaction has a rate constant that obeys the Arrhenius equation, a plot of  $\ln(k^*)$  (in  $s^{-1}$ ) versus  $T^{-1}$  follows a straight line as shown in Figure 5-2d . The slope of the Arrhenius plot (Figure 5-2d) was used to extract the apparent activation energy,  $E_a^*$ , of the reaction using the following equation:

$$E_a^* = -R \times \left( \frac{\ln(k)}{\frac{1}{T}} \right) = 29.8 \frac{\text{kJ}}{\text{mol}} \quad (5-2)$$

The relatively large value of the activation energy ( $E_a^* \sim 30 \text{ kJ/mol}$ ) shows that the reaction needs a high energy contribution. The reaction is facilitated at high temperatures when the migration of the reducing agent is faster.

The apparent rate constant determined in the microchannel environment is compared to that corresponding to the reaction carried out at macro-scale [63] under similar conditions and the results are compared in Figure 5-2e. The reaction rate in microfluidic environment is  $k^*=4.6\times 10^{-4}\text{h}^{-1}$  and in macro environment is  $k^*=7.3\times 10^{-3}\text{h}^{-1}$ . These results show that the reaction is approximately 16 times slower in the microchannel due to less favorable conditions for mixing of the reactants. The schematic shown in Figure 5-2f illustrates how the reduction reaction takes place in the microchannel. The schematic also shows how migration of cross-linking agent to the channel surface can take place. The lower reaction rate indicated in microfluidic environment is also due to the effect of the channel wall that may adsorb (immobilize) the gold ions and the cross-linking agent.

Therefore, in the case of this *in-situ* heterogeneous reaction, the microfluidic environment has not enhanced the rate of reaction as seen. However, as seen in the section 3.2, the size distribution of gold NPs synthesized in the microchannel was significantly narrower providing better uniformity of size of the particles

### ***5.3.2 Particle size distribution in micro and macro environments***

SEM imaging was used to characterize the size and distribution of AuNPs in the annealed microchannel. To take the image of the particles inside the channels, the PDMS-PDMS bonding was removed. Figure 5-3a shows the SEM image of particles formed in a 400-1 microfluidic cell prepared by introducing a 1% solution of gold precursor for 24h in the channel. The channel edge is shown in the SEM image. The inset of the figure shows a close-up of gold particles with the size of around 100 nm.

The annealing process improves the uniformity of the particle morphology and it can be seen in SEM images by the narrower size distribution and less particle aggregations and indicated by the blue shift of the Au-LSPR band [63]. The improvement is evaluated by a blue shift of the band which is  $\sim 8\text{nm}$  shift in macro environment compared to only  $\sim 2\text{nm}$  shift in a microchannel environment. This is due to the fact that the distribution of the synthesized particles in the non-annealed microchannel is more uniform than in the sample prepared in macro environment even before annealing. Therefore it can be inferred that the annealing treatment does not have a significant effect of the gold nanoparticles prepared in a microfluidic environment.

To show difference between the size distributions of gold nanoparticles prepared in the microfluidic chips compared to particles prepared in a macro environment, gold nanocomposites were prepared in microchannel as well as in a macro environment. Gold nanoparticles integrated microfluidic chip was prepared by keeping a 2% solution of gold salt for 48h in the channel. The same conditions are used to fabricate a gold-PDMS nanocomposite by incubating of PDMS samples in gold solution (macro environment). Both samples were annealed.

The SEM image and the corresponding histogram of particle size distribution for the C400-1 and for macro sample are shown in Figure 5-3b and Figure 5-3c respectively. It is clear from these two figures that the size distribution of the particles in the microchannel (Figure 5-3b) is narrower than the distribution in macro environment (Figure 5-3c) which is one of the main advantages of synthesis in microfluidic environment. It could be seen in Figure 5-3b and c that the particle size in the channel has a band of  $125\pm 5\text{nm}$  compared to bandwidth of  $140\pm 35\text{nm}$  in macro sample. This is in agreement with the

shape of the gold-LSPR band in both micro and macro sample which is shown in Figure 5-3d.

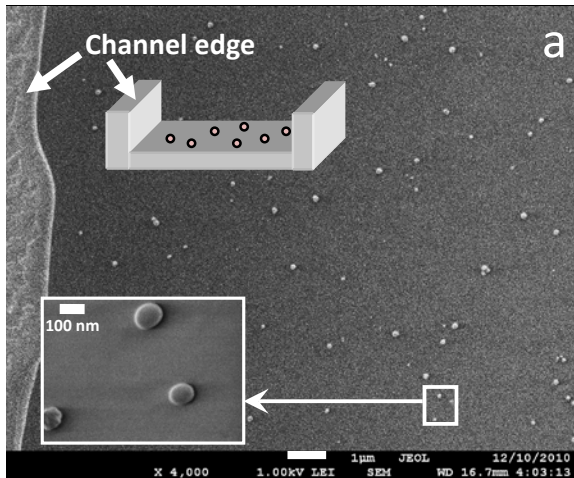


Figure 5-3: SEM images and particle size distribution of annealed cells; (a) a microchannel and formation of gold NPs on the channel surfaces. At the left side, the channel edge is shown and the inset shows the shape of particles. (b and c) SEM image and the corresponding size distribution of Gold NPs prepared by 2% solution of gold precursor for 48h of incubation for two different (c: microchannel and d: macro-scale) environments; (d) Au-LSPR band of nanocomposite prepared in microchannel and macro-scale environment.

Narrower particle distribution on the surface will result in improved sensing properties of the microfluidic platform and could enhance the detection limit of the proposed microfluidic biosensor.

### 5.3.3 Sensing experiments

#### 5.3.3.1 Sensitivity test

The sensitivity test is a good way to assess the biosensing capability of a sensing platform. In order to determine the sensitivity of the platform, experiments were conducted in media of different refractive indices (RI). By increasing the refractive index of the surrounding medium, the Au-band is shifted to longer wavelengths. For this purpose, two sets of five identical 400-2 chip were prepared and one set was annealed. For each solvent, the solution was introduced into the channel and its spectrum was recorded. The sensitivity graphs for both non-annealed and annealed cells are shown in Figure 5-4.

The results show that the annealed sample has a sensitivity as high as 74 nm/RIU which makes it very useful for label-free biosensing application. The sensitivity for the non-annealed samples is about 65 nm/RIU. The similar values of the sensitivities shows that the annealing treatment has less effect on uniformity and sensitivity in a microfluidic environment as discussed in section 3.2.

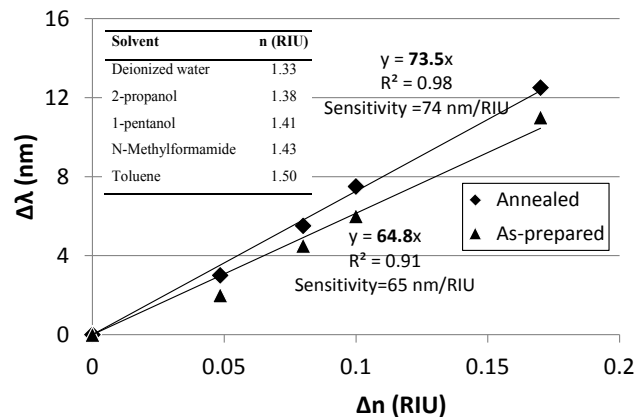


Figure 5-4: Sensitivity tests of the 400-2 microfluidic cell prepared from 2% aqueous solution of gold for 48h.

### **5.3.3.2 Biosensing capability of the proposed biosensor and the detection limit of BGH**

The microfluidic biosensor integrated with gold NP, prepared and annealed as described earlier, tested for biosensing of bST. The biosensing experiment involves the antigen-antibody interaction detection of the bovine growth hormone in mouse through the spectra of the sample recorded at different steps. Annealed 400-2 microfluidic cells were used for these tests. A cross-section of the microchannel with embedded gold nanoparticles is shown in Figure 5-5-a and the different steps of the biosensing experiment are schematically depicted in Figure 5-5b.

The Au LSPR band shifts to longer wavelength after each step, as an evidence of attaching the biomolecule to the AuNPs results in a decreased refractive index of the gold nanoparticles medium. During the last step (attaching of the Ag) the shift is mainly due to the Ab-Ag interaction. The spectra corresponding to the different steps of the biosensing experiment are shown in Figure 5-5d.

To obtain the detection limit of our proposed biosensor for the detection of growth hormone, antigen with different concentration (80ng/ml, 40ng/ml, and 10ng/ml) were tested for biosensing. The corresponding LSPR shift was recorded for each concentration. A detection limit of 4ng/mL is obtained as shown in Figure 5-5e corresponding to 1nm precision of the measurement. The measured variation of red shift against the concentration of bovine growth hormone is shown in this figure.

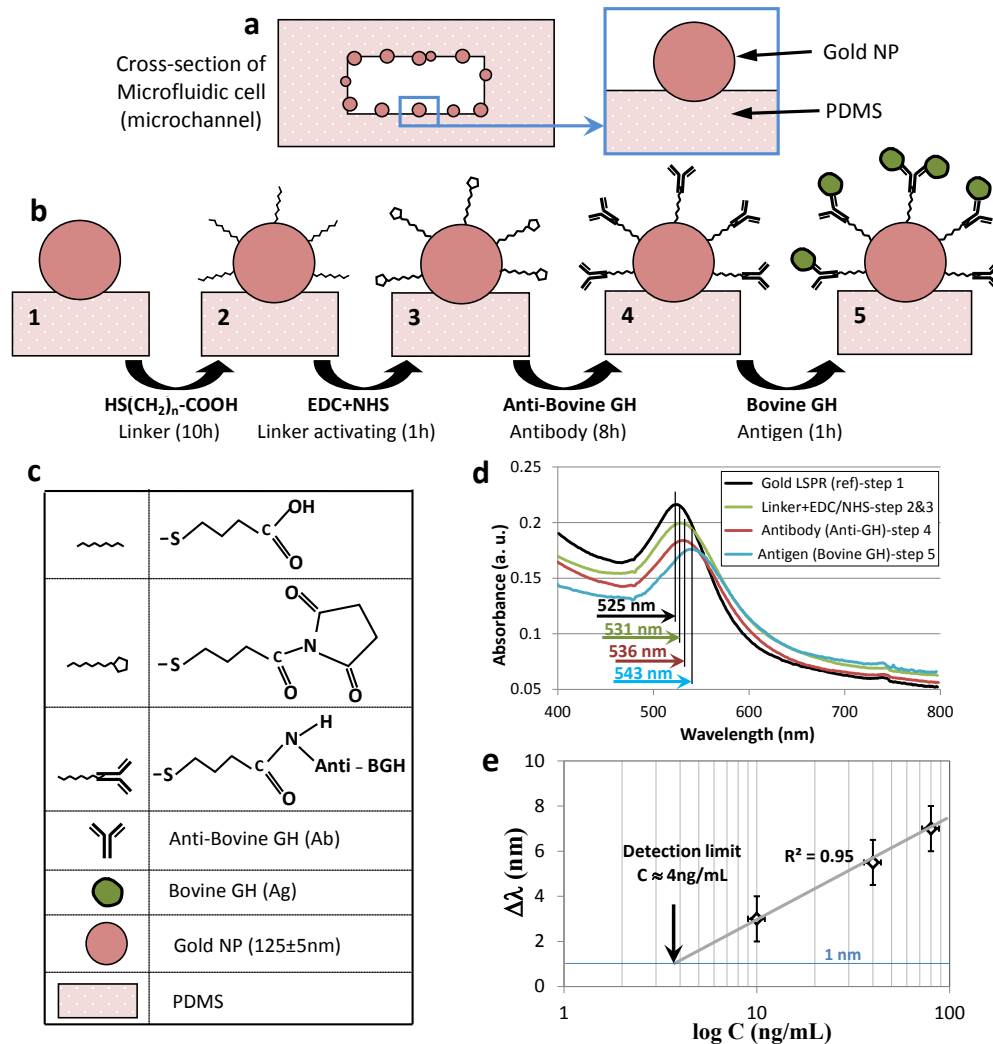


Figure 5-5: Biosensing experiments performed by using the annealed microfluidic biosensor (400-2 cells) prepared from 2% aqueous solution of the gold precursor (48h). (a) cross-section of a microchannel and AuNPs in the channel; (b) four steps of the biosensing protocol; (c) legend of the schematics; (d) Au-LSPR corresponding to the four sensing steps depicted in a; (e) LSPR band shift corresponding to different Ag concentrations.

## 5.4 Conclusions

Gold-PDMS nanocomposite was synthesized in a microfluidic channel through an *in-situ* reaction between a gold precursor and the cross-linking (curing) agent of the polymer. It found that the reaction is slower in the micro-environment than at a macro-scale. However, the size distribution of gold nanoparticles synthesized in the microchannel was

found to be 120-130 nm (8% size variation) as considerably improved and narrower compared to macro-scale sample resulted a range of 105-175 nm (67% size variation) which means around an order of magnitude (8.3 times) improvement in size uniformity. The kinetics of the synthesis was studied in detail and the apparent activation energy of the reaction was estimated  $E_a^* = 30\text{kJ/mol}$  by using the Arrhenius equation.

It was shown that, the annealing of the microfluidic chip affects only slightly the sensitivity of the platform due to the improved morphology of nanoparticles in microfluidic chip even before annealing treatment. The capability of the proposed microfluidic biosensor to detect bovine growth hormone based on antibody-antigen interaction was successfully demonstrated. The detection limit was found to be as low as 4ng/ml. This strategy demonstrated a successful integration of microfluidics and nanoparticles that can potentially provide an alternative towards the clinical detection of proteins.

## **Chapter 6: Realization of Polymeric Suspended**

### **Microfluidics**

This chapter report, for the very first time, the fabrication of polymeric free-standing structure with buried microfluidic. The realized device was called “*Polymeric Suspended Microfluidics*”. One of the final steps toward the main objective of this thesis is the integration of PDMS microcantilever with buried microchannel. In this chapter, the fabrication process of the PDMS microcantilever with buried microchannel which is called “*suspended PDMS-microfluidics (SPMF)*” is presented. To the best of our knowledge, this is the first report for the fabrication of such a Suspended Polymeric Microfluidics. In addition, the simulation has been performed in order to relate the deflection of the cantilever with its thickness. The simulation was further used to optimize the cantilever dimensions, mainly the cantilever thickness, in view of its application for biosensing. The optimization process is essential to improve the detection limit of the cantilever sensor.

### **6.1 Introduction**

Advances in microfabrication technologies are enabling a wide range of new possibilities. Over the past few years, progress in the fabrication of transducers technology with a more comprehensive understanding of the governing rules of biomolecular interactions, has led to rapid advancements in the development of biosensors [1].

Progresses in the microfabrication technologies made it possible to fabricate mechanical devices with moving parts in the range of a few microns or sub-micron, meaning even a

few nanometers [1,2]. These advancements have led to move from fundamental problems in biological physics toward fabrication of practical sensors that can be fabricated in batch.

In the past 20 years, the fabrication of microcantilever has advanced rapidly. The initial cantilevers were only used as AFM tips. Thundat [26] in 1995 opens a new window towards the application of microcantilever (MCs) in sensing. Many sensitive microcantilevers-based devices have been developed for different biosensing applications such as label-free biosensing, antigen-antibody interaction detection and DNA-hybridization in [30-42]. It should be noted that in all of these applications, the simple cantilevers were fabricated from silicon by etching of silicon [4].

The next generation of cantilever transducers was proposed by Burg in 2003 [43] when microfluidic systems have been integrated into the microcantilevers in order to make a sensitive device to measure the mass of a single molecule, or a nanoparticle with ultra-high resolution. The term “suspended micro-resonators (SMR)” refers to these types of integrated microcantilevers. Today many sensitive SMR devices are proposed that use similar principal for measurement of mass with a high sensitivity to the level of pico/femto gram resolution. To the best of our knowledge, only silicon was used as substrate to fabricate SMRs and the fabrication procedure is almost similar [44-47]. The fabrication of suspended microchannels is a very cumbersome process containing several complex steps. Generally, the fabrication procedure of SMRs encompasses two main steps. The first step is to make the buried channel in silicon by using polysilicon Damascene process, which includes etching of sacrificial layer in hot potassium

hydroxide. Second step is bulk micromachining to fabricate suspended microchannels with a wall thickness [43].

Polymers are rarely used for the fabrication of cantilevers. There are only a few works that used PDMS and other polymers for the fabrication of microcantilevers [157,158] by using Injection molding process. Furthermore, the suspended PDMS microfluidics (SPMF), or the fabrication of buried microchannel in a PDMS cantilever has not been investigated yet. One of the main reasons is the lack of a practical application for these types of polymeric cantilevers.

The reported PDMS cantilevers have always been used for non-biosensing applications due to the lack of a method to immobilize biomolecules on their surface. In fact, to the best of our knowledge, there is no effective method that can ensure effective immobilization of gold nanoparticles on the surface of PDMS that can be used further as a probe to immobilize biomolecules on them. This is the main reason that prevented PDMS microcantilevers from use in biosensing applications.

Earlier to this thesis, in Chapter 2, a simple method for effective immobilization of gold nanoparticles onto the PDMS surface is proposed. The method is based on the *in-situ* reduction of gold into PDMS surface. The prepared Au-PDMS nanocomposite showed very good biosensing capabilities toward the detection of antigen-antibody interaction. The method would be further integrated with SPMF toward the fabrication of sensitive cantilever-based biosensors.

In this chapter, for the first time, we proposed a method for the fabrication of “suspended polymeric-microfluidics” using PDMS. The fabricated device is referred to “*Suspended*

*PDMS-microfluidics* (SPMF)". COMSOL simulations were used to simulate the cantilever deflection behavior in order to optimize its dimensions. The optimized SPMF cantilever was then fabricated.

The platform will be further used for biosensing applications. For this purpose, following the fabrication of SPMF, gold nanoparticles (AuNPs) will be integrated onto the buried channel walls. Then the biomolecules will be immobilized on AuNPs inside the buried microfluidics. Through the interaction of biomolecules, a surface stress will be induced which results in bending of cantilever. Therefore, the dimensions of SPMF cantilever platform have to be optimized in order to reach the maximum deflection of cantilever.

## **6.2 Design and Fabrication of the SPMF cantilever**

For the fabrication of SPMF cantilever with buried microchannel, SU-8 photoresist (from MicroChem) patterning procedure was used to prepare two molds which were used further to fabricate the layers of the cantilever. A schematic of a cantilever is shown in Figure 6-1. As it can be seen in this figure, the cantilever contains 4 layers (two thick and two thin layers). These layers from top to bottom include: (1) top substrate layer for holding of the cantilever; (2) top cover layer to close the channel with the thickness of  $t_1$ ; (3) a microfluidic-structure layer containing the buried microchannel with the thickness of  $t_2$  and; (4) bottom substrate layer for holding of the cantilever.

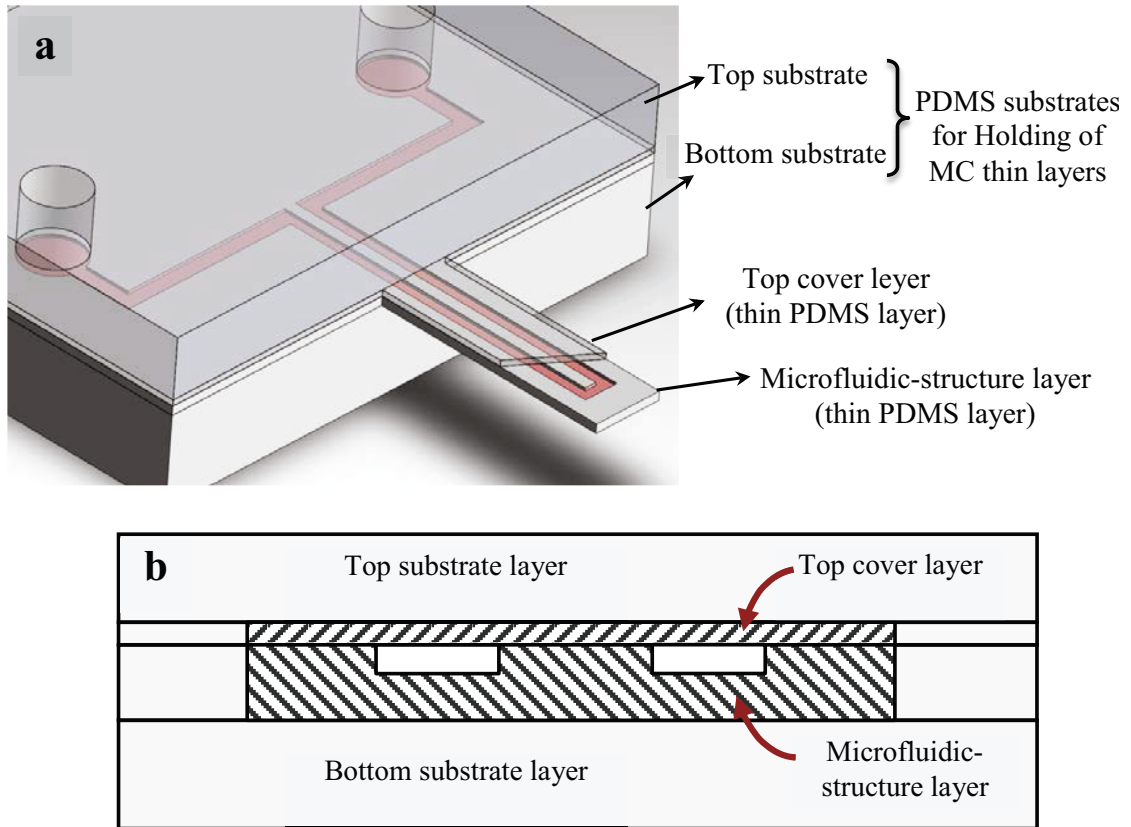


Figure 6-1: (a) Design of a cantilever with buried microchannel; (b) cross-section of the cantilever

### 6.2.1 Fabrication of SU-8 molds

Substrate layers are flat PDMS layers that can be fabricated easily by molding PDMS on a flat surface. However, for the fabrication of thin layers two SU-8 molds for cover layer and microfluidic-structure layer were fabricated. Preparation of top thin layer is a one stage standard SU-8 process. The steps are depicted in Figure 6-2.

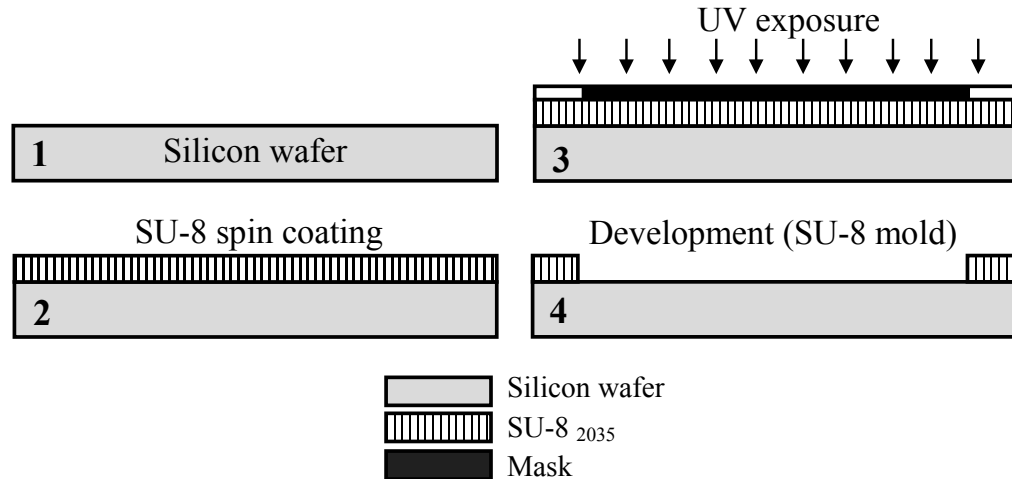


Figure 6-2: Fabrication of SU-8 mold for thin cover layer of SPMF.

For mold fabrication, SU-8 was spin coated with different thicknesses from  $t_I=15\mu\text{m}$  to  $t_I=150\mu\text{m}$  on a cleaned 4" wafer (Figure 6-2, step2) and then soft-baked at  $95^\circ\text{C}$  for 10-20 min. The soft-backed SU-8 was exposed to UV light followed by a post-baking process for 10-12 min at  $95^\circ\text{C}$  as mentioned in Figure 6-2 by step 3. Afterwards, the SU-8 was developed in SU-8 developer. Finally the mold is hard-baked at  $200^\circ\text{C}$  for 15 minutes (Figure 6-2, step 4). The mold was silanized in vapor phase to enable the removal of PDMS cover layer from the mold after curing.

It should be noted that the mold for cover layer were fabricated with different thicknesses ( $t_I=15\mu\text{m}$ ,  $t_I=25\mu\text{m}$ ,  $t_I=40\mu\text{m}$ ,  $t_I=60\mu\text{m}$ , and  $t_I=105\mu\text{m}$ ). The molds with different thicknesses ( $t_I$ ) were further used to fabricate cantilevers with different cover layer in order to find the optimized thickness of the cantilever cover layer.

The fabrication process of SU-8 mold for the microfluidic-structure layer is more complicated as it contains two different SU-8 levels. One level has a thickness of  $h=15\mu\text{m}$  and it forms the buried microchannel with the depth of  $h=15\mu\text{m}$  and the other

level forms the microfluidic-structure layer with the thickness  $t_1$  ( $t_2=60 \mu\text{m}$ ). The fabrication steps of this layer are shown in Figure 6-3 (steps 1 to 6).

The procedure for the fabrication of SU-8 mold of microfluidic ( $\mu\text{F}$ )-structure layer starts with spin coating of SU-8<sub>2010</sub> with the thicknesses of  $h=15\mu\text{m}$  on a cleaned 4" wafer (Figure 6-3, step 2) and then soft-baking at  $95^\circ\text{C}$  for 10-20 min. The soft-backed SU-8 was exposed to UV light followed by a post-exposure baking (PEB) at  $65^\circ\text{C}$  for 5 min as depicted in Figure 6-3 step 3. The PEB should be performed at a low temperature of  $65^\circ\text{C}$  due to two main issues: (i) Even at low-temperature PEB, an image of the pattern would be visible in the SU-8 2010 coated layer. These images can be used as reference to align the second mask. (ii) Low-temperature PEB avoids the appearance of bubbles on the unexposed parts of SU-8. As a result, low-temperature PEB does not deteriorate the smoothness of first SU-8 (2010) surface which is going to be used for the second SU-8 (2035) spin coating.

The second SU-8<sub>2035</sub> layer was spin coated on the first layer to the thickness of  $t_2=45 \mu\text{m}$  followed by soft baking of the wafer at  $95^\circ\text{C}$  for 15 min (Figure 6-3 step 4). Then, the wafer is exposed to UV light followed by PEB at  $95^\circ\text{C}$  for 10 min as shown in Figure 6-3, step 5. It should be noted that before the second UV exposure, the mask should be aligned to the previous patterns by using the visible image of the previous layer's features. This is a very important step as any miss-alignment, will cause that the buried microchannel will not be at the center of the cantilever.

In the next step, both SU-8 layers were developed in SU-8 developer and the mold obtained as shown in step 6 of Figure 6-3. Finally the mold is hard-baked at  $200^\circ\text{C}$  for 15

minutes. The mold was silanized in vapor phase to enable the removal of PDMS from the mold after curing. Figure 6-4 shows the fabricated mold for the  $\mu$ F-structure layer of SPMF. In this figure the close-up images show different SU-8 level of patterns. The lower lever will make the buried microchannels. The inset image in this figure shows the mold that was used for the fabrication of cover layer.

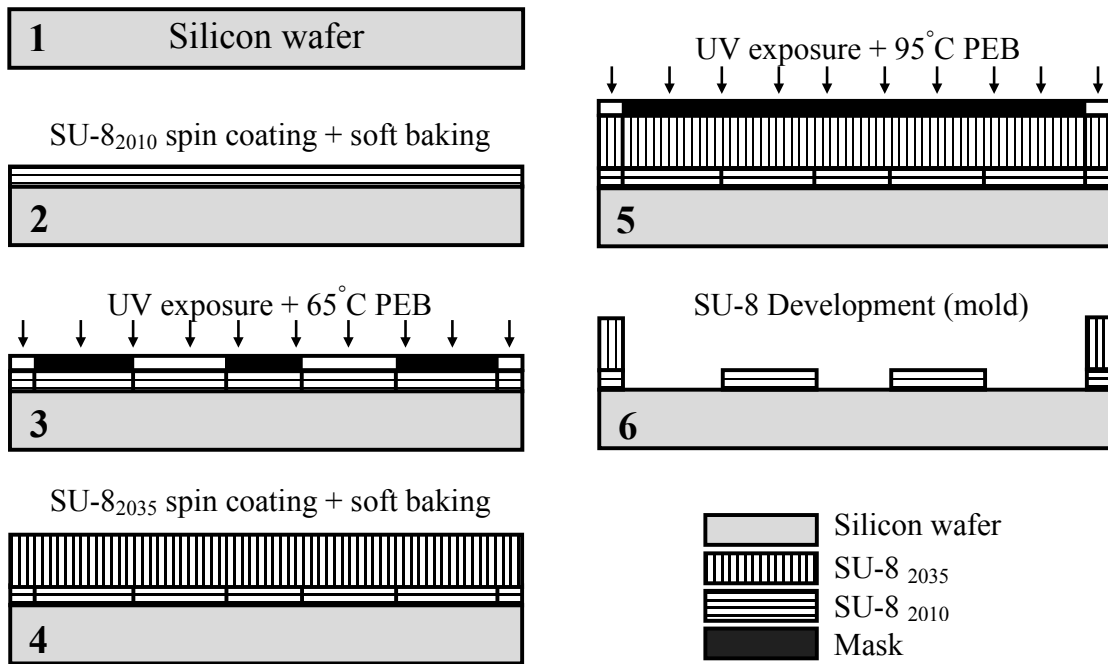


Figure 6-3: Fabrication of mold for the microfluidic-structure layer of SPMF.

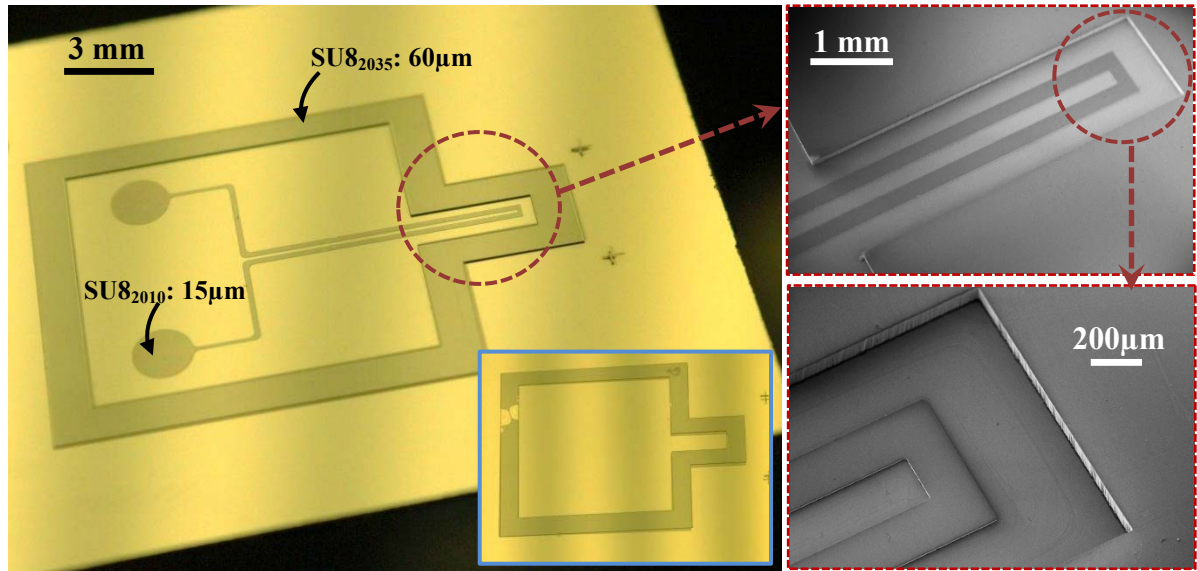


Figure 6-4: Images of the fabricated mold for thin layers. The SU-8 mold for bottom thin layer is shown and its SEM images demonstrate two different SU-8 levels. The inset shows the top thin layer of the SU-8 mold.

### 6.2.2 Fabrication of suspended PDMS microfluidics (SPMF)

After fabrication of SU-8 molds, the PDMS was used for the fabrication of cantilever with buried microchannel. PDMS compound was prepared by mixing the base polymer (pre-polymer) and the curing agent (cross-linking agent) with the weight ratio of 10:1. The process is followed by the removal of air bubbles in a vacuum desiccator for 10 minutes. Substrate layers are fabricated by using a simple flat surface as a mold. PDMS was poured to a thickness of 1-2 mm in the flat mold and then cured at 60°C for at least 4h. The layers were then peeled off from the surface and were cut into rectangular shapes. Thin layers of the SPMF were fabricated by using the PDMS thin layer fabrication method. The fabrication process for two thin layers of cover layer and  $\mu$ F-structure layer are shown schematically in Figure 6-5-a and b, respectively.

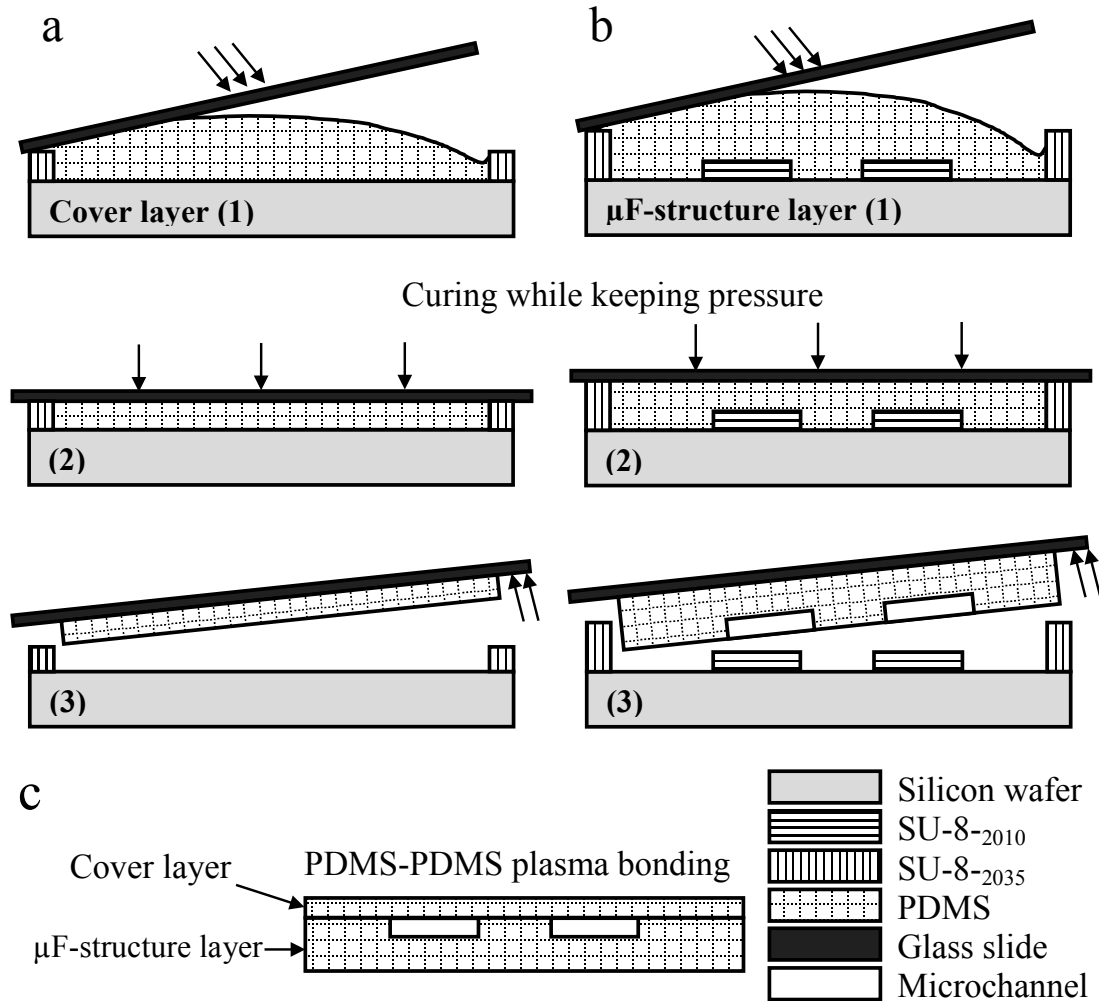


Figure 6-5: thin layers fabrication procedure (a) fabrication of cover layer; (b) fabrication of  $\mu$ F-structure layer; (c) PDMS-PDMS bonding of thin layers for form a closed microchannel.

The fabrication of cover layer and  $\mu$ F-structure layer is similar. First, PDMS was poured into the mold and then a semi-silanized glass slide was placed on PDMS to let the excess of PDMS to be squeezed out of the mold (Figure 6-5, step 1). While keeping the pressure one the glass slide, the PDMS thin layer was cured at 80°C for two hours (Figure 6-5, step 2). Afterwards the semi-silanized glass slide along with PDMS thin layer can be easily peeled off from the mold as the mold was already fully silanized (Figure 6-5, step 3). Figure 6-5-c shows the bonding of two thin layers for form a closed microchannel.

The fabricated cover layer and  $\mu$ F-structure layer are shown in Figure 6-6 and Figure 6-7 respectively.

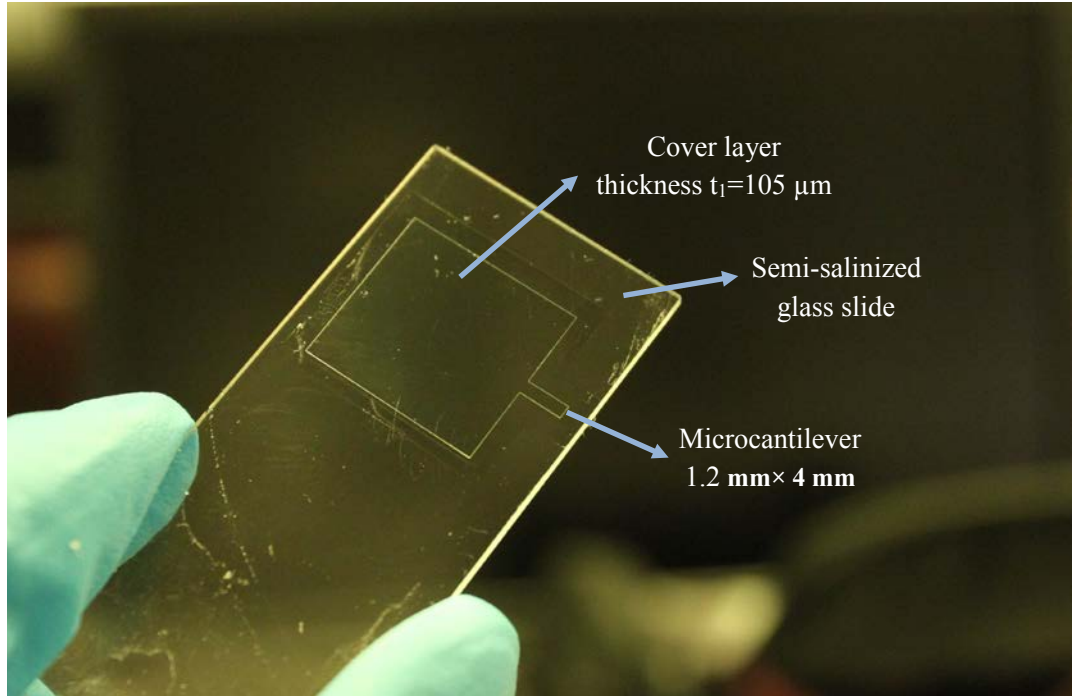


Figure 6-6: Cover layer of the cantilever on a semi-salinized glass slide.

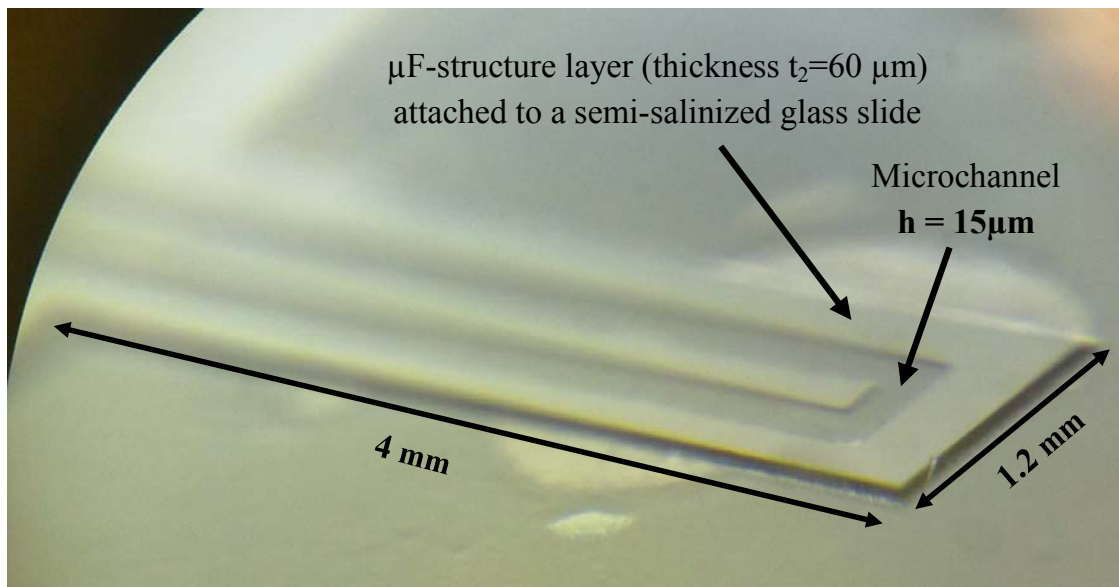


Figure 6-7: Fabricated  $\mu$ F-structure layer with the microchannel features on a semi-salinized glass slide. The buried microchannel with the depth of  $15 \mu\text{m}$  is clear in the image.

After the fabrication of all four layers, in order to fabricate the SPMF, first the top substrate was bonded to the cover layer by using oxygen plasma. Then the bonded top substrate carrying cover layer can be removed from the semi-silanized glass. Then the  $\mu$ F-structure layer was bonded to the cover layer and then the whole cantilever was removed from the other semi-silanized glass. Finally, the bottom substrate was bonded (using oxygen plasma) to have the whole PDMS cantilever.

One important issue in the fabrication of the cantilever is the correct alignment of the cover layer and  $\mu$ F-structure layer before PDMS-PDMS bonding. Any miss-alignment in the bonding process will result in the malfunctioning of the microfluidic system. All the process should be performed under an optical microscope.

A complete fabricated SPMF is shown in Figure 6-8. The size of the fabricated cantilever used in this work is 1.2 mm width by 4 mm long. The thickness of cover layer in this image is  $t_1=105 \mu\text{m}$  and the thickness of  $\mu$ F-structure layer is  $t_2=60 \mu\text{m}$  therefore the thickness of the whole microcantilever is  $165 \mu\text{m}$ .

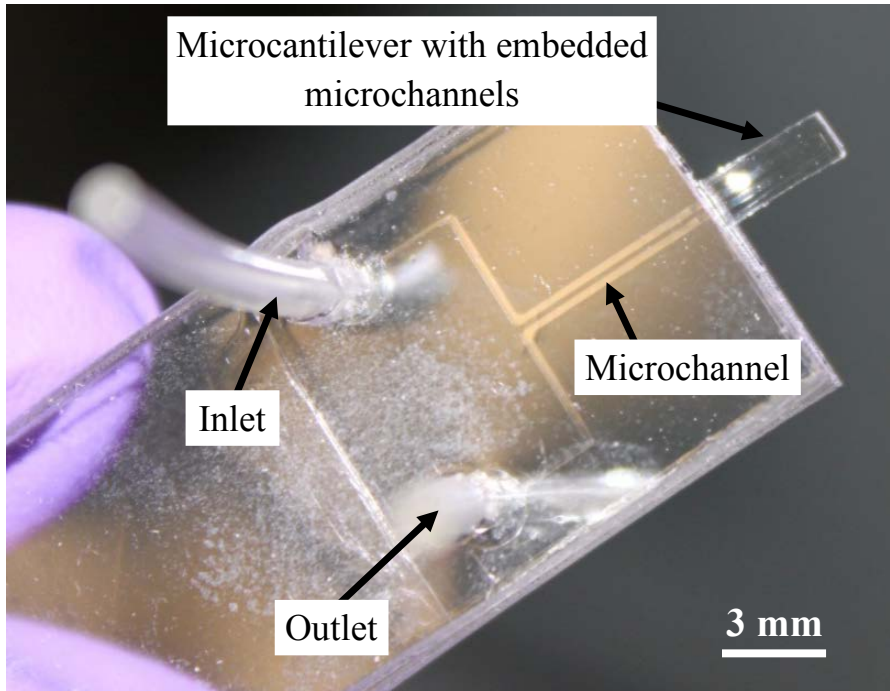


Figure 6-8: Fabricated PDMS-microcantilever with buried microchannels. The thickness of cantilever is 165  $\mu\text{m}$ .

### 6.3 Snapping problem

During the fabrication of the SPMF, some issues should be considered due to the bonding limitations. One of the steps in the fabrication procedure of SPMF is the plasma bonding of thin layers. Our results show that when the thickness of the cover layer is very low, upon its bonding with the  $\mu\text{F}$ -structure layer, the channels in the cantilever will be blocked due to snapping of the top layer into the bottom layer. This closure of the channel due to very high tension of activated PDMS surfaces (plasma activated) from both sides which causes the surfaces to attract and stick to each other. It results in blockage of the microfluidic channel. This phenomenon is shown schematically in Figure 6-9-a and a real snapping problem shown in Figure 6-9-b.

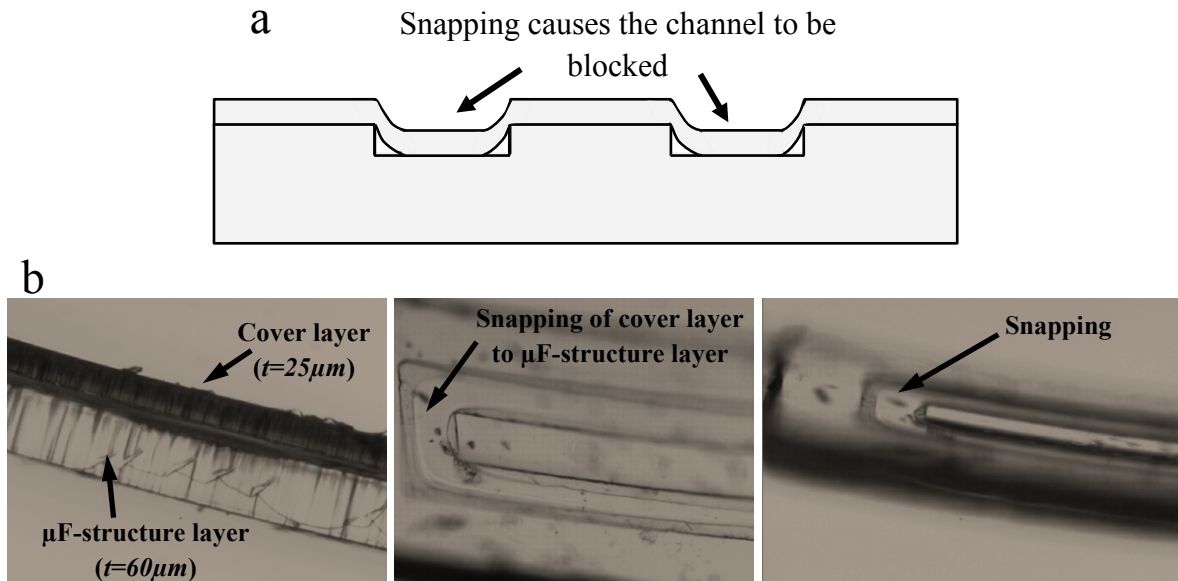


Figure 6-9: (a) Schematics of closure of the microchannel due to snapping problem of two thin layers; (b) the fabricated device while two layers are snapped.

Our fabrication results show that the cover layer with the thicknesses less than  $t_1 = 40 \mu\text{m}$  will result in the snapping of the channel. Therefore it can be concluded that the thickness of cover layer should be selected higher than  $40 \mu\text{m}$  ( $t_1 > 40 \mu\text{m}$ ) in order to avoid the snapping problem.

It should be noted that the obtained threshold value of  $t_1 = 40 \mu\text{m}$  to avoid snapping is strongly dependent on the microchannel width and it will decrease when the channel width is decreased. As a result of the above snapping problem, a thickness range of  $t_1 = 15\text{-}40 \mu\text{m}$  cannot be selected for the fabrication of microcantilever.

## 6.4 Optimization of cantilever thickness

A schematic of a microcantilever and its cross-section are shown in Figure 6-10. Upon interaction of biomolecules that are immobilized in the buried microfluidic channel, a surface-stress will be induced. This surface-stress results in the bending of cantilever.

The stress away from the neutral axis is responsible for the cantilever deflection and its orientation, because stress causes forces which result in the bending moments with respect to the neutral axis. In the proposed microcantilever, the surface-stress is assumed to be induced inside the microchannels where are placed in the  $\mu$ F-structure layer with a fixed thickness of  $t_2=60 \mu\text{m}$ . Therefore, the thickness of the cantilever cover layer, parameter  $t_1$  in Figure 6-10, plays an important role in the location of the neutral line. Indeed, changing the thickness of this top layer can result in the displacement of the neutral line. For a known induced surface-stress, the parameter  $d$  (Figure 6-10), the distance between the neutral line and the microchannel's center line, determines the cantilever deflection. The variation of parameter,  $d$ , against the change in the thickness of cantilever top layer,  $t_1$ , is shown in Figure 6-11 and is stated by the Equation 6-1.

Upon increasing  $t_1$ , first  $d$  decreases linearly and reaches to  $d=0$  (at  $t_1=45 \mu\text{m}$ ). Then it increases linearly as a function of  $t_1$ . The parameter  $d$ , can be obtained from the geometrical data shown in Figure 6-10, and can be calculated mathematically as following:

$$\begin{cases} d = \left(\frac{t_1+t_2}{2}\right) - \left(t_1 + \frac{h}{2}\right) & t_1 < t_2 - h \\ d = 0 & t_1 = t_2 - h \\ d = \left(t_1 + \frac{h}{2}\right) - \left(\frac{t_1+t_2}{2}\right) & t_1 > t_2 - h \end{cases} \quad (6-1)$$

Where  $t_1$  is the thickness of cover layer,  $t_2=60\mu\text{m}$  is the thickness of  $\mu\text{F}$ -structure layer, and  $h=15\mu\text{m}$  is the depth of the buried microchannel.

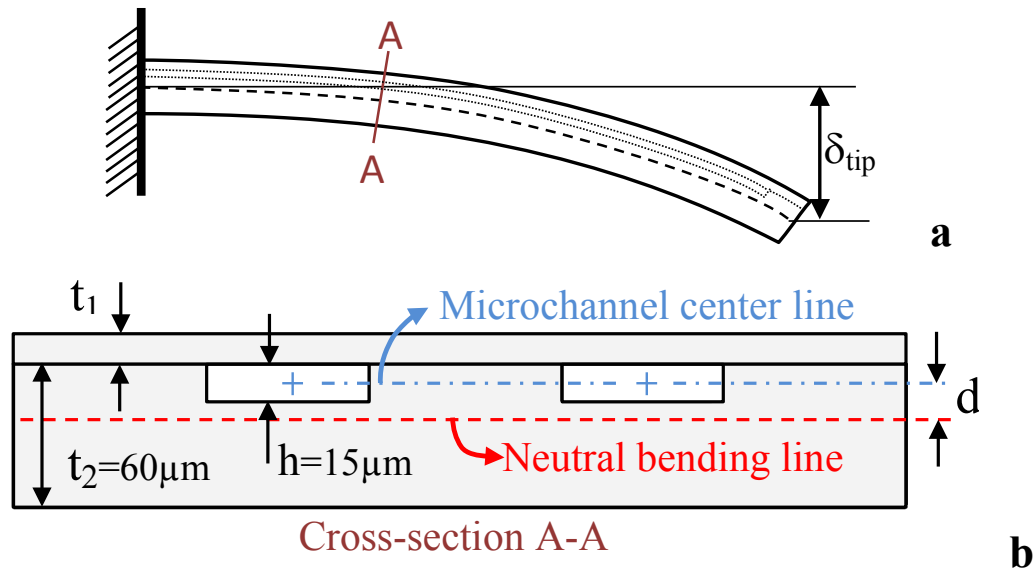


Figure 6-10: Schematic of the SPMF cantilever and its dimension, (a) cantilever subjected to bending; (b) cross section of the cantilever.

The variation of  $d$  against  $t_1$  is shown in Figure 6-11. As seen in this graph, there is a condition when  $t_1=45\mu\text{m}$ , the value of  $d=0$ , which means the center of microchannel is placed at the cantilever neutral line. In this condition, the induced surface-stress can result only the elongation of the cantilever with no bending and therefore  $\delta_{tip}=0$  which is not suitable for biosensing. Indeed, the best choice is to select the parameter  $d$  as maximum as possible in order to maximize the cantilever deflection due to bending. On

the other hand, the increase of  $d$ , increase the stiffness of the cantilever correspondingly resulting in decrease in bending of the cantilever.

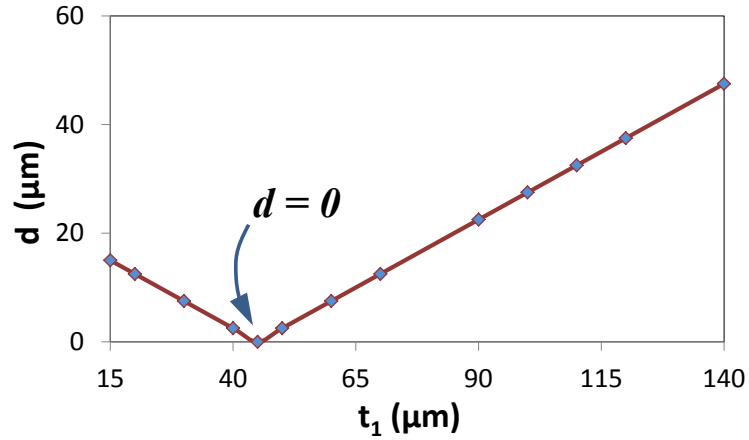


Figure 6-11: The variation of parameter  $d$  with respect to the thickness of cantilever cover layer  $t_1$ .

#### 6.4.1 Finite Element Modeling

To find the optimum value of  $t_1$ , the deflection of cantilever under a known induced surface-stress was modeled. The COMSOL® Multiphysics MEMS module is used for the finite element (FE) analysis of Euler-Bernoulli equation. One can also use the Stoney's formula to calculate the cantilever tip deflection. The FE results and those obtained by using Stoney equation would be very close but not exactly similar due to presence of a buried microchannel in the cantilever. For simulation, FEM of the 3D CAD model is used for simulation. The whole 3D volume is discretized with the maximum element size of  $10\mu\text{m}$ . Figure 6-12 shows the FEM model of the cantilever and the boundary condition that was used for the simulation.

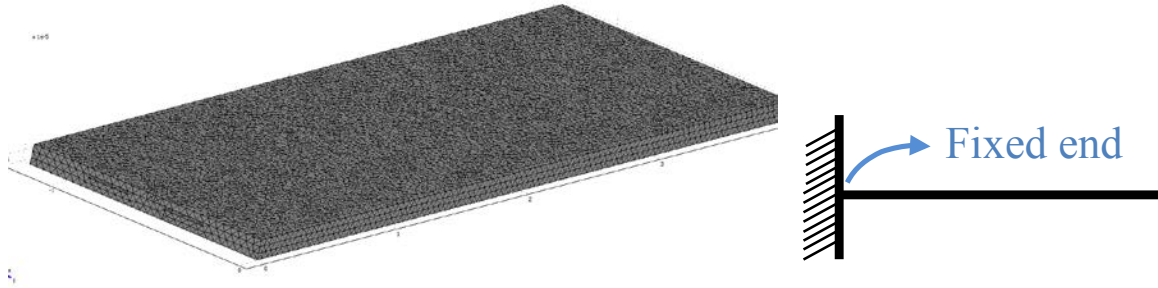


Figure 6-12: FEM model of the microcantilever and its boundary condition

The Euler-Bernoulli equation describes the relationship between the beam's deflection and the applied load as following:

$$\frac{d^2}{dx^2} \left( EI \frac{d^2 w}{dx^2} \right) = q \quad (6-2)$$

Where  $w(x)$  describes the deflection of the beam in the  $z$  direction (vertical beam deflection) at position  $x$ ,  $q$  is a distributed load, in force per unit length.  $E$  is the elastic modulus and  $I$  is the area moment of inertia.  $I$  must be calculated with respect to the centroidal axis perpendicular to the applied loading. For an Euler-Bernoulli beam not under any axial loading,  $EI$  is a constant, so the Equation 6-2 can be simply rewritten as:

$$EI \frac{d^4 w}{dx^4} = q(x) \quad (6-2)$$

The mechanical properties of PDMS were used in the analysis. However it should be noted that it has been showed that both the mechanical strength and the Young's modulus of the PDMS membranes are thickness dependent. In particular, for the PDMS membrane with a thickness of less than 200  $\mu\text{m}$ , there is a high non-linearity between the mechanical properties and thickness of the membrane [159]. We have implemented these

thickness dependent properties in the FE simulation. The values of these properties were taken from a work published recently by Liu et al [159]. This non-linear relationship between the modulus of elasticity and the thickness of PDMS membrane is shown in Figure 6-13.

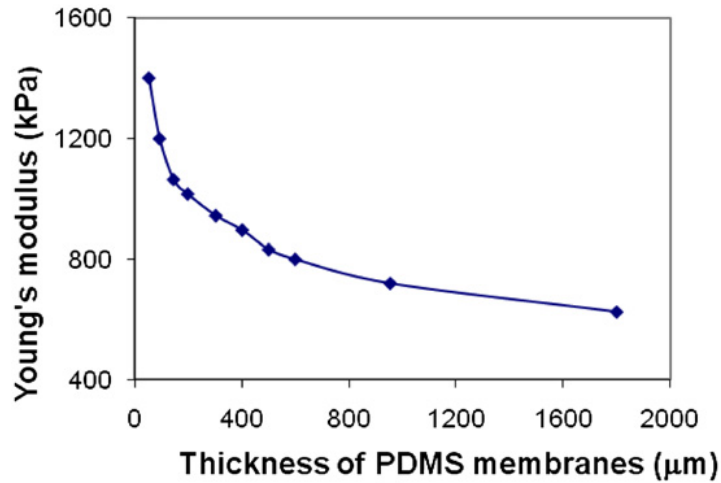


Figure 6-13: Variation of elastic module of PDMS membrane against thickness [159].

Following values used for the simulation:  $\rho=0.97 \text{ gr/cm}^3$ ,  $\nu=0.5$  (Poisson ratio), and the magnitude of the surface-stress induced by biomolecular interaction  $\sigma = 5 \text{ mNm}^{-1}$  from a work done by Fritz et al [4]. Though we do not have the exact value of the stress induced by bST antigen/antibody interaction, the value of this stress is not the main issue as there is a linear relation between the  $\delta_{tip}$  and  $\sigma$ . A simulated cantilever with the real dimensions and its deflection is shown in Figure 6-14. In this figure the deflection of cantilever is normalized while the blue color shows zero deflection, the red color corresponds to the maximum deflection of 1.

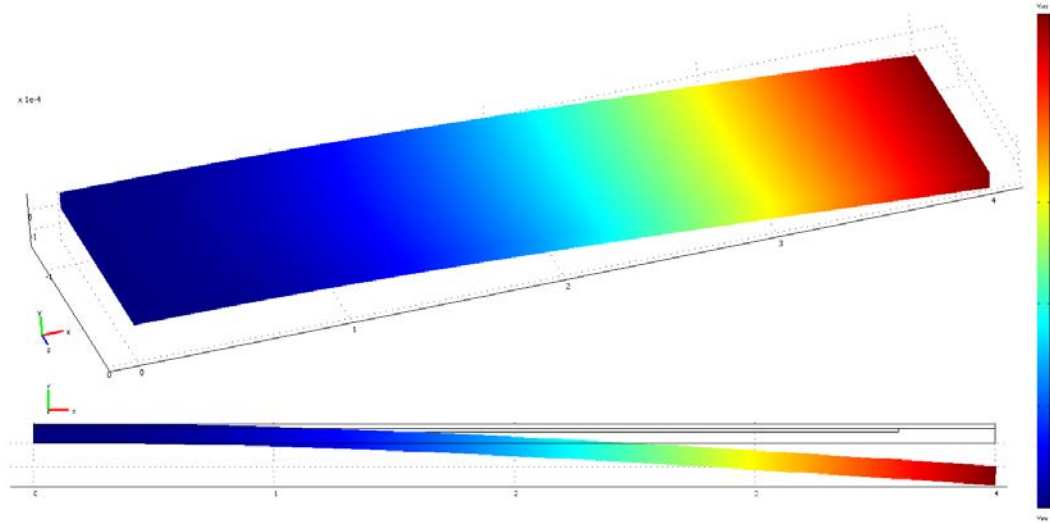


Figure 6-14: Simulation of a microcantilever with buried microchannel. A surface stress of  $\sigma = 5 \text{ mNm}^{-1}$  is applied on the surface of the channel walls.

The cantilever with different top layer thicknesses was simulated. For each case the value of Young's modulus of the PDMS was selected based on the thickness of the cantilever (from Figure 6-13). The normalized tip deflection against the thickness of top cantilever layer was plotted in Figure 6-15. From this graph it can be seen that for a low thickness of  $t = 15 \mu\text{m}$  top layer, we have the maximum deflection. By increasing the thickness, the deflection will be decreased as a result of reducing of the parameter  $d$ . By approaching to  $d = 0$ , the deflection will approach to zero. Upon further increasing of  $t_1$ , the deflection will first increase and then will decrease. The increase is due to increasing of parameter  $d$ , however, by more increasing of the thickness, the stiffness of the cantilever will increase which results in decreasing of the cantilever deflection. Therefore, from this figure, it can be inferred that the optimized thickness of the top layer can be either in the range of  $t_1 = 15\text{-}40 \mu\text{m}$  or  $t_1 = 80\text{-}130 \mu\text{m}$ .

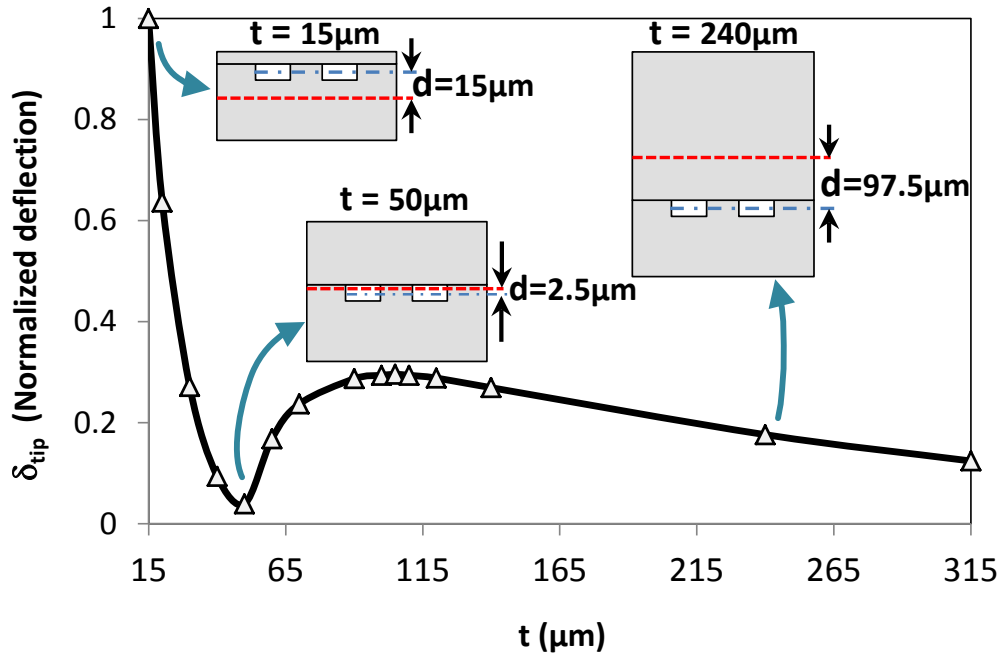


Figure 6-15: optimization of the thickness of cantilever top layer for achieving the highest tip deflection.

However, it has been observed that any thicknesses less than 40  $\mu\text{m}$  will result in closure of the microchannel in the cantilever due to the snapping problem in the bonding step. Hence, the only possible range for the fabrication of microcantilever is  $t_l=80\text{-}130 \mu\text{m}$  which would result in maximum cantilever deflection.

## 6.5 Conclusion

In this chapter, the realization of a PDMS microcantilever with buried microchannel called “*suspended PDMS microfluidic (SPMF)*” is presented. The cantilever was fabricated by using two SU-8 molds which form two thin layers of the cantilever. The cantilever was simulated to find the optimum range for the maximum deflection with respect to the cantilever cover layer. The fabrication shows any thickness less than 40  $\mu\text{m}$  will result in the closure of the cantilever channels due to snapping of the PDMS thin

layers during the plasma bonding. Therefore the optimum range for the cantilever top layer was optioned to be  $t_1=80-130 \mu m$ . The fabricated cantilever with optimum dimensions has a length of 4 mm, width of 1.2 mm and thickness of 165  $\mu m$ . the width of the buried channel is selected to be 200  $\mu m$  with the depth of 15  $\mu m$ .

## **Chapter 7: Hybrid Synthesis and Integration of gold nanoparticles (AuNPs) on Suspended PDMS- Microfluidics**

Integration of gold nanoparticles on the surface of PDMS-microfluidics for biosensing applications is a challenging task. In this chapter we address this issue by integration of pre-synthesized gold nanoparticles (AuNP) solution in a microfluidics. This method explored the affinity of AuNPs toward PDMS surface so that, the particles will be *adsorbed* onto the channel walls. AuNPs were synthesized inside a microreactor before integration. In order to improve the size uniformity of synthesized AuNPs, a micromixer which was proposed earlier in this thesis (Chapter 4), was integrated with the microreactor for providing full mixing. The method of integration of AuNPs in the SPMF is presented in this chapter. The fabrication of suspended PDMS-microfluidics (SPMF) cantilever is discussed in detail in the previous chapter (Chapter 6). Finally the integrated biosensing platform was used for the detection of antigen-antibody interaction.

### **7.1 Introduction**

The development of immunosensors that uses gold nanoparticles is increasing explosively in the recent years [136]. The interest in the AuNP-based biosensors relies on their unique properties allowing label-free and real-time biomolecular analysis with possible detection of biomolecular interactions at low-concentrations [137]. Specifically, integration of AuNPs in PDMS microfluidic chips opens new opportunities for the development of ultra-sensitive biosensors [65]. It is well-established how to immobilize biomolecules (proteins, polypeptides, antigens and antibodies) on the gold nanoparticle

through appropriate functionalization of the particle [63]. The immobilized molecules enable researchers to locally observe and study the behavior of the biomolecular interactions.

Several works on the integration of nanoparticles into the microfluidic devices for biosensing application have recently been published [142,143]. There are two main approaches to integrate AuNPs into a microfluidic system: (1) by using AuNPs that were pre-synthesized outside and then introducing them into the microfluidic system [145,146,148] and (2) by using an *in-situ* method to synthesize AuNPs in the main sensing microfluidics [151].

In this work, for the integration of gold nanoparticles on the surface of PDMS, AuNPs are synthesized in a hybrid integrated microreactor. For the synthesis purpose, aqueous solutions of gold precursor and reductant are mixed in the microreactor. Upon mixing the analytes, the gold ions in the solution are reduced to nanoparticles. This process results in the preparation of gold nanoparticle red solution. Performing the synthesis process in microfluidic environment has several advantageous compared with macro-synthesize. Due to large surface area to volume ratio, heat and mass transport are considerably enhanced which leads to better uniformity of particles in terms of size distribution [108,138]. However, one drawback in microfluidic synthesis is insufficient mixing. A micromixer may be integrated with a microreactor to resolve this issue [119,152]. After preparation of AuNPs, it is introduced into a microchannel and the particles will be immobilized on the PDMS surface upon suitable surface treatment such as plasma activation of PDMS surface which is used in this work [160]. The integrated

(immobilized) particles inside a microfluidics provide a proper sensing platform for wide range of biosensing applications.

In clinical diagnostics a challenging task that is highly demanding is to obtain high sensitivity platform in short period of time [1]. Mechanical transducers-cantilever biosensors have a simple sensing mechanism with high sensitivity which makes them useful for clinical applications. Many research groups are focusing on these types of biosensor platforms in the last decade. This is due to their simple transduction mechanism as they can simply translate biomolecule interactions into a measurable signal. Particularly, in microcantilever biosensors, the biomolecular interaction such as antigen/antibody interaction, take place on the cantilever surface [38]. The biomolecular interaction induces a surface stress which results in the cantilever bending [2,26,27]. In the previous chapter, a polymeric cantilever with buried channel was fabricated (SPMF). In order to use this cantilever as a platform for biosensing application, a method to integrate AuNP homogenously on the PDMS surface of microfluidic is critical. The integrated particles, allow us to immobilize different biomolecules on the surface of AuNPs in order to use the SPMF device for different biosensing applications.

This chapter addresses this issue by reporting a method for the integration of AuNPs on the surface of the PDMS microfluidic sensing platform. Here, the AuNPs are first synthesized in a microreactor with is connected to a micromixer. The synthesized AuNPs then were introduced into the SPMF and allowed to be immobilized and integrated on the PDMS microfluidics (SPMF). The AuNP integrated SPMF platform was then used as a biosensor for the detection of bovine growth hormone.

## **7.2 Material and methods**

### ***7.2.1 Materials***

Dow Corning Corporation's PDMS Sylgard® 184 elastomer kit was used. SU-8 from MicroChem and Gold chloride trihydrate ( $\text{HAuCl}_4 \cdot 3\text{H}_2\text{O}$ ) from Alfa Aesar were purchased. 1-pentanol, toluene, 2-propanol ethyl alcohol, and N, N-dimethylformamid, bought from Sigma-Aldrich was used in the experimental work. Mmonoclonal Bovine Growth Hormone antibody (anti-BGH or bST) in mouse and Bovine Growth Hormone (BGH) antigen were supplied from Dr. Parlow National Hormone and Peptide Program in California, USA. Furthermore, from Sigma Aldrich we purchased Nanothink® 18, TWEEN® 20, N-Hydroxysuccinimide (NHS), and N-(3-Dimethylaminopropyl)-N'-ethylcarbodiimide hydrochloride (EDC).

### ***7.2.2 Fabrication of microreactor***

Standard SU-8 process was used to fabricate a mold for the fabrication of a microreactor. The fabrication steps are schematically shown in Figure 7-1-A. For the mold fabrication, SU-8 was spin coated at 1500rpm for 30s on a cleaned wafer and then soft-baked at 95°C for 15 min. The soft-backed SU-8 was exposed to UV followed by a post-baking process. The SU-8 was then developed. The mold was silanized to enable remove of PDMS chip from the mold after curing.

PDMS compound was prepared by mixing PDMS and its curing agent (by weight ratio 10:1). The fabrication is followed by degasifying the mixture. The mixture is then poured

into the SU-8 mold and the mold is kept in oven at 70°C for curing for a minimum 4 hours. The cured molded PDMS is peeled off from the mold as shown in a Figure 7-1-1. A flat PDMS layer (Figure 7-1-2), was then bonded with the microreactor layer (Figure 7-1-1) by using oxygen plasma treatment. A fabricated microreactor is shown in Figure 7-1-B.

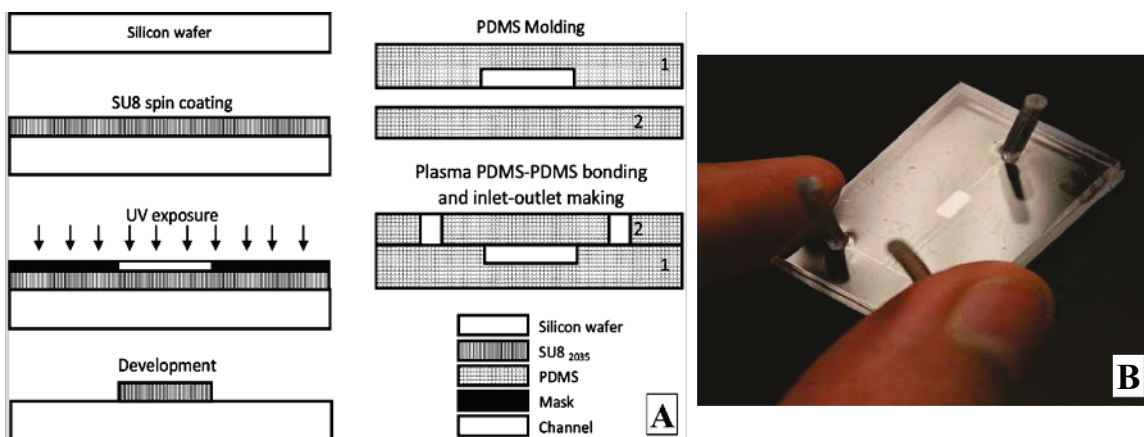


Figure 7-1: (A) Fabrication steps of a PDMS microreactor for the synthesis of gold nanoparticles; (B) fabricated PDMS-microreactor chip of size 2 mm×4 mm.

### 7.2.3 Synthesis of AuNPs in a microfluidic environment

One method of preparing of gold-PDMS nanocomposite is to introduce the pre-synthesized AuNPs into the microchannel and allow them to be embedded on the surface. In this procedure, the particles will be integrated onto the channel wall as a result of their affinity of the particles toward the polymer. This affinity is as the result of plasma activation of the PDMS surface in the chip fabrication stage which is discussed in detail in [160].

In general, AuNPs are synthesized in a macro-scale environment (in batch). The main advantage of this type of reduction reaction is the complete mixing of the gold precursor

(gold salt) and the reductant (sodium citrate). However, as it has been already mentioned, miniaturization of the reaction platforms provides new opportunities for advanced synthesis [108,138] properties. In microreactors, due to enhanced heat and mass transportation, the quality of the produced particles is generally improved in terms of size distribution [65]. In this work, we used a microreactor for the AuNP synthesis. A schematic of the synthesis in a microreactor is shown in Figure 7-2.

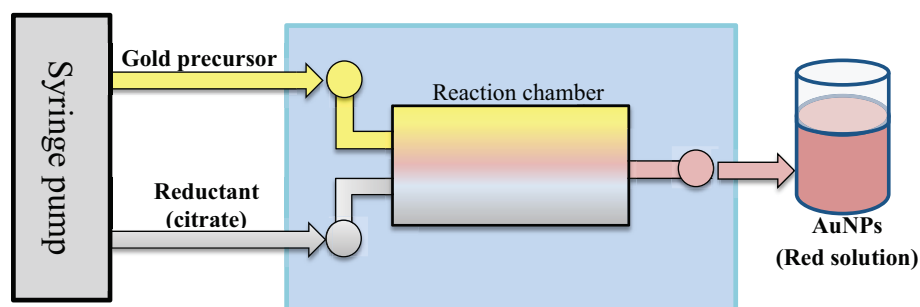


Figure 7-2: Schematic of synthesis of AuNPs in a microreactor.

A syringe pump was used to pump chloroauric acid (gold precursor) and sodium citrate (reductant) with the flow rate of  $10\mu\text{l}/\text{min}$  into the microreactor as shown in Figure 7-3. The output was collected (the close-up image) to characterize the AuNP solution.

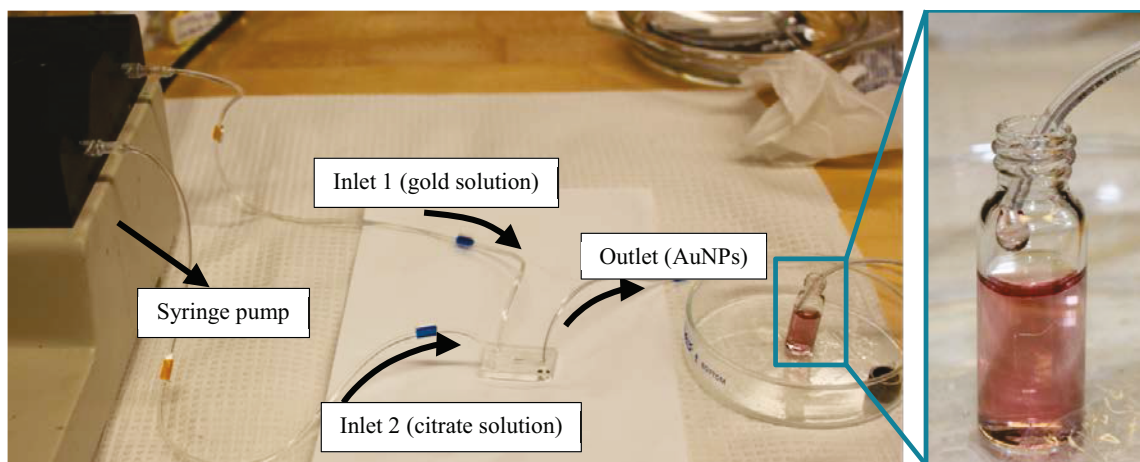


Figure 7-3: Synthesis of gold nanoparticles in a microreactor.

Upon synthesis of AuNPs in the microreactor, particles will be adsorbed onto the PDMS surface to form gold-PDMS nanocomposite. As we mentioned earlier, one of the main concerns in the microfluidic synthesis is insufficient mixing. Indeed, incomplete mixing causes AuNPs to be obtained only at the contact area of the two analytes where mixing is happening as it shown in Figure 7-4. In this figure, the close-up shows that the AuNPs are integrated on the PDMS surface along the center line of the channel which shows incomplete mixing of fluids. In order to improve the mixing for complete reaction, the 3D-micromixer, discussed in Chapter 4 of this thesis, was integrated with microreactor.

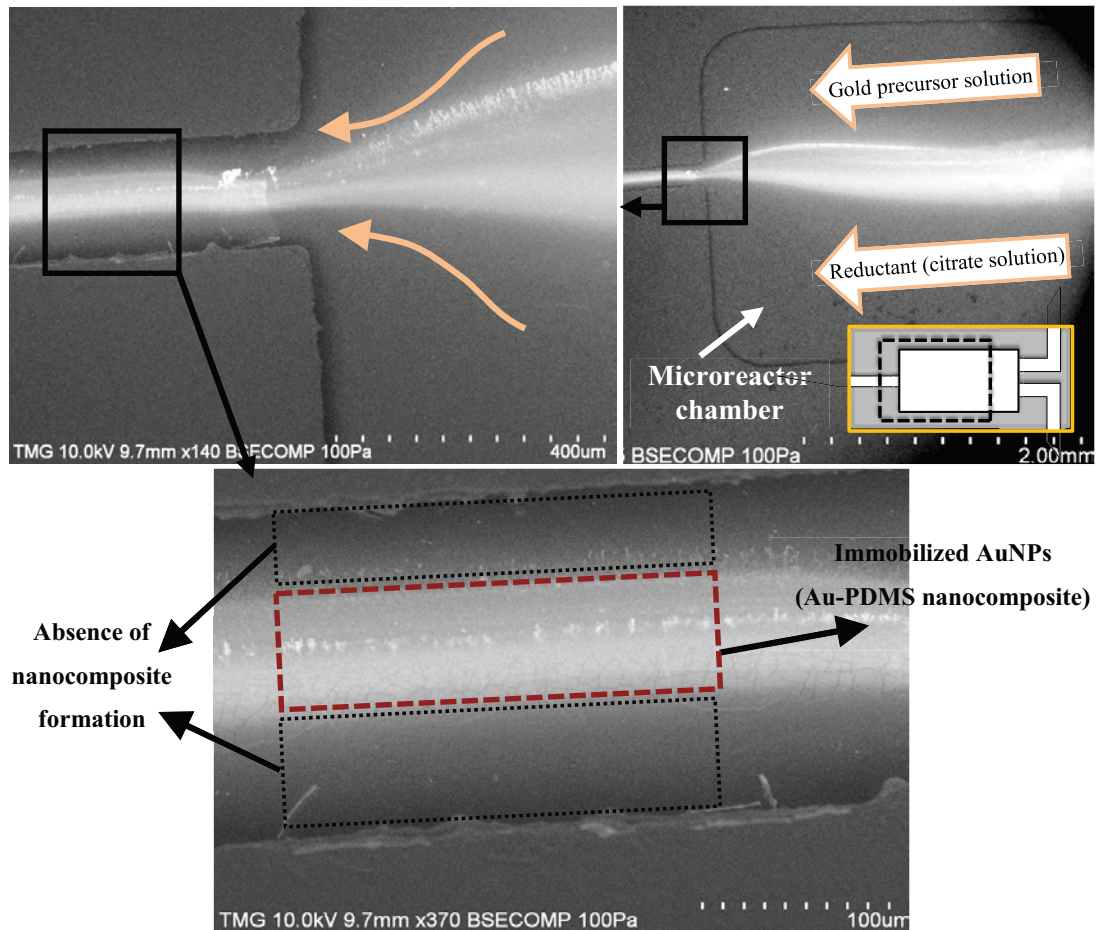


Figure 7-4: Formation of gold nanoparticles in a microfluidic reactor and immediate adsorption of synthesized AuNPs onto the PDMS microchannel surface. The micrographs show that the insufficient mixing causes the nanocomposite to form only in the contact area of two analytes.

#### ***7.2.4 Integration of 3D-micromixer with microreactor***

As mentioned earlier in this thesis, a 3D-PDMS micromixer was designed, fabricated and successfully tested [67]. The mixing mechanism is based on split-and-recombinant flows and is discussed in detail in Chapter 4.

The micromixer was integrated to the microreactor and the output was connected into the suspended PDMS microfluidics (SPMF). Through this layout, AuNPs are allowed to be immobilized onto the surface of PDMS of buried microchannel. The sensing platform will be further used for the detection of biomolecular interaction. The schematic of the integrated platform and the fabricated device are shown in Figure 7-5-a and b, respectively.

In the absence of a micromixer, in the previous part, it was observed the formation of gold only along the center-line of the channel. However, upon integration of the microreactor with micromixer, our results show the immobilization (adsorption) of gold nanoparticles on the whole cross-section of the outlet channel. SEM images of the channel walls are obtained and showed in Figure 7-5-c. This SEM shows the integrated AuNPs on the surface of PDMS of channel walls.

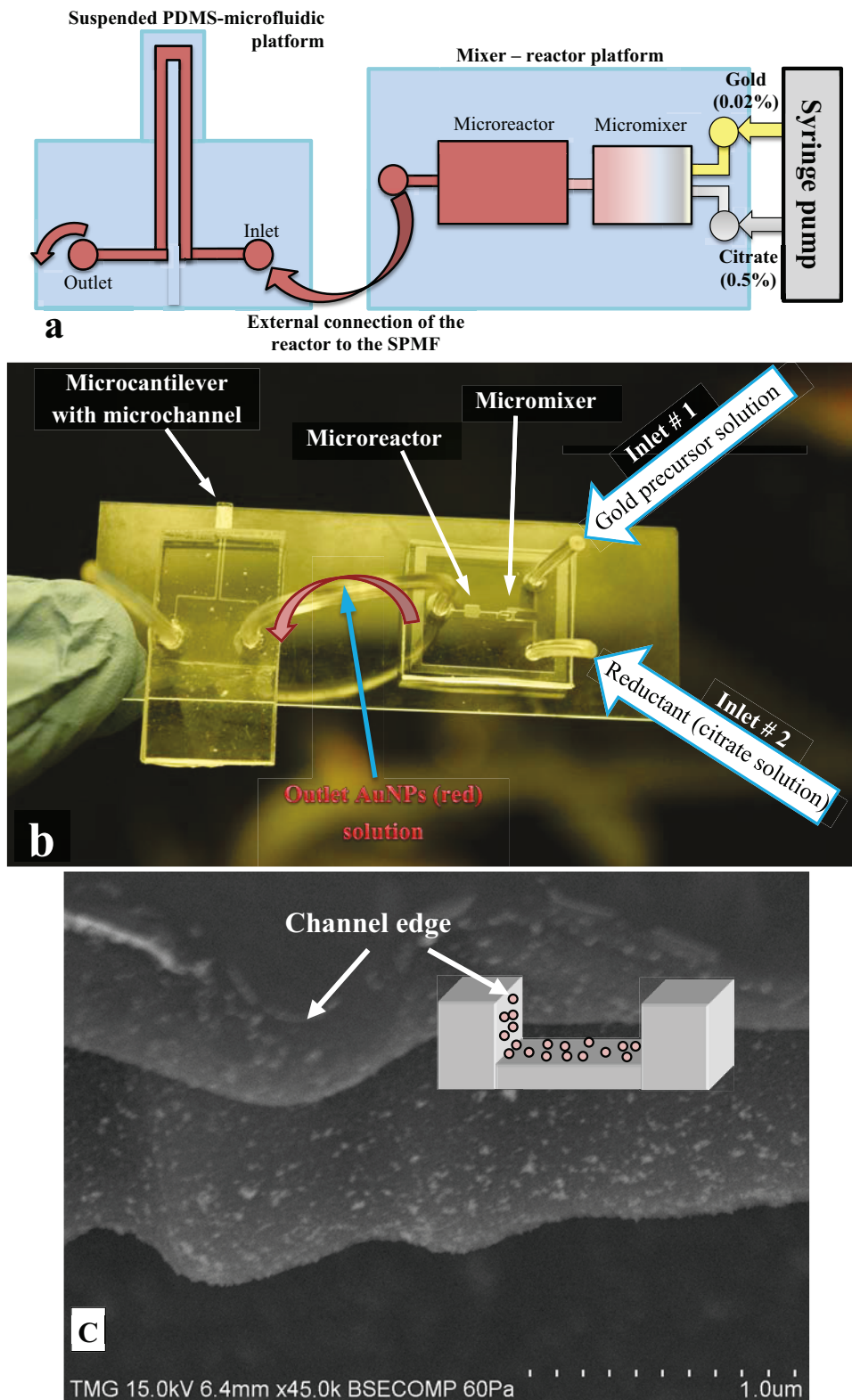


Figure 7-5: Introduction of pre-synthesized AuNPs into the SPMF; (a) Schematic of the integrated micromixer-microreactor-biosensor platform; and (b) The fabricated device (c) SEM image of the microreactor outlet channel wall.

Different concentrations of gold precursor (0.005%, 0.01%, 0.02%, 0.05%, and 0.1%) and sodium citrate solution (0.2%, 0.4%, 0.5%, 0.8% and 1%) were used to obtain the optimum conditions for preparation of the nanocomposite while the inlets' flow rate was kept at a constant flow rate of 10 $\mu$ l/min. SEM images of the PDMS-nanocomposite were obtained in each case. It should be noted as we mentioned earlier in Chapter 2, gold salt solution with the concentration less than 0.25% will not result in the formation of AuNP through the in-situ process. Therefore the concentrations of gold in this chapter are selected much less than this limit to minimize the formation of AuNPs by *in-situ* process.

In addition, based on our previous experiments, the AuNP integrated SPMF platforms were annealed to improve the size distribution of NPs. For heat treatment, the device has been heated from room temperature to 300 $^{\circ}$ C in 10 minutes and then kept at this temperature for 30 min.

### ***7.2.5 Biosensing protocol and experiment***

The bST antibody (Ab) (anti-BGH) and its corresponding antigen (Ag) were used for biosensing experiments using the annealed devices.

Functionalization of AuNPs with 5mM ethanol solution of 11-mercaptoundecanoic acid (NanoThink $^{\circledR}$  ACID11) is the first step of biosensing protocol. The solution was introduced into the SPMF and kept for 5 h. After that, in order to activate the carboxyl groups, the conventional carbodiimide coupling chemistry (EDC/NHS) is used. This step was carried out by injecting a 1:1 ratio mixture of 0.4M N-(3-dimethylaminopropyl)-N'-ethylcarbodiimide hydrochloride (EDC) and 0.1M N-hydroxysuccinimide (NHS) for 1 h.

Upon activation of AuNPs, Ab can be immobilized on the gold nanoparticles. 200ng/ml antibody dissolved in a PBS buffer solution was introduced into the SPMF for 8 h. The procedure was followed by washing the SPMF several times with a 0.05% TWEEN® 20 solution in PBS. All these steps were carried out by introducing the corresponding analyte using a syringe. The last step is introducing the solution of Ag in PBS into the microchannel by using a syringe pump at a flow rate of 10  $\mu\text{l}/\text{min}$ . The syringe pump introduced the Ag solution for 60 second to make sure the microfluidic channels are full of the solution. Upon interaction of Ag-Ab, the cantilever bends due to the induced surface-stress. The deflection of cantilever was measured by using an optical microscope. The schematic of the deflection measurement setup is shown in Figure 7-6.

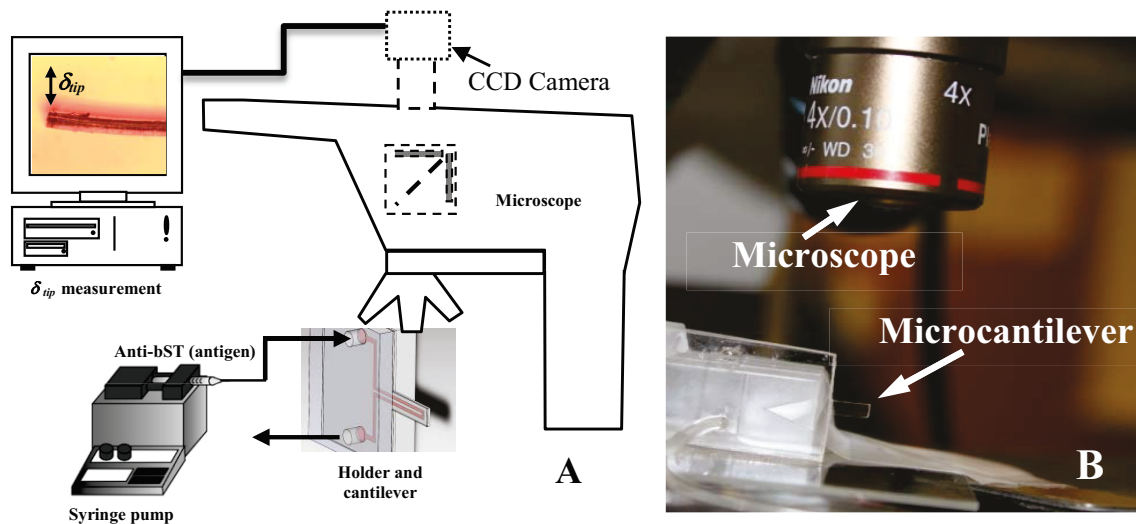


Figure 7-6: Deflection measurement of the cantilever (a) Schematic of the experimental setup; (b) Device under test (DUT) in an experiment

As we already mentioned in the introductory part, the interaction of antigen with antibody will induce a surface stress in the microchannel which will results in bending of the cantilever. The whole biosensing experiments were performed under an optical

microscope to track the cantilever tip as schematically shown in Figure 7-6. The tip deflection was calculated from the analysis of microscope images. Different antigen concentrations were tested to estimate the detection limit of the proposed cantilever biosensor considering a minimum detectable tip deflection of  $1\mu\text{m}$ . A cross section of the microchannel with AuNPs immobilized on PDMS is shown in Figure 7-7-a. In Figure 7-7-b, four steps of the biosensing protocol are shown schematically. Figure 7-7-d shows cantilever bending due to the interaction of biomolecules.

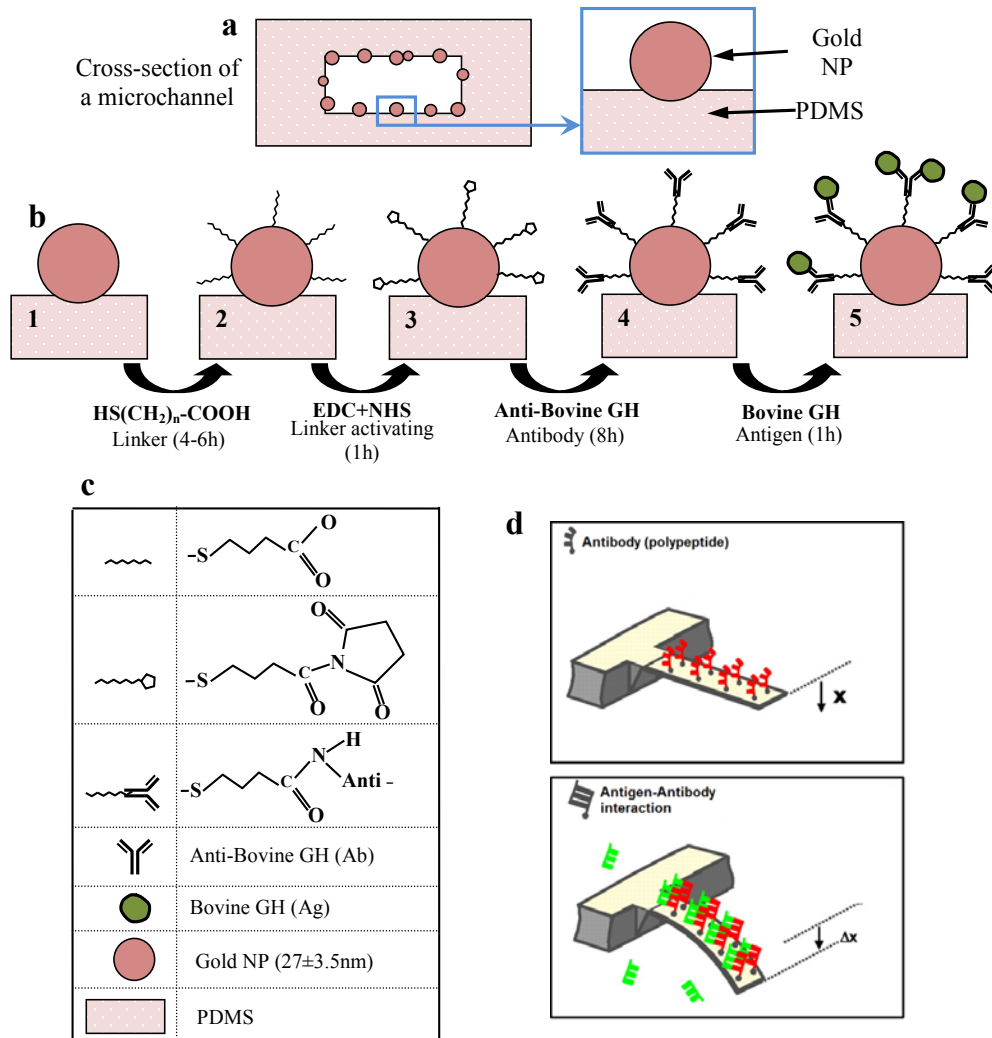


Figure 7-7: (a) A cross section of the microchannel and the position of AuNPs; (b) biosensing protocol; (c) legend of the figure; (d) schematic of the deflection of cantilever tip upon interaction of antigen-antibody [34].

## 7.3 Results and discussions

### *7.3.1 Au-PDMS nanocomposite fabrication and SEM characterization*

SEM images of the nanocomposite were taken under different conditions. Gwyddion 2.28, a modular program for data visualization and analysis was used, to obtain the size distribution of particles from SEM images.

Experimental test were carried out under different concentrations of gold precursor and citrate solution to estimate the most suitable condition of nanocomposite preparation. The samples were then annealed to improve the size distribution. SEM images of the Au-PDMS nanocomposite were obtained from the microfluidics (the channel of SPMF) under different solution concentrations were recorded. In addition, the gold plasmon bands of the collected solution from the microfluidic chip were measured using a UV/Vis spectrophotometer (LAMBDA 650 UV/Vis Spectrophotometer from PerkinElmer).

Our results show that the optimized condition for the preparation of gold-PDMS nanocomposite is when a 0.02% aqueous solution of gold chloroauric acid (gold salt precursor) and 0.5% of aqueous solution of sodium citrate (reductant) were introduced into the microreactor in the room temperature. These conditions resulted in a narrow size distribution of synthesized AuNPs in a microfluidic channel with minimum aggregation of the AuNPs. Figure 7-8-a shows Au-LSPR spectra of the collected red solution for the optimum condition (0.02% of gold salt and 05% of citrate) and another mixing condition while the concentrations of the gold and reductant was 0.05% and 0.5% respectively. In

Figure 7-8-b and Figure 7-8-c, the SEM images of the nanocomposite for these conditions and their corresponding size distribution histogram are shown.

The Au-LSPR spectra of the collected gold nanoparticle solutions show that the spectrum in the optimum condition is narrower meaning narrow size distribution. Indeed, the size histogram graphs show the optimum condition resulted in a narrow size distribution of  $27 \text{ nm} \pm 3.5 \text{ nm}$  compared with the other condition with a wide size distribution of  $29 \text{ nm} \pm 7.5 \text{ nm}$ .

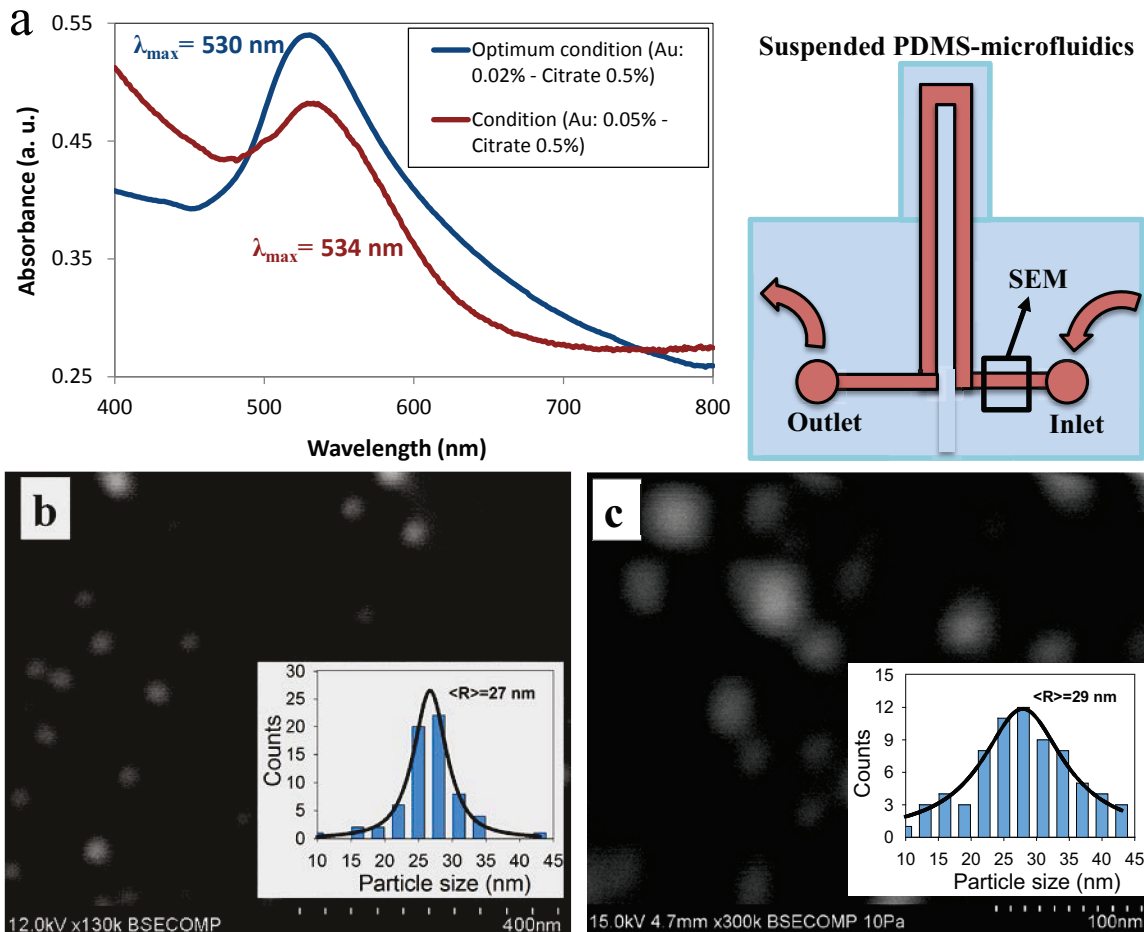


Figure 7-8: Au-LSPR spectra of the collected solution for two different concentrations and their corresponding SEM images

### 7.3.2 Static deflection of PDMS cantilever tip

As we mentioned in section 7.2.5, the images of the cantilever were used for deflection measurement. An important issue in the measurement of deflection is to justify that the cantilever tip is deflected as a result of an induced surface stress and not a simple cantilever movement. We prove this by showing that a part of the cantilever that is recorded undergoes bending. Figure 7-9 proves this issue by selecting two fixed points along the cantilever in each image. Then the angle of the line that passes through these two points was calculated. Changing of slope of this line is an evidence of bending of cantilever in the image. Generally we assume that the base of the cantilever is fixed and rigid.

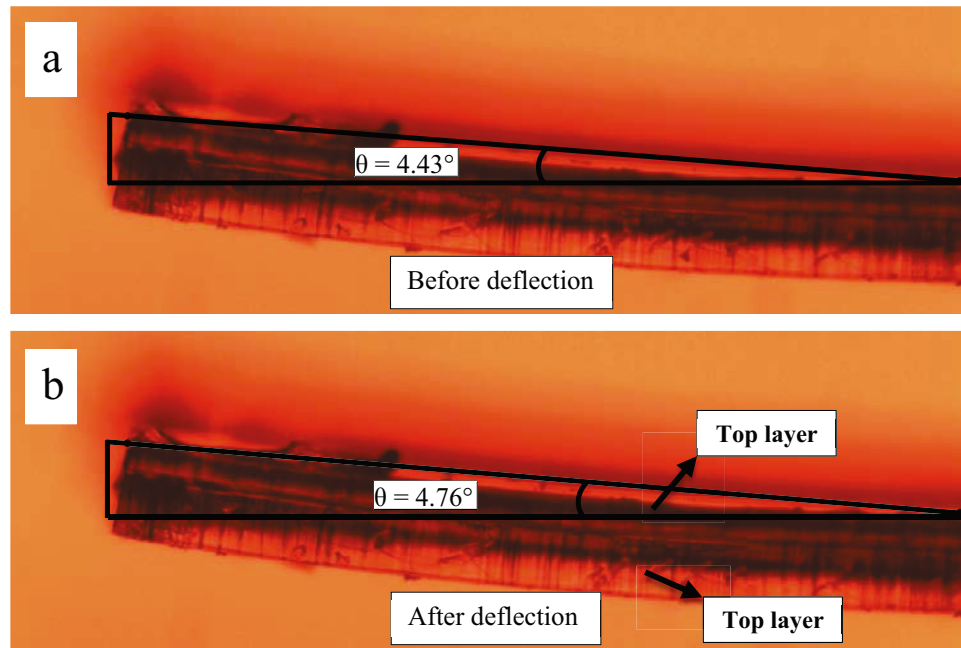


Figure 7-9: Calculation of the cantilever bending by measuring the slope of the cantilever deflection.

### ***7.3.3 Antigen-antibody interaction and determination of detection limit***

The biosensing experiments were performed on integrated SPMF with the cantilever of size of 1.2 mm width, 4 mm long and 165  $\mu\text{m}$  thick. At the final step of biosensing protocol, the antigen was injected into the buried microchannel and at the same time the deflection of the cantilever was recorded through a CCD camera connected to an optical microscope. The frequency of CCD imaging was set to be one image per second and deflection of the cantilever calculated in each image.

Figure 7-10 shows the response of the cantilever for 12 min during the last step of biosensing experiment which is the injection of anti-bovine growth hormone (Ag). At the beginning of the test before injection of Ag, the cantilever is at its static equilibrium with the tip deflection of zero. The antigen solution was injected into the SPMF at  $t=240 \text{ sec}$  (at the flow rate of 10  $\mu\text{l}/\text{min}$ ) and then the syringe-pump was turned off at  $t=300 \text{ sec}$ . These times are also marked in Figure 7-10-a. One important issue that is shown in Figure 7-10-b is the existence of three phases in the response of the cantilever during the biosensing experiments. The first phase is when the cantilever is at its static condition (with the deflection of  $\delta_{\text{tip}}=0$ ). The second phase starts at  $t=240 \text{ sec}$  when the Ag is injected into the microchannel via the pump. The transience phase lasts for around 80 sec when the cantilever reached to its steady-state response of 19  $\mu\text{m}$ . A permanent cantilever deflection of 19  $\mu\text{m}$  is obtained after the completion of Ag-Ab interaction.

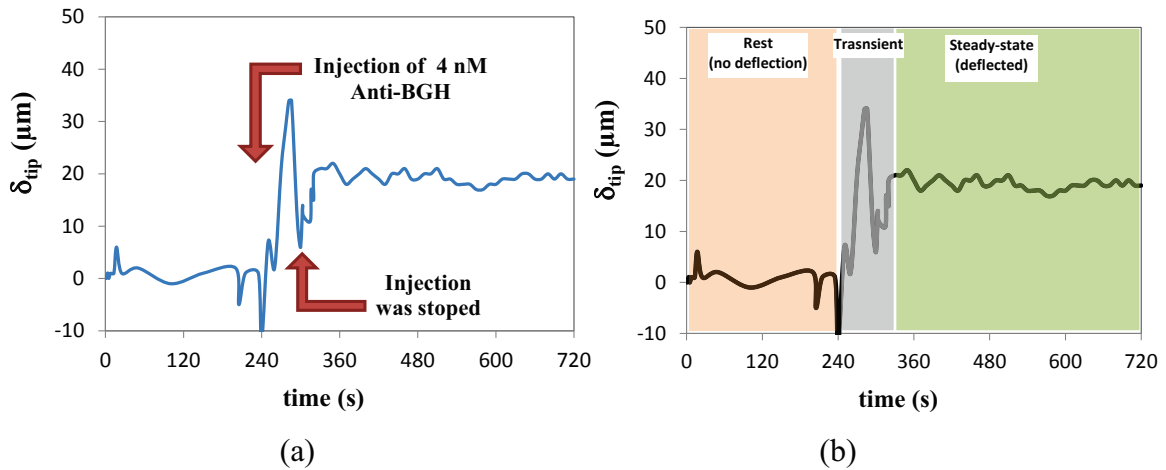


Figure 7-10: (a) Response of the cantilever for the Ag concentration of 4nM; (b) three phases of biosensing including: Before injection of Ag, during the stress induction, and the final response .

The steady-state deflection of the cantilever was obtained for three different concentrations of 80 ng/ml, 40 ng/ml and 10 ng/ml. After each biosensing experiments, the cantilever washed several times with 0.01% tween solution and DI water (around 10 times) and dried to remove the immobilized Ab and Ag. These results were used to obtain the limit of detection of the cantilever sensor as shown in Figure 7-11. The detection limit was found to be as low as 10ng/ml (500pM) by extrapolation of the line when crossing the 1 $\mu\text{m}$  error (minimum detectable deflection) in the deflection measurement of the cantilever. The horizontal error bars in this figure shows 4% error in the preparation of Ag solution in PBS and the vertical bars shows 1 $\mu\text{m}$  error in the measurement of cantilever tip deflection.

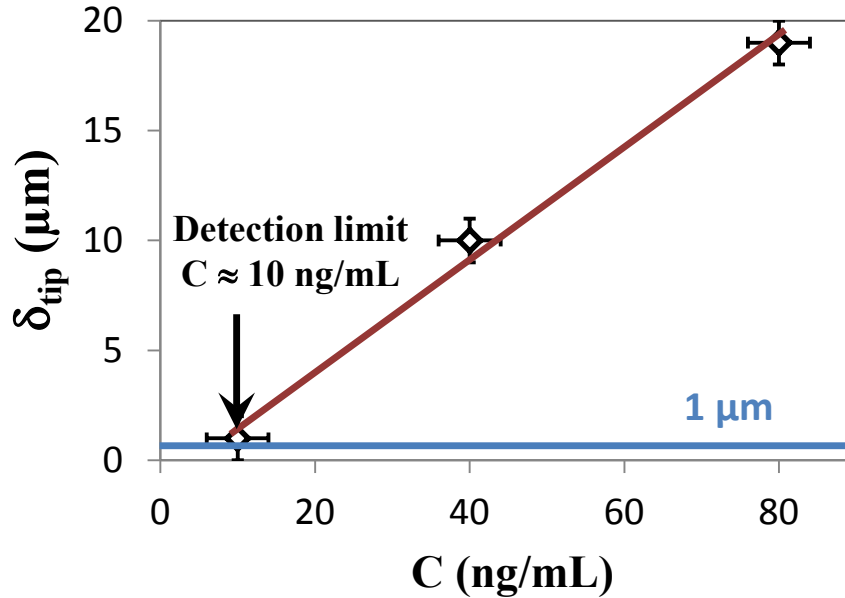


Figure 7-11: Deflection of the cantilever tip due to different antigen concentration and calculation of detection limit

One could notice from Figure 7-10 that the proposed biosensor can respond to the presence of anti-bST in less than 1 min. Indeed, the final response of the cantilever was obtained only around 30 sec upon the stopping the injection of the antigen. This fast behavior proves that the presence of a microfluidic system results in the enhancement of the response time.

## 7.4 Conclusions

In this chapter, a method for the integration of AuNPs on the surface of PDMS is proposed. The gold nanoparticles are synthesized inside a microfluidic environment, a microreactor, and then introduced inside a microfluidic system and allowed to be adsorbed on the PDMS surface after plasma treatment. The spatial distribution of gold nanoparticles on the polymer surface was improved by integration of a 3D micromixer to the reactor to enhance the mixing.

The biosensing capability of the immobilized AuNPs was tested by using the fabricated SPMF as a sensing platform. The gold NPs are integrated on the buried channel of SPMF and the device was further used for the detection of growth hormone based on Ag-Ab interaction. The biosensing experimental results show that the microfluidic sensor responds in less than a minute to the antigen-antibody interaction. The experimental results also show that the proposed sensor has the detection limit of 10 ng/ml (500pM) for the detection of growth hormones. These results show that the proposed micromixer-microreactor platform is an effective method in order to synthesize gold nanoparticles with a narrow size distribution and to suitably integrate them on the surface of PDMS with high uniformity. The prepared Au-PDMS nanocomposite has a lot of application in other microfluidic biosensing applications.

## **Chapter 8: Towards Femtomolar (fM) Sensing of Biomolecular Recognition**

The development of sensitive biosensors for the detection biomolecular interaction is an extremely important and high demanding issue in life sciences. Biosensors based of mechanical transducers, such as microcantilevers, provide a sensitive platform with for applications. Indeed, integration of microfluidics with polymeric microcantilevers would be a suitable choice due to their simple and cheap structure while reducing the analytes consumption as well as enabling fast sensor response towards biomolecular detection. Moving from silicon-based suspended microfluidics towards polymeric suspended microfluidics (PSM) allows us to take rapid strides towards the next generation of ultra-sensitive biosensors to detect micro-organisms with concentrations as low as femto-molar (fM). This chapter reports a method to integrate gold nanoparticles (AuNPs) in a suspended PDMS-microfluidics for biosensing application. The results show that the sensor can reach very high sensitivity of 100pM toward detection of antigen-antibody interaction.

### **8.1 Introduction**

The development of biosensors for the detection of biomolecular interaction is a challenging problem in life science. Progresses in the fabrication of transducers technology along with clear understanding of the governing rules of biomolecular interactions, has led to rapid advancements in the development of biosensors [1].

Recently, fabrication of mechanical biosensor devices with moving parts from a few nanometers to hundreds of microns has become possible. This will enable the fabrication of practical sensors for clinical diagnostics [1,2].

Recent advancements in nanotechnology, microfabrication and microfluidics enabled biosensing methods to be elaborately combined to make *simple, sensitive, and cheap* integrated biosensors. These three factors drive the biosensor world from laboratory use to wide applications in clinical and point-of-care diagnostics [62].

Microfluidic biosensing methods are of interest for a wide range of researchers due to their high-throughput and low-cost mass fabrication [141]. Indeed, microfluidic devices dramatically reduce the required sample/reagent volume. In addition, they accelerate immunoreactions enabling fast response [121].

Integration (or immobilization) of AuNPs inside PDMS microfluidics is a tedious task due to the high hydrophobicity of PDMS. Several methods to integrate AuNPs into the microfluidic devices have been reported [142,143] which can be categorized into two approaches: (1) integration of pre-synthesized AuNPs inside a microfluidic system [145,146,148] and; (2) synthesis of AuNPs inside the microchannel through the *in-situ* synthesis method [151]. In general, the *in-situ* methods show better quality of immobilized AuNPs on PDMS surface in terms of size uniformity while they ensure high stability of particles on the surface [65].

A successful integration of NPs in microchannel opens up new opportunities for the development of ultra-sensitive microfluidic-based biosensors [65]. It is well-established how to immobilize biomolecules (proteins, polypeptide, etc.) on the surface of pre-

immobilized gold nanoparticle through AuNP functionalization. The immobilized biomolecules enable researchers to locally observe and study the behavior of the biomolecular interactions [63].

Besides microfluidic biosensors, microcantilevers transducers are in the focus point of large number of researchers groups due to their simple transduction mechanism which enable label-free biosensing [4,34,38]. Upon interaction of biomolecules, which are already immobilized on the AuNPs integrated in the cantilever, a surface stress ( $\sigma$ ) are induced that results in bending of cantilever [4,17,34,38]. The Stoney's formula relates cantilever end deflection  $\delta$  to the induced surface stress  $\sigma$  as follows [12]:

$$\delta = \frac{3\sigma(1-\nu)}{E} \left( \frac{L}{t} \right)^2 \quad (8-1)$$

Where  $L$  and  $t$  are cantilever length and thickness. This estimation is valid for the cases with large aspect ratio ( $L/t > 10$ ). For devices with  $L/t < 10$  the more detailed analysis of Sader must be used [161].

Unique properties of cantilever biosensors include: (1) Provide exquisite mass sensitivity proportional to their mass and the size of cantilever [3]; (2) The compliance of the mechanical cantilevers can be decreased in the order of three by scaling down the device dimensions. It will allow us to measure forces as small as  $\sim 10$  pN and it corresponds to few nanometer cantilever deflection [1,4].

However there are some drawbacks associated with cantilever biosensors. In biosensing, the cantilever has to be submerged into the sample solution which considerably increase the analytes consumption [4]. Furthermore, the presence of fluids in the optical paths

provide significant challenges for the accurate measurement of cantilever deflection using optical method and in some cases it necessitates usage of complex electrical read-outs to measure the cantilever deflection [21-23,25].

Burg [43] pioneered the integration of microchannels into silicon microcantilevers in 2003 and developed new sensors called “suspended microchannel resonator (SMR)”. The proposed sensor reduced the consumption of sample volumes and at the same time exhibited very low response time (in the range of few minutes) compared with regular cantilever sensors [1,138]. To the best of our knowledge, up to now, all of the proposed SMR sensors used only for different mass detection applications based on frequency shift measurement [44-48,51]. The only issue that kept the SMRs away for applications in biomolecular interaction detection was the lack of a method to immobilize gold nanoparticles inside the buried silicon channels of SMRs.

One of the important issues in the design of biosensors is the sensitivity. As we mentioned earlier, a review paper recently published [1] explains the sensitivity of different sensing mechanisms. Figure 8-1 shows the detection limit of different biosensing mechanisms. As it can be seen in this figure, microfluidic sensors generally have a very good response time (few seconds) in spite of their high detection limit. In contrast, microcantilevers' detection limit is very promising while they have a few hours ( $\approx 1-3$  hrs) response time. Obtaining high sensitivity in short period of time is a challenging problem with immediate application in clinical medicine [1]. This work competes this challenge by reporting, for the first time, a method to integrate gold nanoparticles inside a suspended PDMS-microfluidics (SPMF) as a ultra-sensitive and fast-responding biosensor. The elasticity of PDMS-based platforms is around 5 orders of

magnitude less than that of silicon-based SMRs which enables the improved sensitivity of the device.

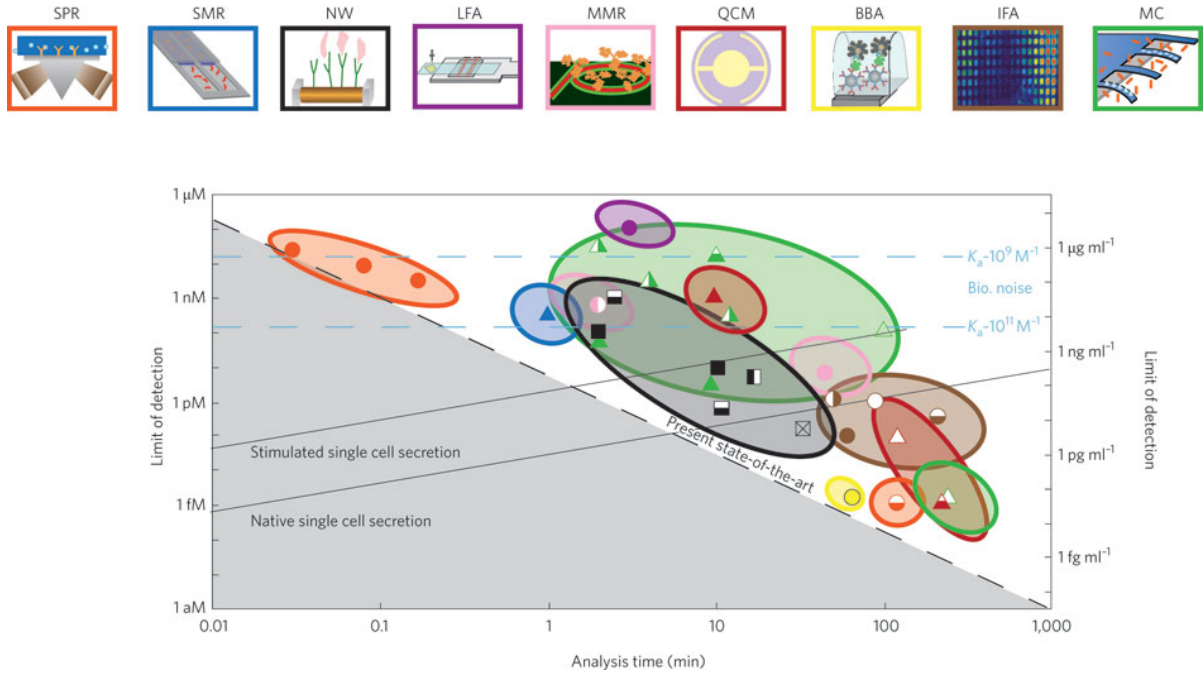


Figure 8-1: The limit of detection in moles and grams per millilitre versus the analysis time for the different types of biosensor for mechanical and non-mechanical sensors. (SPR: surface-plasmon resonance; SMR: suspended microchannel resonator; NW: nanowire; LFA: lateral flow assay; MRR: microring resonator; QCM: quartz crystal microbalance; BBA: biobarcode amplification assay; IFA: immunofluorescent assay; MC: microcantilever [1].

In this work, a developed SPMF is used as a sensor platform. At the beginning, an *in-situ* method was used to integrate AuNPs into the buried microchannel. Finally the SPMF platform was used for the detection of bovine growth hormone under different conditions. The results show that polymeric suspended microfluidics (PSM) allows us to take rapid strides toward to the next generation of biosensors with sensitivities as low as femtomolar (fM) concentrations.

## 8.2 Material and methods

### 8.2.1 Materials

The antibody and antigen used in biosensing are a monoclonal bovine growth hormone (BGH) also known as bovine somatotropin (bST) in mouse, purchased from Dr. Parlow National Hormone and Peptide Program in California. For PDMS compound, Dow Corning Corp's Sylgard® 184 elastomer kit was used and SU-8 was purchased from MicroChem. Gold chloride trihydrate ( $\text{HAuCl}_4 \cdot 3\text{H}_2\text{O}$ ) was purchased from Alfa Aesar. In addition, Nanothink® 18, TWEEN® 20, N-Hydroxysuccinimide (NHS), and N-(3-Dimethylaminopropyl)-N'-ethylcarbodiimide hydrochloride (EDC) were purchased from Sigma Aldrich to be used in biosensing steps.

### 8.2.2 Integration of gold nanoparticles (AuNPs) into microchannel

An *in-situ* method was used to integrate of gold nanoparticles into the buried microchannels of SPMF in the form of Au-PDMS nanocomposite. Aqueous solution of chloroauric acid with 2% concentration was prepared and then introduced into the buried microchannel with a syringe ( $\sim 5\mu\text{l}$ ). Then the whole chip was kept at room temperature for 48 hours. The inlet/outlet was closed in order to avoid evaporation of the solution.

As we already mentioned in detail in Chapter 2 of this thesis, the curing agent (cross-linking agent) in PDMS compound reduces the gold ions to gold nanoparticles embedded into the polymer network [63]. The relatively high concentration of the gold precursor (2%) were used in order to increase the rate of the reaction.

After keeping the solution for 48h inside the SPMF, the channel turns to red showing the presence of AuNPs inside the microchannel. A heat treatment then used in order to improve the size distribution of AuNPs in PDMS [63,65]. Indeed, annealing process reduces the particle aggregation and results in uniformly distribution particles on PDMS surface. For annealing, the nano-integrated SMPF devices are heated from room temperature to 300°C in 10 minutes and then kept at this temperature for 30 min.

### ***8.2.3 Biosensing protocol and experiment***

Label-free biosensing tests have been performed by using the annealed SPMF microcantilevers. The bST antibody (anti-BGH) and its corresponding antigen (Ag) were used for the biosensing experiments.

Immobilization of Ab on the gold nanoparticles is carried out though functionalizing the nanoparticles with 5mM 11-mercaptoundecanoic acid (NanoThink® ACID11) in ethanol (5mM), by introducing the solution into the microchannel and keeping it for at least 5 h. Before attaching the Ab to the linkers, which are connected to AuNPs from the previous step, the linkers should be activated. The conventional carbodiimide coupling chemistry (EDC/NHS) is used to activate the carboxyl groups. The activation step was carried out by injecting a mixture (volume ratio of 1:1) of 0.4M N-(3-dimethylaminopropyl)-N'-ethylcarbodiimide hydrochloride (EDC) and 0.1M N-hydroxysuccinimide (NHS) into the buried channel for 1 hour. The activated linkers are now ready to host Ab. Upon introduction of 200ng/ml solution of antibody in PBS buffer solution for 8 h, the Ab immobilized on the AuNPs. The process followed by washing the microchannel several times with a TWEEN® 20 solution in PBS (0.05%). The last step in biosensing protocol

is the introduction of complementary Ag dissolved in PBS buffer solution using a syringe pump. The antigen solution was introduced into the channel by using a syringe pump at a flow rate of 10 $\mu$ l/min. When the Ag solution is injected into the channel, they interact with the immobilized Ab molecules and induce a surface-stress which bends the cantilever.

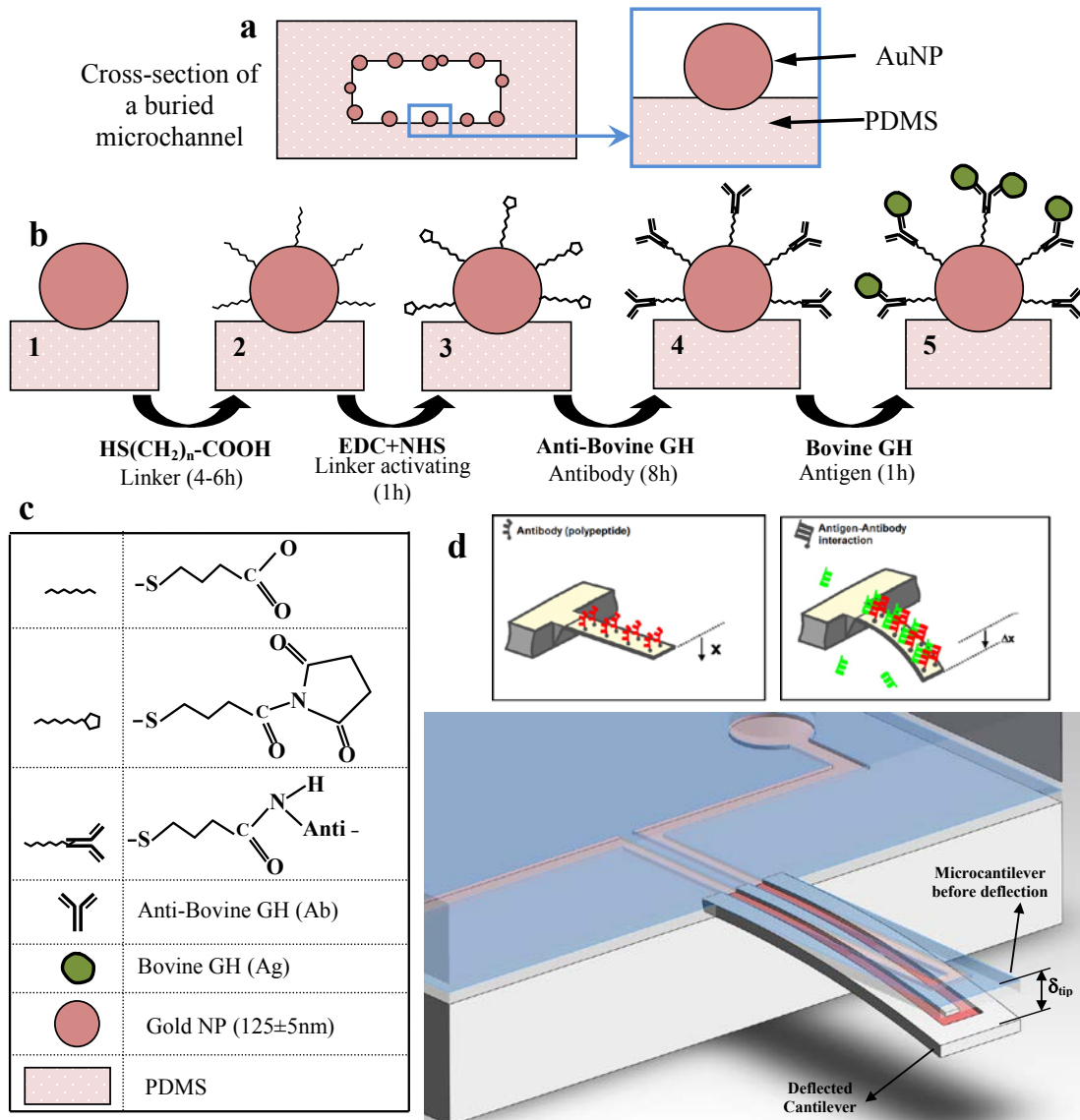


Figure 8-2: (a) A cross section of the buried microchannel of SPMF and the formation of AuNPs on the PDMS surface; (b) four steps of the biosensing protocol to immobilize Ab of the surface of AuNP; (c) legend of the figure; (d) schematic of the deflection of cantilever tip due to the interaction of antigen-antibody [34].

In Figure 8-2-a the schematics of formation of AuNPs on the surface of buried microchannel of SPMF is shown. Furthermore, the immobilization steps of Ab on the surface of AuNP are schematically shown in Figure 8-2-b. Figure 8-2-d shows that the cantilever response in form of bending due to the interaction of Ag–Ab that result in induced surface-stress.

The magnitude of cantilever deflection is proportional to the induced surface stress which is related to the concentration of Ag solution. The schematic of cantilever deflection setup and the device under test (DUT) are shown in Figure 8-3 and Figure 8-4-a respectively. In Figure 8-4-b, an image of the cantilever tip, under microscope is also shown.

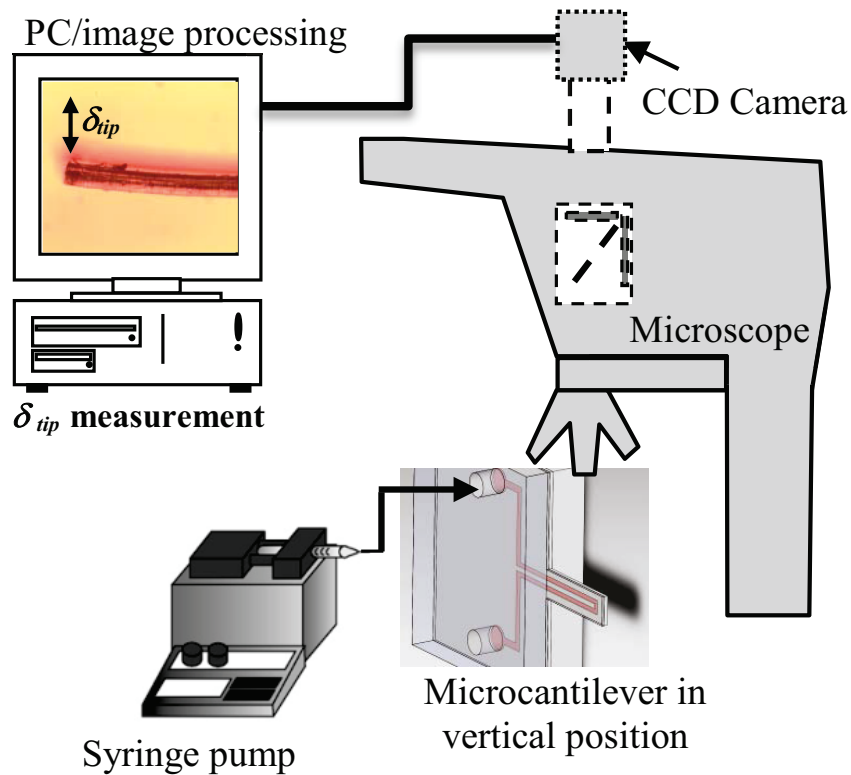


Figure 8-3: Schematic of the experimental setup for the deflection measurement of the cantilever

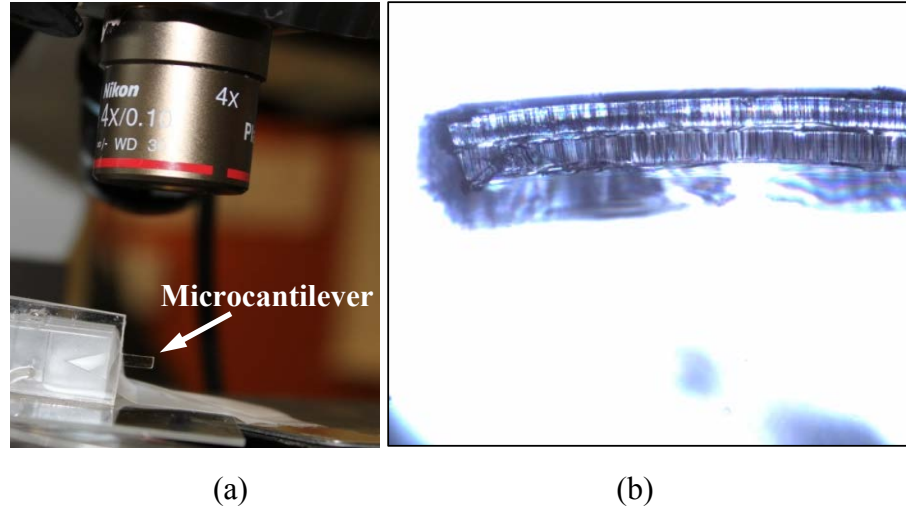


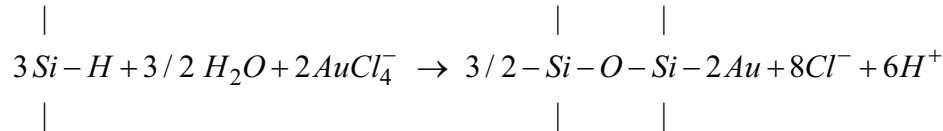
Figure 8-4: (a) Device under test (DUT); Image of the cantilever tip recorded by CCD camera

The biosensing experiments were performed under an optical microscope to track the cantilever tip as shown in Figure 8-4-a. The tip deflection was calculated by using the analysis of the obtained images from the microscope (Figure 8-4-b). Different antigen concentrations were tested to obtain the detection limit of the proposed integrated cantilever biosensor.

## 8.3 Results and Discussion

### 8.3.1 *Au-PDMS nanocomposite fabrication and SEM characterization*

After the *in-situ* synthesis of AuNPs on the surface of PDMS microchannel, in the form of Au-PDMS nanocomposite, the devices are annealed. To characterize the Au-PDMS nanocomposite formed inside the buried microchannel, SEM imaging was used. The size distribution histograms were extracted from the SEM images using Gwyddion 2.28 data visualization modular program. The following *in-situ* reduction reaction has been suggested between the gold ions and cross-linking agent of PDMS [74]:



The reduction reaction is schematically shown in a cross-section of the buried channels of SPMF in Figure 8-5. Upon introduction of the gold solution, the curing (cross-linking) agent of the PDMS will act as a reductant and initiate the gold nanoparticle to crystalize and grow into the PDMS polymer network as illustrated in Figure 8-5. The *in-situ* reduction reaction ensures high stability of the AuNPs on the PDMS surface as the particles are embedded in the polymer and interact strongly with the polymer network. Indeed, our experiments verify that the leaching of particles can be ignored. However the *in-situ* process is a slow process (take around 48 hours) because of the heterogeneous nature of the reaction. The amount of the cross-linking agent (curing agent) available for the reduction of Au<sup>3+</sup> is not enough and therefore migration of the cross-linking agent toward the PDMS surface during the reaction is the another issue that explains the slow reaction. Possible migration of cross-linking agents of PDMS is schematically shown by dashed arrow in Figure 8-5.

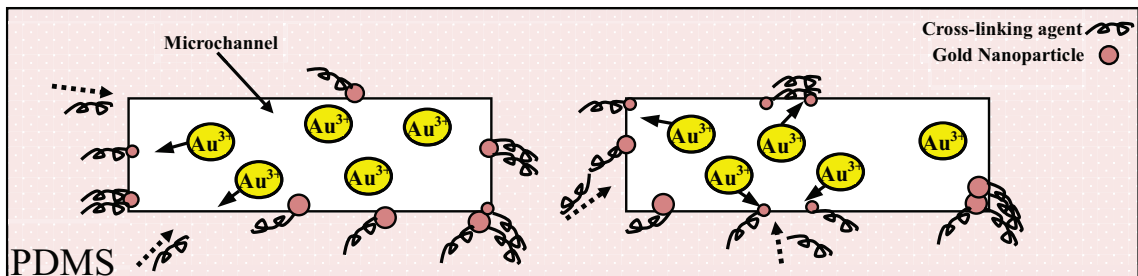


Figure 8-5: Illustration of the *in-situ* reaction at the cross-section of microcantilever and the migration of reducing agent toward the channel wall.

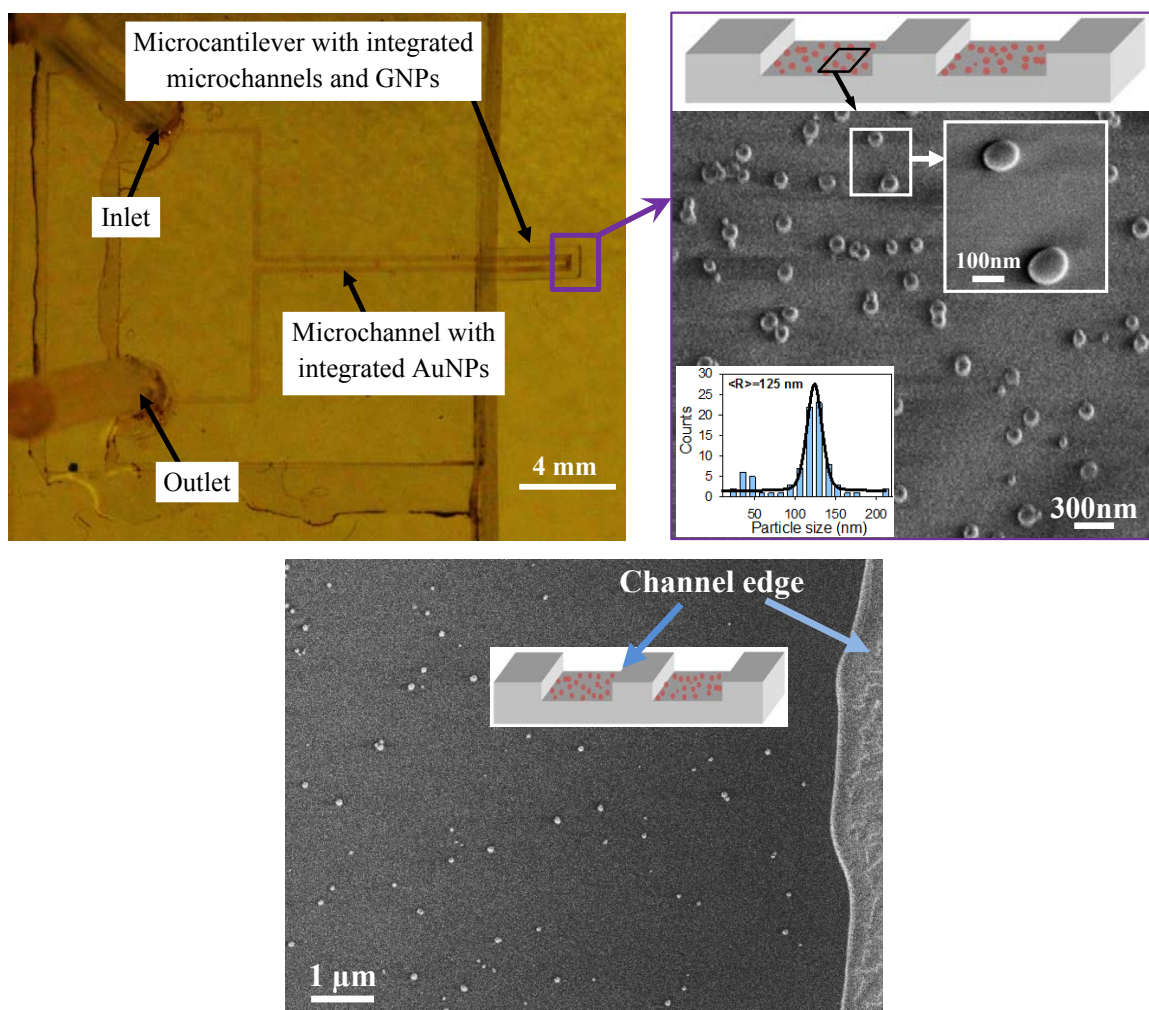


Figure 8-6: gold nanoparticle integrated microfluidic buried microcantilever biosensor. The SEM image shows the size distribution of AuNPs inside the channel.

A fabricated SPMF with integrated AuNPs is shown in Figure 8-6. In this figure, the SEM images of the annealed PDMS nanocomposite and close-up images of the AuNPs are also shown.

The size distribution histogram of the nanocomposite shows a very narrow size distribution of the particle with less than 8% size variation ( $125 \text{ nm} \pm 5 \text{ nm}$ ). High uniformity of the synthesized particles makes the composite cantilever platform a suitable candidate for sensitive biosensing experiments.

### 8.3.2 Kinetics of the *in-situ* reduction reaction

The *in-situ* reaction carried out at three different temperatures including room temperature (22°C), 40°C, and 50°C in order to study the temperature-dependent behavior of the *in-situ* synthesis, kinetics of the reaction. In each temperature, the Au-LSPR peak absorbance band of the nanocomposite was obtained during the first 48 h of the reaction. Our results show a linear relationship between the time of reaction and the Au-LSPR absorbance. The slope of this line (in each temperature) corresponds to the apparent rate constant of the *in-situ* reaction,  $k^*$ , which is tabled in Table 8-1. It should be noted that for the reaction times more than 120 h, the graph starts to saturate. The results in Table 8-1 show that there is a high dependency between the  $k^*$  and temperature meaning the *in-situ* reaction rate can be enhanced at higher temperatures. Detailed discussions of the kinetic data are included in Chapter 5 of this thesis.

Table 8-1: The apparent rate constants of the formation of gold NPs at different temperatures

T (°C)	$k^*$ (h <sup>-1</sup> )
22 ±0.5	0.5×10 <sup>-3</sup>
40 ±0.5	1.1×10 <sup>-3</sup>
50 ±0.5	1.4×10 <sup>-3</sup>

Furthermore, the Arrhenius equation was used to estimate the activation energy  $E_a$  of the *in-situ* reaction as following:

$$k = Ae^{-E_a/RT} \rightarrow \ln(k) = -\frac{E_a}{R} \frac{1}{T} + \ln(A) \quad (8-1)$$

Where  $k$  is the rate constant of the reaction at the temperature  $T$  (in Kelvin),  $A$  is the pre-exponential or frequency factor, and  $R$  is the universal gas constant ( $R=8.314 \text{ J/mol.K}$ ).

The activation energy is expressed in  $\text{J/mol}$ .

Considering the reduction reaction has a rate constant that obeys the Arrhenius equation, a plot of  $\ln(k^*)$  (in  $\text{s}^{-1}$ ) versus  $T^{-1}$  follows a straight line. The slope of this line (the slope of Arrhenius plot) can be used to calculate the apparent activation energy,  $E_a^*$ , of the reaction using the following equation:

$$E_a^* = -R \times \left( \frac{\ln(k^*)}{\frac{1}{T}} \right) = 29.8 \frac{\text{kJ}}{\text{mol}} \quad (5-2)$$

The relatively large value of the activation energy ( $E_a^* \sim 30 \text{ kJ/mol}$ ) shows that the reaction needs a high energy contribution. The reaction is facilitated at high temperatures when the migration of the reducing agent is faster. It should be noted that the data were calculated here are obtained from spectrometric measurements, and therefore, they are indicated as apparent rates and apparent activation energy.

### ***8.3.3 Static deflection of SPMF cantilever***

The deflection measurement of the cantilever tip was performed by using the setup shown in Figure 8-3. The images obtained from the tip of the cantilever were recorded and analyzed in order to calculate the deflection of the cantilever tip. A concern that should be considered in the deflection measurement is that the cantilever was deflected as a result of surface-stress induced as the result of biomolecular interaction and not the rotation of whole cantilever. In order to justify this issue, two fixed points were assumed

along the cantilever and then a line was passed through them to measure the cantilever angle before and after deflection as shown in Figure 8-7. Variation of the slope of this line is an evidence that the cantilever is bended (and not moved) by assuming this fact that the base of the cantilever is fix and rigid enough which is our assumption.

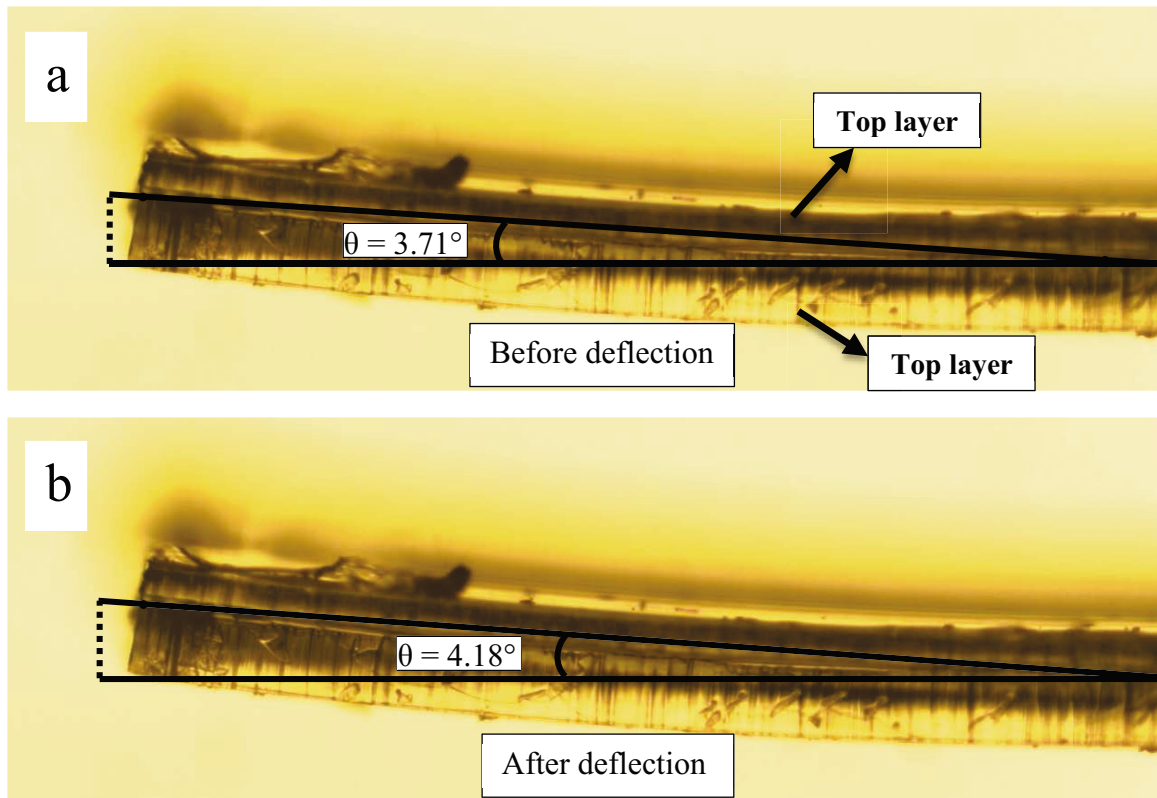


Figure 8-7: calculation of the cantilever bending by measuring the bending of the cantilever.

### ***8.3.4 Biosensing experiment and estimation of detection limit***

The biosensing experiments performed using a SPMF with the cantilever dimensions of 4 mm long, 1.2 mm width and 165  $\mu\text{m}$  thick. The antigen was injected into the buried microchannel at the last step of biosensing and at the same time the deflection of the cantilever was recorded using a CCD camera that was mounted on an optical microscope.

Figure 8-8 shows the response of the cantilever deflection for 12 min of biosensing experiment upon injection of 4nM growth hormone. The antigen solution was injected into the microchannel at  $t = 240 \text{ sec}$  with a flow rate of  $10 \mu\text{l}/\text{min}$ . Then the syringe-pump was stopped at  $t=310 \text{ sec}$  when the antigen solution filled the buried microfluidic completely meaning the antigens are in contact with immobilized antibodies. The time zone that correspond to different phases that occur during the biomolecular interaction are marked in Figure 8-8-a. The response in this figure shows that the cantilever is finally deflected by  $35 \mu\text{m}$  as the result of induced surface-stress upon Ag-Ab interaction.

Figure 8-8-b shows the response of cantilever encompasses three different phases during the interaction. The first phase is when the cantilever is at its rest condition with the deflection of  $\delta_{\text{tip}}=0$ . The second phase starts at  $t=240 \text{ sec}$  when the syringe pump starts to inject the Ag solution. This phase can be considered as a transient phase and it includes disturbances and noises and it lasts for around 120sec when the cantilever tip reached to its final steady-state response of  $35 \mu\text{m}$  approximately. The last phase (steady-state response) is when the cantilever deflects fully due to the induced surface-stress.

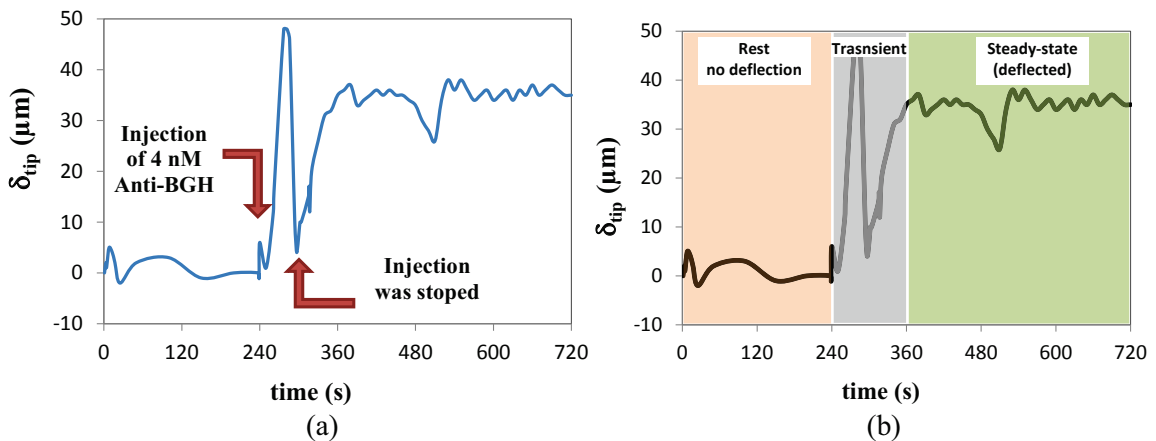


Figure 8-8: Response of the cantilever while the gold NPs were obtained by an *in-situ* method in the channels of the cantilever.

After each experiment, the buried microchannel was washed several times with the 0.01% Tween solution and DI water and dried in an oven at 50°C to make sure there is no more antigen/antibody immobilized on the AuNPs. After the washing process, the cantilever was used for another biosensing experiments. The steady-state cantilever tip deflection measurement was obtained for three different concentrations including 80 ng/ml, 40 ng/ml and 10 ng/ml. These results were used to estimate the detection limit of the SPMF sensor. Biosensing experiments under different Ag concentrations revealed that the SPMF biosensor has a high sensitivity as low as 2 ng/ml (100 pM). This limit is obtained by extrapolation of the obtained graph and by assuming 1 μm precision in the cantilever deflection measurement (minimum detectable deflection), as it shown in Figure 8-9. The horizontal error bars in this figure shows 4% error in the preparation of Ag solution in PBS and the vertical bars shows 1 μm error in the measurement of cantilever tip deflection.

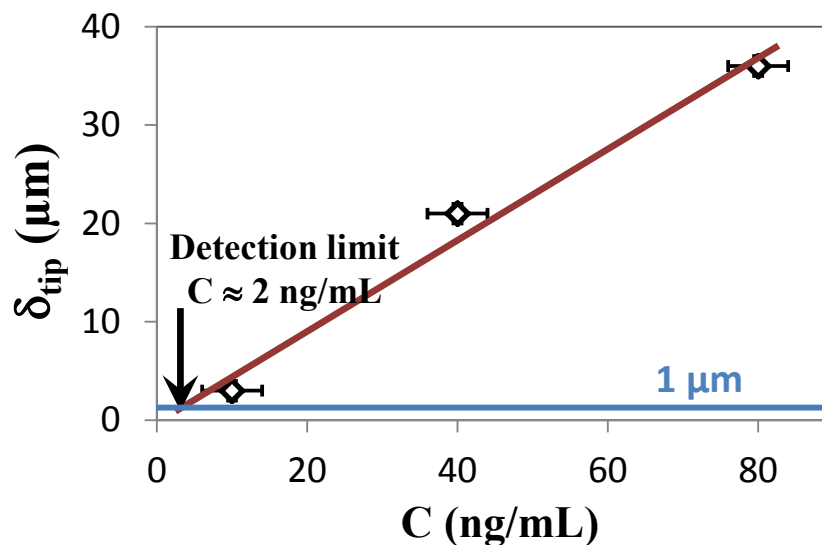


Figure 8-9: Deflection of the cantilever tip due to different antigen concentration and estimation of the limit of detection

A promising achievement in the biosensing results is the response time of the cantilever due to the induced surface-stress. As it can be seen from the Figure 8-8, the cantilever has reached its steady-state position of 35  $\mu\text{m}$  only about 60 sec after the injection of Ag solution inside the buried microchannel. The fast response time can be accounted by the occurrence of Ag-Ab interaction in a microfluidic environment.

## 8.4 Conclusion

In this chapter a method for the integration of gold nanoparticles inside a suspended PDMS-microfluidics is proposed. Gold nanoparticles were integrated into the buried microchannel using an *in-situ* method on the basis of the reductive properties of cross-linking agent of the PDMS compound. Strong interaction between the gold nanoparticles and PDMS surface ensures high stability of immobilized particles into the surface. The fabricated Au-PDMS nanocomposite provides a suitable platform toward effective immobilization of biomolecules on the surface of gold nanoparticles for biosensing applications. The integrated platform was finally used toward for the detection of bovine somatotropin (bST) based on Ag-Ab interaction.

The results show that the sensor can reach very-low detection limits, as low as 2ng/ml (100pM) toward the detection of bST. In addition, the results show a high response time of 60 sec for the detection of Ag. The sensitivity of the system can be easily improved by decreasing the platform size and improving the cantilever deflection measurement system,. The results of this work presents successful demonstration of application of integrated polymeric cantilever for ultra-high sensitive detection of biomolecular recognition. Indeed, utilization of polymeric suspended microfluidics (PSM) compared

with silicon-based suspended microfluidics allows us to take rapid strides toward to the next generation of ultra-sensitive biosensors and proves that the detection of biomolecule with concentrations as low as femto-molar (fM) is totally possible.

## Chapter 9: Conclusions

### 9.1 Summary and conclusions

In the present thesis the integration of gold nanoparticles inside a suspended microfluidic system is performed. The integrated device has been used as an ultra-sensitive biosensor for the detection of growth hormones.

Process methods were developed to integrate gold nanoparticles inside a suspended polymeric microfluidic called SPMF. Moreover, a fabrication method was proposed to fabricate a PDMS microcantilever with buried microchannel. In short, the key features of different steps toward the fabrication of final integrated biosensor are listed below:

- a. Gold-PDMS nanocomposite was fabricated by using a novel *in-situ* method by using different carrier fluids of gold salt including water and ethanol. The results show that due to high permeability of ethanol into the polymer network, the reaction is around one order of magnitude faster than water as the carrier fluid. The results showed that the process can be performed as fast as 7 hours by using ethanol while it takes around 50 hours with aqueous solution of gold salt. The platform was used for the antigen-antibody interaction based of the plasmonic properties of the gold nanoparticles. The results show that the samples prepared with water solution show better sensing properties than ethanol samples.
- b. Post-processing of the Au-PDMS nanocomposite can effectively improve the biosensing capability of the platform such as annealing and swelling of the

polymer network. In particular, the combination of annealing and swelling can double the sensitivity of the platform toward the refractive index of medium.

- c. A microwave-assisted reduction of gold ions into the PDMS polymer was proposed. The fabrication procedure resulted in a narrow size distribution of the particles into the polymer surface. The sensitivity of the platform toward the refractive index of the medium was obtained as high as 102nm/RIU showing a promising method for the fabrication of biosensor platforms. The method has the capability to be integrated with microfluidic systems.
- d. A novel, simple and low-cost PDMS micromixer was proposed to improve the mixing at low Reynolds number flow rates in microfluidic environment. The designed micromixer was simulated under real conditions and the mixing efficiency was defined by introducing a new method. Furthermore, the micromixer was fabricated and the flow was visualized in the channel. At the final step, a mixing experiment was accomplished to evaluate its performance quantitatively in the real conditions using mixing of acid and base. The results show a mixing efficiency of 85% for the flow rates up to 40  $\mu\text{l}/\text{min}$  meaning fully mixing for  $R_e < 5.5$ . Due to the simplicity of the proposed micromixer, the mixing unit can be easily integrated with micro-total analysis systems ( $\mu$ -TAS).
- e. Gold-PDMS nanocomposite was synthesized in a microfluidic channel through an *in-situ* reaction. It was found that the reaction is slower in the micro-environment than at a macro-scale. The SEM images show that the size distribution of AuNPs synthesized in the microchannel was found to be 120-130 nm (8% size variation) which was considerably improved and narrower compared with macro-scale

sample which resulted in a range of 105-175 nm (67% size variation). This means that the reaction in microfluidic environment improves the uniformity around an order of magnitude (8.3 times).

- f. The kinetics of the synthesis of AuNPs in the microfluidic environment was studied in detail and the apparent activation energy of the reaction was estimated  $E_a^* = 30\text{kJ/mol}$  by using the Arrhenius equation. The LSPR-based microfluidic biosensor was finally used for hormone detection and the results show the proposed sensor obtained a detection limit as low as 4 ng/ml toward the Ag-Ab interaction detection of bST.
- g. To the best of our knowledge, for the first time, a method for the fabrication of PDMS microcantilever with buried microchannel by using SU-8 process for mold fabrication was proposed. The fabricated device is referred to "*suspended PDMS-microfluidics (SPMF)*". The simulation results show a non-linear behavior of the cantilever to the applied surface stress. Therefore, the cantilever thickness was optimized for the high cantilever tip deflection for a pre-determined induced surface-stress during the biosensing applications.
- h. By using the *in-situ* method, AuNPs was integrated with the SPMF platform and the response of the cantilever was obtained during the Ag-Ab interaction. The results show the proposed integrated biosensor can reach a sensitivity as low as 100pM toward the Ag-Ab recognition of growth hormones.

## 9.2 Future works

The objective of this thesis was to develop a method to integrate gold nanoparticles in polymeric free-standing structures for biosensing applications. Several steps have been

done towards the integration of gold nanoparticles in suspended PDMS-microfluidics. However, there are still a number of considerations that can be implemented for the further improvement of the presented biosensor. Such improvements are discussed below:

- a. The preparation of PDMS-nanocomposite sensing platform by using microwave-assisted synthesis of gold ions performed in batch. Due to high sensitivity of the fabricated platform, it is suggested that the integration of the method in a microfluidic chip can be performed to achieve high sensitive LSPR-based biosensor. Indeed, the kinetics of the reaction in the microfluidic environment should be thoroughly discussed. Furthermore, the integration of the microwave-assisted AuNPs formation method with the SPMF can also lead towards a promising ultra-high sensitive cantilever biosensor that can easily explore the femtomolar region.
- b. The *in-situ* reduction reaction in a microfluidic chip was performed under the static condition. In another word, there was no flow in the microfluidic chip during the *in-situ* reaction. However, one of the main advantages of microfluidics is the considerably accelerated heat and mass transport due to improved diffusion in the small scales. There would be a great possibility to have a very uniform size distribution of gold nanoparticles in the dynamic *in-situ* synthesis.
- c. The reduction of gold nanoparticles inside the microreactor should be investigated in more detail under various conditions. In particular, the effect of temperature and that of the flow rate should be studied in detail.

- d. The size of the microcantilever was assumed to be 1.2mm by 4mm. However, based on the proposed method, for the fabrication of the cantilever, there is a possibility to reduce the cantilever size as well as the thickness of the cantilever. The detection limit of the proposed biosensor depends strongly on these dimensions. Indeed, by decreasing the width of buried microchannel, the thickness of thin cover layer of cantilever and therefore the whole cantilever thickness can be reduced. This will result in the reduced stiffness of the cantilever which can directly enhance the sensitivity of the device.
- e. The biosensing experiment performed on this thesis was based on the interaction of a specific antigen/antibody of growth hormone. More biosensing experiments including DNA-hybridization and another antigen/antibody interaction experiments should be performed to qualitatively and quantitatively assess the suitability of the proposed biosensor for different bimolecular interactions.
- f. The fabricated SPMF may be used as a flow-sensor. It is suggested to measure the cantilever deflection with different flow-rates ( $Q$ ) and find a relationship between the cantilever deflection and flow rate. The resulting curve can be used to calibrate the device for flow measurements.

## Reference

1. J. Arlett, E. Myers and M. Roukes, *Nature nanotechnol.*, 2011, 6, 203-215.
2. T. Thundat, P. Oden and R. Warmack, *Microscale. Therm. Eng.*, 1997, 1, 185-199.
3. A. Moulin, S. O'shea and M. Welland, *Ultramicroscopy.*, 2000, 82, 23-31.
4. J. Fritz, M. Baller, H. Lang, H. Rothuizen, P. Vettiger, E. Meyer, H. J. Güntherodt, C. Gerber and J. Gimzewski, *Science.*, 2000, 288, 316-318.
5. N. V. Lavrik, C. A. Tipple, M. J. Sepaniak and P. G. Datskos, *Chem. Phys. Lett.*, 2001, 336, 371-376.
6. V. Tabard-Cossa, McGill University, 2005.
7. K. K. Liu, R. G. Wu, Y. J. Chuang, H. S. Khoo, S. H. Huang and F. G. Tseng, *Sensors.*, 2010, 10, 6623-6661.
8. J. Satija, R. Bharadwaj, V. Sai and S. Mukherji, *Nanotechnol. Science Applications.*, 2010, 3, 171-188.
9. M. Vidotti, R. F. Carvalhal, R. K. Mendes, D. Ferreira and L. T. Kubota, *J. Braz. Chem. Soc.*, 2011, 22, 3-20.
10. L. L. Beecroft and C. K. Ober, *Chem. Mater.*, 1997, 9, 1302-1317.
11. P. Devi, A. Y. Mahmoud, S. Badilescu, M. Packirisamy, P. Jeevanandam and V. V. Truong, Synthesis and Surface Modification of Poly (dimethylsiloxane)-Gold Nanocomposite Films for Biosensing Applications, 2010.
12. G. G. Stoney, *Proc. R. Soc. A*, 1909, 172-175.
13. M. Godin, V. Tabard-Cossa, P. Grutter and P. Williams, *Appl. Phys. Lett.*, 2001, 79, 551-553.
14. K. S. Hwang, K. Eom, J. H. Lee, D. W. Chun, B. H. Cha, D. S. Yoon, T. S. Kim and J. H. Park, *Appl. Phys. Lett.*, 2006, 89, 173905-173905-173903.
15. M. J. Lachut and J. E. Sader, *Phys. Rev. Lett.*, 2007, 99, 206102.
16. S. Kim and K. Kihm, *Appl. Phys. Lett.*, 2008, 93, 081911-081911-081913.
17. G. Wu, H. Ji, K. Hansen, T. Thundat, R. Datar, R. Cote, M. F. Hagan, A. K. Chakraborty and A. Majumdar, *Proc. Natl. Acad. Sci. U. S. A.*, 2001, 98, 1560-1564.
18. P. S. Waggoner and H. G. Craighead, *Lab. Chip.*, 2007, 7, 1238-1255.
19. G. Chen, T. Thundat, E. Wachter and R. Warmack, *J. Appl. Phys.*, 1995, 77, 3618-3622.
20. C. Ziegler, *Anal. Bioanal. Chem.*, 2004, 379, 946-959.
21. G. Shekhawat, S. H. Tark and V. P. Dravid, *Science.*, 2006, 311, 1592-1595.
22. G. A. Campbell and R. Mutharasan, *Biosens. Bioelectron.*, 2006, 21, 1684-1692.
23. S. H. Tark, A. Srivastava, S. Chou, G. Shekhawat and V. P. Dravid, *Appl. Phys. Lett.*, 2009, 94, 104101-104101-104103.
24. H. H. Tsai, C. F. Lin, Y. Z. Juang, I. Wang, Y. C. Lin, R. L. Wang and H. Y. Lin, *Sens. Actuators B Chem.*, 2010, 144, 407-412.
25. A. Choudhury, P. J. Hesketh, T. Thundat and Z. Hu, *J. Micromech. Microeng.*, 2007, 17, 2065-2076.

26. T. Thundat, E. Wachter, S. Sharp and R. Warmack, *Appl. Phys. Lett.*, 1995, 66, 1695-1697.
27. T. Thundat, G. Chen, R. Warmack, D. Allison and E. Wachter, *Anal. Chem.*, 1995, 67, 519-521.
28. K. Hill, P. Dutta, A. Zareba, M. L. Eldridge and M. J. Sepaniak, *Anal. Chim. Acta.*, 2008, 625, 55-62.
29. C. A. Tipple, N. V. Lavrik, M. Culha, J. Headrick, P. Datskos and M. J. Sepaniak, *Anal. Chem.*, 2002, 74, 3118-3126.
30. E. Lee and H. S. Hong, An integrated system of microcantilever arrays with carbon nanotube tips for bio/nano analysis: design and control, 2005.
31. B. H. Cha, S. M. Lee, J. C. Park, K. S. Hwang, S. K. Kim, Y. S. Lee, B. K. Ju and T. S. Kim, *Biosens. Bioelectron.*, 2009, 25, 130-135.
32. B. Ilic, Y. Yang and H. Craighead, *Appl. Phys. Lett.*, 2004, 85, 2604-2606.
33. K. M. Hansen, H. F. Ji, G. Wu, R. Datar, R. Cote, A. Majumdar and T. Thundat, *Anal. Chem.*, 2001, 73, 1567-1571.
34. R. McKendry, J. Zhang, Y. Arntz, T. Strunz, M. Hegner, H. P. Lang, M. K. Baller, U. Certa, E. Meyer and H. J. Güntherodt, *Proc.Natl. Acad. Sci. U. S. A.*, 2002, 99, 9783-9788.
35. M. Su, S. Li and V. P. Dravid, *Appl. Phys. Lett.*, 2003, 82, 3562-3564.
36. G. Wu, R. H. Datar, K. M. Hansen, T. Thundat, R. J. Cote and A. Majumdar, *Nature. biotechnol.*, 2001, 19, 856-860.
37. J. H. Lee, K. S. Hwang, J. Park, K. H. Yoon, D. S. Yoon and T. S. Kim, *Biosens. Bioelectron.*, 2005, 20, 2157-2162.
38. N. Backmann, C. Zahnd, F. Huber, A. Bietsch, A. Plückthun, H. P. Lang, H. J. Güntherodt, M. Hegner and C. Gerber, *Proc.Natl. Acad. Sci. U. S. A.*, 2005, 102, 14587-14592.
39. J. Bausells Roigé, *Contributions to science*, 2006, 67-78.
40. L. R. Senesac, P. Dutta, P. G. Datskos and M. J. Sepaniak, *Anal. Chim. Acta.*, 2006, 558, 94-101.
41. N. V. Lavrik and P. G. Datskos, *Appl. Phys. Lett.*, 2003, 82, 2697-2699.
42. P. J. Chapman, Z. Long, P. G. Datskos, R. Archibald and M. J. Sepaniak, *Anal. Chem.*, 2007, 79, 7062-7068.
43. T. P. Burg and S. R. Manalis, *Appl. Phys. Lett.*, 2003, 83, 2698-2700.
44. M. G. von Muhlen, N. D. Brault, S. M. Knudsen, S. Jiang and S. R. Manalis, *Anal. Chem.*, 2010, 82, 1905-1910.
45. T. P. Burg, A. R. Mirza, N. Milovic, C. H. Tsau, G. A. Popescu, J. S. Foster and S. R. Manalis, *J. Microelectromech. S.*, 2006, 15, 1466-1476.
46. J. Lee, W. Shen, K. Payer, T. P. Burg and S. R. Manalis, *Nano Lett.*, 2010, 10, 2537-2542.
47. A. Gupta, D. Akin and R. Bashir, *Appl. Phys. Lett.*, 2004, 84, 1976-1978.
48. T. P. Burg, M. Godin, S. M. Knudsen, W. Shen, G. Carlson, J. S. Foster, K. Babcock and S. R. Manalis, *Nature.*, 2007, 446, 1066-1069.
49. Y. Lu and M. Wang, *Chinese. J. Anal. Chem.*, 2009, 37, 923-928.
50. D. Psaltis, S. R. Quake and C. Yang, *Nature.*, 2006, 442, 381-386.
51. P. Dextras, T. P. Burg and S. R. Manalis, *Anal. Chem.*, 2009, 81, 4517.

52. F. S. Aggor, E. M. Ahmed, A. El-Aref and M. Asem, *J. American Sci.*, 2010, 6, 648-656.
53. Z. Chang, S. Li, M. Bouquey, I. Kraus, C. Serra and J. Köhler, Continuous-microflow synthesis of multiscale materials based on polymer microparticles/inorganic nanoparticles composites, 2010.
54. J. Wagner and J. Köhler, *Nano Lett.*, 2005, 5, 685-691.
55. C. Hsieh and S. Hsieh, *J. Mater. Chem.*, 2011, 21, 16900-16904.
56. P. H. C. Camargo, K. G. Satyanarayana and F. Wypych, *Mater. Res.*, 2009, 12, 1-39.
57. D. Li, C. Li, A. Wang, Q. He and J. Li, *J. Mater. Chem.*, 2010, 20, 7782-7787.
58. S. K. Sia and G. M. Whitesides, *Electrophoresis.*, 2003, 24, 3563-3576.
59. A. Scott, R. Gupta and G. U. Kulkarni, *Macromol. Chem.Phys.*, 2010, 211, 1640-1647.
60. R. Gradess, R. Abargues, A. Habbou, J. Canet-Ferrer, E. Pedrueza, A. Russell, J. L. Valdés and J. P. Martínez-Pastor, *J. Mater. Chem.*, 2009, 19, 9233-9240.
61. M. Tagaya and M. Nakagawa, *Smart Mater. Res.*, 2010, 2011, ID 390273, 390277 pages.
62. G. M. Whitesides, *Lab. Chip.*, 2011, 11, 191-193.
63. H. SadAbadi, S. Badilescu, M. Packirisamy and R. Wuthrich, *J. Biomed. Nanotechnol.*, 2012, 8, 539-549.
64. H. SadAbadi, S. Badilescu, M. Packirisamy and R. Wuthrich, *Synthesis and Characterization of Gold-Poly (dimethyl siloxane) Nanocomposites Obtained by In-Situ Microwave-Induced Reduction of Gold Ions*, Wiley, 2012.
65. H. SadAbadi, S. Badilescu, M. Packirisamy and R. wuthrich, *Biosens. Bioelectron.*, 2012, Manuscript No. BIOS-D-12-02459.
66. H. SadAbadi, S. Badilescu, M. Packirisamy and R. Wuthrich, *IEEE Sens. J.*, 2012, Manuscript No. Sensors-7064-2012.
67. H. SadAbadi, M. Packirisamy and R. Wuthrich, *Lab. Chip.*, 2012, Manuscript No. LC-ART-09-2012-041067.
68. H. SadAbadi, M. Packirisamy and R. Wuthrich, *Nature nanotechnol.*, 2012, to be submitted.
69. A. Stepanov and R. Khaibullin, *Rev. Adv. Mat. Science.*, 2004, 7, 108-125.
70. G. Carotenuto, G. L. Peruta and L. Nicolais, *Sens. Actuators B Chem.*, 2006, 114, 1092-1095.
71. I. Wong and C. M. Ho, *Microfluid Nanofluid.*, 2009, 7, 291-306.
72. J. A. Vickers, M. M. Caulum and C. S. Henry, *Anal. Chem.*, 2006, 78, 7446-7452.
73. M. Alsawafta, S. Badilescu, A. Paneri, V. V. Truong and M. Packirisamy, *Polymers.*, 2011, 3, 1833-1848.
74. Q. Zhang, J. J. Xu, Y. Liu and H. Y. Chen, *Lab. Chip.*, 2008, 8, 352-357.
75. A. Goyal, A. Kumar, P. K. Patra, S. Mahendra, S. Tabatabaei, P. J. J. Alvarez, G. John and P. M. Ajayan, *Macromol. Rapid Commun.*, 2009, 30, 1116-1122.
76. J. Ozhikandathil, S. Badilescu and M. Packirisamy, Synthesis and characterization of silver-PDMS nanocomposite for the biosensing applications, 2011.
77. G. Barbillon, J. L. Bijeon, J. Plain, M. L. de la Chapelle, P. M. Adam and P. Royer, *Gold Bull.*, 2007, 40, 240-244.
78. D. Stuart, A. Haes, C. Yonzon, E. Hicks and R. Van Duyne, *IEE Proc. Nanobiotechnol.*, 2005, 152, 13-32.

79. A. J. Haes, S. Zou, G. C. Schatz and R. P. Van Duyne, *J. Phys. Chem. B.*, 2004, 108, 6961-6968.
80. A. J. Haes, S. Zou, G. C. Schatz and R. P. Van Duyne, *J. Phys. Chem. B.*, 2004, 108, 109-116.
81. J. Kastner, B. Plank, D. Salaberger and J. Sekelja, Defect and Porosity Determination of Fibre Reinforced Polymers by X-ray Computed Tomography, 2010.
82. Y. Tamai, H. Tanaka and K. Nakanishi, *Macromolecules.*, 1995, 28, 2544-2554.
83. Y. Huang, P. Zhang, J. Fu, Y. Zhou, X. Huang and X. Tang, *J. Membr. Sci.*, 2009, 339, 85-92.
84. W. Caseri, *Macromol. Rapid Commun.*, 2000, 21, 705-722.
85. W. Caseri, *Chem. Eng. Commun.*, 2008, 196, 549-572.
86. A. Massaro, F. Spano, A. Lay-Ekuakille, P. Cazzato, R. Cingolani and A. Athanassiou, *IEEE Trans. Instrum. Meas.*, 2011, 1-9.
87. C. X. Liu and J. W. Choi, An embedded PDMS nanocomposite strain sensor toward biomedical applications, 2009.
88. H. Althues, J. Henle and S. Kaskel, *Chem. Soc. Rev.*, 2007, 36, 1454-1465.
89. S. Li, M. M. Lin, M. S. Toprak, D. K. Kim and M. Muhammed, *Nano Rev.*, 2010, 1, 1-19.
90. A. Massaro, F. Spano, R. Cingolani and A. Athanassiou, *IEEE Sens. J.*, 2011, 1780-1786.
91. B. Aswathy, G. Avadhani, I. Sumithra, S. Suji and G. Sony, *J. Mol. Liq.*, 2011, 165-169.
92. K. Wang, T. Huang, H. Liu, Y. Zhao and C. Sun, *Colloids Surf. A.*, 2008, 325, 21-25.
93. C. Vargas-Hernandez, M. Mariscal, R. Esparza and M. Yacaman, *Appl. Phys. Lett.*, 2010, 96, 213115-213115-213113.
94. Z. L. Jiang, Z. Feng and X. C. Shen, *Chinese Chem. Lett.*, 2001, 12, 551-554.
95. X. H. Liao, J. J. Zhu and H. Y. Chen, *Mater. Sci. Eng. B.*, 2001, 85, 85-89.
96. H. Yang, C. Huang, A. Tang, X. Zhang and W. Yang, *Mater. Res. Bull.*, 2005, 40, 1690-1695.
97. M. Tsuji, M. Hashimoto, Y. Nishizawa, M. Kubokawa and T. Tsuji, *Chem. Eur. J.*, 2005, 11, 440-452.
98. M. Sabet, M. Salavati-Niasari and F. Davar, *Micro Nano Lett.*, 2011, 6, 904-908.
99. M. Shen, Y. Du, N. Hua and P. Yang, *Powder Technol.*, 2006, 162, 64-72.
100. P. Tiemblo, E. Benito, N. García, A. Esteban-Cubillo, R. Pina-Zapardiel and C. Pecharromán, *RSC Adv.*, 2012, 2, 915-919.
101. H. Wang, Y. Wu, B. Lassiter, C. L. Nehl, J. H. Hafner, P. Nordlander and N. J. Halas, *Proc. Natl. Acad. Sci. U. S. A.*, 2006, 103, 10856-10860.
102. N. Nath and A. Chilkoti, *Anal. Chem.*, 2002, 74, 504-509.
103. N. Nath and A. Chilkoti, *Anal. Chem.*, 2004, 76, 5370-5378.
104. J. Ozhikandathil, S. Badilescu and M. Packirisamy, *IEEE Sens. J.*, 2012, 12, 2791-2798.
105. J. Ozhikandathil, S. Badilescu and M. Packirisamy, *J. Biomed. Opt.*, 2012, 17, 077001-077001-077001-077009.
106. A. Buonerba, C. Cuomo, S. Ortega Sánchez, P. Canton and A. Grassi, *Chem. Eur. J.*, 2012, 18, 709-715.
107. X. Li, L. Wang, Y. Fan, Q. Feng and F. Cui, *J. Nanomater.*, 2012, 2012, 19.

108. A. J. Demello, *Nature.*, 2006, 442, 394-402.
109. M. Long, M. A. Sprague, A. A. Grimes, B. D. Rich and M. Khine, *Appl. Phys. Lett.*, 2009, 94, 133501.
110. S. W. Lee, D. S. Kim, S. S. Lee and T. H. Kwon, *J. Micromech. Microeng.*, 2006, 16, 1067-1072.
111. H. Bockelmann, V. Heuveline and D. P. J. Barz, *Biomicrofluidics.*, 2012, 6, 024123.
112. M. Jain, A. Yeung and K. Nandakumar, *J. Microelectromech. S.*, 2009, 18, 376-384.
113. N. T. Nguyen and X. Huang, *Biomed. Microdevices.*, 2006, 8, 133-139.
114. N. T. Nguyen and Z. Wu, *J. Micromech. Microeng.*, 2005, 15, R1-R16.
115. C. C. Hong, J. W. Choi and C. H. Ahn, *Lab. Chip.*, 2004, 4, 109-113.
116. G. S. Jeong, S. Chung, C. B. Kim and S. H. Lee, *Analyst.*, 2010, 135, 460-473.
117. L. Zhang, H. Nakamura, C. G. Lee and H. Maeda, *RSC Adv.*, 2012, 2, 3708-3713.
118. W. Buchegger, A. Haller, S. van den Driesche, M. Kraft, B. Lendl and M. Vellekoop, *Biomicrofluidics.*, 2012, 6, 012803.
119. E. M. Chan, R. A. Mathies and A. P. Alivisatos, *Nano Lett.*, 2003, 3, 199-201.
120. H. Song and R. F. Ismagilov, *J. Am. Chem. Soc.*, 2003, 125, 14613-14619.
121. Y. Luo, F. Yu and R. N. Zare, *Lab. Chip.*, 2008, 8, 694-700.
122. J. Kim, J. W. Hong, D. P. Kim, J. H. Shin and I. Park, *Lab. Chip.*, 2012, 12, 2914-2921.
123. K. P. Nichols, J. R. Ferullo and A. J. Baeumner, *Lab. Chip.*, 2006, 6, 242-246.
124. R. T. Tsai and C. Y. Wu, *Biomicrofluidics.*, 2011, 5, 014103.
125. A. A. S. Bhagat, E. T. K. Peterson and I. Papautsky, *J. Micromech. Microeng.*, 2007, 17, 1017-1024.
126. J. M. Ottino and S. Wiggins, *Science.*, 2004, 305, 485-486.
127. S. H. Wong, P. Bryant, M. Ward and C. Wharton, *Sens. Actuators B Chem.*, 2003, 95, 414-424.
128. M. Xian Lin, K. A. Hyun, H. S. Moon, T. Seok Sim, J. G. Lee, J. Chan Park, S. Suk Lee and H. I. Jung, *Biosens. Bioelectron.*, 2012, <http://dx.doi.org/10.1016/j.bios.2012.1006.1016>.
129. T. W. Lim, Y. Son, Y. J. Jeong, D. Y. Yang, H. J. Kong, K. S. Lee and D. P. Kim, *Lab. Chip.*, 2010, 11, 100-103.
130. T. P. Forbes and J. Kralj, *Lab. Chip.*, 2012, 12, 2634-2637.
131. F. Schönfeld, V. Hessel and C. Hofmann, *Lab. Chip.*, 2004, 4, 65-69.
132. W. Buchegger, C. Wagner, P. Svasek, B. Lendl, M. Kraft and M. J. Vellekoop, *Sens. Actuators B Chem.*, 2011, 159, 336-341.
133. C. P. Jen, C. Y. Wu, Y. C. Lin and C. Y. Wu, *Lab. Chip.*, 2003, 3, 77-81.
134. K. Ren, W. Dai, J. Zhou, J. Su and H. Wu, *Proc. Natl. Acad. Sci. U. S. A.*, 2011, 108, 8162-8166.
135. I. H. Shames, *Mechanics of fluids*, McGraw-Hill, New York, 1962.
136. W. L. Barnes, A. Dereux and T. W. Ebbesen, *Nature.*, 2003, 424, 824-830.
137. X. Hoa, A. Kirk and M. Tabrizian, *Biosens. Bioelectron.*, 2009, 24, 3043-3048.
138. S. Badilescu and M. Packirisamy, *Polymers.*, 2012, 4, 1278-1310.

139. C. C. Lin, J. H. Wang, H. W. Wu and G. B. Lee, *J. Lab. Autom.*, 2010, 15, 253-274.
140. X. Cheng, G. Chen and W. R. Rodriguez, *Anal. Bioanal. Chem.*, 2009, 393, 487-501.
141. H. Ben-Yoav, P. H. Dykstra, W. E. Bentley and R. Ghodssi, *Biosens. Bioelectron.*, 2012, 38, 114-120.
142. T. Zhang, Y. He, J. Wei and L. Que, *Biosens. Bioelectron.*, 2012, 38, 382-388.
143. A. Abbas, M. J. Linman and Q. Cheng, *Biosens. Bioelectron.*, 2011, 26, 1815-1824.
144. W. T. Hsu, W. H. Hsieh, S. F. Cheng, C. P. Jen, C. C. Wu, C. Y. Lee, W. Y. Li, L. K. Chau, C. Y. Chiang and S. R. Lyu, *Anal. Chim. Acta.*, 2011, 75-82.
145. C. Huang, K. Bonroy, G. Reekmans, W. Laureyn, K. Verhaegen, I. De Vlaminck, L. Lagae and G. Borghs, *Biomed. Microdevices.*, 2009, 11, 893-901.
146. C. Huang, K. Bonroy, G. Reekman, K. Verstrecken, L. Lagae and G. Borghs, *Microelectron. Eng.*, 2009, 86, 2437-2441.
147. Y. T. Li, H. S. Liu, H. P. Lin and S. H. Chen, *Electrophoresis.*, 2005, 26, 4743-4750.
148. J. D. Qiu, L. Wang, R. P. Liang and J. W. Wang, *Electrophoresis.*, 2009, 30, 3472-3479.
149. A. J. Haes and R. P. Van Duyne, *J. Am. Chem. Soc.*, 2002, 124, 10596-10604.
150. Z. Geng, W. Liu, X. Wang and F. Yang, *Sens. Actuators A Phys.*, 2011, 169, 37-42.
151. F. Zhou, M. Lu, W. Wang, Z. P. Bian, J. R. Zhang and J. J. Zhu, *Clin. Chem.*, 2010, 56, 1701-1707.
152. D. Shalom, R. C. R. Wootton, R. F. Winkle, B. F. Cottam, R. Vilar, A. J. demello and C. P. Wilde, *Mater. Lett.*, 2007, 61, 1146-1150.
153. Y. Song, E. Doomes, J. Prindle, R. Tittsworth, J. Hormes, S. Challa and R. Kumar, *J. Phys. Chem. B.*, 2005, 109, 9330-9338.
154. S. Batabyal, S. Rakshit, S. Kar and S. K. Pal, *Rev. Sci. Instrum.*, 2012, 83, 43113.
155. H. Roder, K. Maki and H. Cheng, *Chem. Rev.*, 2006, 106, 1836-1861.
156. H. SadAbadi, M. Ghasemi and A. Ghaffari, *Biomed. Pap. Med. Fac. Univ. Palacky Olomouc Czech Repub.*, 2007, 151, 73-78.
157. W. H. Song, A. Hierlemann and J. Lichtenberg, Dead-end injection molding of polymeric microcantilever arrays, 2005.
158. J. Kim, J. Park, J. Lee, E. Yoon and S. Park, Biohybrid microsystems actuated by cardiomyocytes: microcantilever, microrobot, and micropump, 2008.
159. M. Liu, J. Sun, Y. Sun, C. Bock and Q. Chen, *J. Micromech. Microeng.*, 2009, 19, 035028.
160. N. B. Trung, H. Yoshikawa, E. Tamiya, P. H. Viet, Y. Takamura and T. Ashahi, *Jpn. J. Appl. Phys.*, 2012, 51, 037001.
161. J. E. Sader, *J. Appl. Phys.*, 2001, 89, 2911-2921.